

**SILICON NANOCRYSTALS EMBEDDED IN SiO₂
FOR
LIGHT EMITTING DIODE (LED)
APPLICATIONS**

**A THESIS SUBMITTED TO
THE GRADUATE SCHOOL OF NATURAL AND APPLIED SCIENCES
OF
MIDDLE EAST TECHNICAL UNIVERSITY**

BY

MUSTAFA KULAKÇI

**IN PARTIAL FULFILLMENT OF THE REQUIREMENTS
FOR
THE DEGREE OF MASTER OF SCIENCE
IN
PHYSICS**

AUGUST 2005

Approval of the Graduate School of Natural and Applied sciences

Prof. Dr. Canan Özgen
Director

I certify that this thesis satisfies all the requirements as a thesis for the degree of Master of Science.

Prof. Dr. Sinan Bilikmen
Head of Department

This is to certify that we have read this thesis and that in our opinion it is fully adequate, in scope and quality, as a thesis for the degree of Master of Science.

Prof. Dr. Raşit Turan
Supervisor

Examining Committee Members

Prof. Dr. Çiğdem Erçelebi	(METU,PHYS)	_____
Prof. Dr. Raşit Turan	(METU,PHYS)	_____
Prof. Dr. Bahtiyar Salamov	(GAZİ UNI,PHYS)	_____
Prof. Dr. Nizami Hasanlı	(METU,PHYS)	_____
Assoc. Prof. Dr. Enver Bulur	(METU,PHYS)	_____

I hereby declare that all information in this document has been obtained and presented in accordance with academic rules and ethical conduct. I also declare that, as required by these rules and conduct, I have fully cited and referenced all material and results that are not original to this work.

Name-surname: Mustafa Kulakçı

Signature :

ABSTRACT

SILICON NANOCRYSTALS EMBEDDED IN SiO₂ FOR LIGHT EMITTING DIODE (LED) APPLICATIONS

Kulakçı, Mustafa

M. Sc. Department of Physics

Supervisor: Prof. Dr. Raşit Turan

August 2005, 101 pages

In this study, silicon nanocrystals (NC) were synthesized in silicon dioxide matrix by ion implantation followed by high temperature annealing. Annealing temperature and duration were varied to study their effect on the nanocrystal formation and optical properties. Implantation of silicon ions was performed with different energy and dose depending on the oxide thickness on the silicon substrate. Before device fabrication, photoluminescence (PL) measurement was performed for each sample. From PL measurement it was observed that, PL emission depends on nanocrystal size determined by the parameters of implantation and annealing process. The peak position of PL emission was found to shift toward higher wavelength when the dose of implanted Si increased. Two PL emission bands were observed in most cases. PL emission around 800 nm originated from Si NC in oxide matrix. Other emissions can be attributed to the luminescent defects in oxide or oxide/NC interface.

In order to see electroluminescence properties Light Emitting Devices (LED) were fabricated by using metal oxide semiconductor structure, current-voltage (I-V) and electroluminescence (EL) measurements were conducted. I-V results revealed that,

current passing through device depends on both implanted Si dose and annealing parameters. Current increases with increasing dose as one might expect due to the increased amount of defects in the matrix. The current however decreases with increasing annealing temperature and duration, which imply that, NC in oxide behave like a well controlled trap level for charge transport. From EL measurements, few differences were observed between EL and PL results. These differences can be attributed to the different excitation and emission mechanisms in PL and EL process. Upon comparison, EL emission was found to be inefficient due to the asymmetric charge injection from substrate and top contact. Peak position of EL emission was blue shifted with respect to PL one, and approached towards PL peak position as applied voltage increased. From the results of the EL measurements, EL emission mechanisms was attributed to tunneling of electron hole pairs from top contact and substrate to NC via oxide barrier.

Keyword: Ion Implantation, Si Nanocrystal, LED, Photoluminescence (PL), Current-Voltage (I-V), Electroluminescence (EL).

ÖZ

SİLİKONDİOKSİT İÇİNE GÖMÜLMÜŞ SİLİKON NANOKRİSTALLERİN IŞIK YAYAN DİYOT (LED) UYGULAMALARI

Kulakçı, Mustafa

Yüksek Lisans, Fizik Bölümü

Tez Yöneticisi: Prof. Dr. Raşit Turan

Ağustos 2005, 101 sayfa

Bu çalışmada iyon ekme yöntemi kullanılarak SiO₂ matris içinde yüksek tavlama sıcaklığında silicon nanokristaller (NK) sentezlendi. Tavlama sıcaklığı, tavlama zamanı ve iyon ekme parametrelerinin nanokristal oluşumuna etkisi incelendi. Silicon iyonu ekimi, silicon taban üzerindeki oksit kalınlığına bağlı olarak farklı doz ve enerjide gerçekleştirildi. Örneklerden aygıt yapılmadan önce fotoluminesans (PL) ölçümleri alındı. PL ışımalarının, tavlama ve silicon iyonu ekim parametrelerine bağlı nanokristal büyüklüğü ve yoğunluğuyla değiştiği gözlemlendi. Birim hacme düşen ekilen Si atomu arttırıldığında, PL ışımalarının tepe pozisyonunun yüksek dalga boyuna doğru kaydığı gözlemlendi. PL ışımalarından 800 nm civarındaki NK'lerden kaynaklanırken, diğer ışımaların oksit matris içerisinde veya oksit/NK arayüzeyinde bulunan ışıyan kusurlardan kaynaklanabilmektedir.

Üretilen LED yapılarında akım-voltage (I-V) ve elektrolüminesans (EL) ölçümleri yapıldı. I-V sonuçları aygıttan geçen akımın hem ekilen Si iyonu dozuna ve hemde tavlama parametrelerine bağlı olduğunu açığa çıkardı. Artan dozla birlikte akımda artmaktadır. Ancak, artan tavlama sıcaklığı ve süresiyle aygıttan geçen akım azalmaktadır, bu durum oksit içindeki NK'lerin yük taşınımında iyi control edilebilen

tuzak seviyeleri gibi davrandığını göstermektedir. EL ölçümleri sonucunda, PL ve EL ışınmaları arasında bazı farklar gözlemlendi, bu durum uyarma ve ışınma mekanizmaları arasındaki farklılıklara atfedilebilir. PL ışınmasıyla karşılaştırıldığında, taban ve ön kontakten asimetrik yük enjeksiyonundan dolayı, EL ışınmasının verimliliği çok düşüktür. EL ışınımının tepe pozisyonu PL'inkine göre maviye kaymıştır ve aygıtta uygulanan voltaj arttırıldığında bu ışınma PL ışınmasına doğru kaymaktadır. EL ışınması sadece tabandan oksit matrise deşik sağlandığı durumda gözlemlenmiştir. Elde edilen ölçümler sonucundan EL ışınma mekanizmasının tepe kontağı ve Si tabandan NK'lere oksit bariyerinden elektron ve deşik çiftlerinin tünellemesi sonucu oluştuğu farzedilmiştir.

Anahtar Kelime: İyon Ekme, Si Nanokristal, LED, Fotolüminesans (PL), Akım-Voltage (I-V), Elektrolüminesans (EL).

ACKNOWLEDGMENTS

I would like to thank my supervisor Prof. Dr. Raşit Turan. He is a real guide throughout this study. Whenever I have a problem, he is always with me. I would also thank him for his friendship.

I would like to express my gratitude to Prof. Dr. Mehmet Parlak for having greatly benefited from his knowledge. Also thanks to Prof. Dr. Atilla Aydinli and group members about growth of ITO windows for our devices.

I intensely acknowledge my chief Ugur Serincan and Bülent Aslan to encourage continuing Ms degree, especially for their friendship and for helpful discussion.

My cousin Fazlı Çağrı Mermi is another important person whom I must thank very much about home mate, friendship, actually for everything during 3 years.

I wish to thank all colleges and friends from the lab. Thanks to Arif Sinan Alagöz, Ayşe Arat, Mustafa Arikan, Gülnur Aygün, Umut Bostancı, Arife Gencer, Eren Gülsen, Sema Memiş, Ayşe Seyhan, Selcuk Yerci and Yücel Eke for their invaluable support and a lot of good time spent together. Also thanks to my friends in the downstairs, Tahir Çolakoğlu, Mustafa Huş, Murat Kaleli, Hazbullah Karaağaç, Koray Yılmaz and Salur Kurucu for enjoyable time we spent together.

I would like to special thank my family for their encouragement and for long term financial support, without whose endless love, I could not carry on this study.

To all people who take care about me

TABLE OF CONTENTS

ABSTRACT.....	iv
ÖZ.....	vi
ACKNOWLEDGMENTS.....	viii
DEDICATION.....	ix
TABLE OF CONTENTS.....	x
LIST OF FIGURES.....	xii
LIST OF TABLES.....	xiii

CHAPTER

1 INTRODUCTION.....	1
2 QUANTUM DOTS.....	3
2.1 Wave Functions and Energy Levels.....	5
2.2 Density of States for Quantum Dots.....	10
2.3 Quantum Confinement Theory.....	13
2.3.1 Weak Confinement.....	14
2.3.2 Strong Confinement.....	17
3 SILICON NANOCRYSTALS IN SiO ₂	15
3.1 SiO ₂ and Properties.....	20
3.1.1 Oxygen Excess Centers.....	24
3.1.2 Oxygen Deficient Centers.....	24
3.2 Coarsening of Si Nanocrystals from Si Rich Oxide.....	26
3.2.1 Ostwald Ripening of Nanocrystals.....	26
3.2.2 Coarsening of Silicon Nanocrystals.....	29
3.3 Optical Properties of Silicon Nanocrystals.....	32
3.4 Exciton Migration and Electron-Hole Exchange Interaction.....	37

	3.4.1 Exciton Migration in Si Nanocrystal System.....	37
	3.4.2 Electron Hole Exchange Interactions.....	40
	3.5 Erbium (Er) Doped Si Nanocrystals.....	42
	3.6 Wavelength Engineering.....	45
	3.7 Electroluminescence and Current-Voltage Characteristics.....	46
	3.7.1 Direct Tunneling.....	48
	3.7.2 Fowler-Nordheim Tunneling.....	49
	3.8 Memory Effects.....	50
4	EXPERIMENTAL PROCEDURES.....	53
	4.1 Sample Preparation.....	53
	4.1.1 Ion Implantation.....	53
	4.1.2 Applications of Ion Implantation.....	55
	4.1.3 Implantation System.....	55
	4.1.4 Simulation of Ion Distribution for the Samples.....	57
	4.1.5 Annealing Procedure.....	59
	4.2 Cleaning Procedure.....	60
	4.3 Device Fabrication.....	60
	4.3.1 Design and Making of Copper Shadow Masks.....	61
	4.3.2 Device Schematic.....	62
	4.4 Device Characterization.....	63
5	RESULTS AND DISCUSSIONS.....	64
	5.1 Photoluminescence (PL) Results.....	64
	5.2 Current-Voltage (I-V) Results.....	72
	5.3 Electroluminescence (EL) Results.....	77
6	CONCLUSION.....	88
	REFERENCES.....	92
	ABBREVIATIONS AND ACRONYMS.....	101

LIST OF FIGURES

FIGURES

Figure 2.1 Representation of the density of states for different dimensional systems: (a) bulk (3D), (b) quantum well (2D), (c) quantum wire (1D), (d) quantum dot (0D) (corresponding to ideal cases).....	10
Figure 2.2 Absorption energy versus nanocrystal size calculated from effective mass approximation for Ge and Si.....	16
Figure 3.1 (a) SiO ₄ structural unit of most forms of SiO ₂ , showing the tetrahedral coordination. (b) Si ₂ O bonding configuration with Si–O–Si bond angle θ varying from 120° to 180° depending on the form of SiO ₂	22
Figure 3.2 Phase diagram of SiO ₂	25
Figure 3.3 Smoluchowski coalescence of islands on Ag. (I) island movement and collision (II) mass transferring and (III) relaxation from elongation to equilibrium shape.....	26
Figure 3.4 Illustration of nanocrystal formation sequence of Si in the SiO ₂ by ion implantation technique.....	30
Figure 3.5 Band structure of silicon, possible optical transitions and dispersion curve of phonon branches.....	32

Figure 3.6 Possible light emission mechanisms of Si nanocrystal SiO ₂ system (1) recombination of electron-hole pairs in the nanocrystal, (2) recombination through radiative centers at the nanocrystal/SiO ₂ interface and (3) radiative defect centers at the matrix.....	35
Figure 3.7 Exciton migration or energy transferring and exciton trapping in Si nanocrystals.....	38
Figure 3.8 Detailed scheme of the Si nanocrystal interacting levels with the main physical processes.....	43
Figure 3.9 Transport mechanism in MOS structure: (1) Fowler-Nordheim tunneling, (2) trapping at cluster and tunneling from cluster to another, (3) quasi free movement of electrons within the conduction band of SiO ₂ , (4) hopping conduction, (5) Poole-Frenkel tunneling.....	49
Figure 3.10 Simple schematic representation of; (a) conventional FG nonvolatile memory cell. (b) nanocrystal nonvolatile memory cell. ONO (oxide-nitride-oxide layer), poly is the polysilicon.....	51
Figure 3.11 (a) schematic cross section (b) band diagram during injection (c) storage (d) removal of an electron from a Si nanocrystal	52
Figure 4.1 Distribution of B in Si with varying implant energy.....	54
Figure 4.2 Basic schematic of ion implantation system from top view	56
Figure 4.3 Simulation result of the Si atoms for the sample series M4 having the oxide thickness of 40 nm, the simulation energy of 15 KeV was chosen. The	

peak concentration of implanted ions is at the depth of ~ 30 nm from the SiO ₂ surface	57
Figure 4.4 Simulation result for the sample M2 having the thickness of 100 nm. Si ions were implanted with the energy of 40 KeV and the peak position is at 72 nm from SiO ₂ surface.....	58
Figure 4.5 Copper shadow masks used in fabrication of the devices, larger dots for optic windows and smaller ones for top contacts.....	62
Figure 4.6 Cross section of the fabricated light emitting device structure. Back and top contacts are Au-Sb for n-type substrate, Al for p-type case.....	62
Figure 5.1 Room temperature PL results of the sample series M3 (n-type Si substrate with 100 nm thermal oxide) as a function of annealing temperature. Arrows on the spectrums indicate corresponding scale. Implanted Si dose is $5 \times 10^{16} \text{ cm}^{-2}$ with implant energy of 50 keV.....	65
Figure 5.2 Room temperature PL results of the sample series M2 as a function of annealing temperature and duration. Implantation energy is 40 keV, other parameters same with series M3	67
Figure 5.3 Room temperature PL observed from the series M1 (p-type Si substrate with 40 nm thermal oxide). Green spectrum from the sample annealed under vacuum, others are annealed under N ₂ atmosphere. Dose of implanted Si is $1 \times 10^{16} \text{ cm}^{-2}$ with implantation energy of 15 keV.....	70
Figure 5.4 Room temperature PL spectra from series M4. All parameters except dose are same. Implanted Si dose is $5 \times 10^{16} \text{ cm}^{-2}$, all other parameters are same as M1.....	71

Figure 5.5 Observed I-V results from Series M4 for different annealing time and duration. Samples substrate is p-type, oxide thickness is 40 nm, implant energy 15 keV and dose is $5 \times 10^{16} \text{ cm}^{-2}$ 73

Figure 5.6 Comparison of I-V results of series M1 and M4. (A) As implanted samples, (B) 2 hours annealed at 1050 °C (M1) and at 1100 °C (M4), (C) 4 hours annealed samples, (D) I-V results of series M1. Substrate, oxide thickness and implant energy are same for both series.....75

Figure 5.7 Observed I-V spectrum of series M1 at both forward and reverse bias range of 7 V. Substrate is n-type, oxide thickness 100 nm, implanted Si dose $5 \times 10^{16} \text{ cm}^{-2}$ with an implant energy of 40 keV.....76

Figure 5.8 EL spectrum of series M1 and oxide as a function of applied voltage under forward bias. PL spectrum given for comparison and EL spectrum of oxide is given as a reference.....78

Figure 5.9 Observed EL results with varying applied voltage under forward bias for the series M4. Corresponding PL spectrums are given for comparison for each sample. Arrows indicate corresponding intensity scale.....79

Figure 5.10 EL results taken from series M2 as a function of applied voltage under reverse bias. EL intensity increases with increase in applied voltage. For as implanted and and °C annealed samples EL and PL intensities are comparable. At higher temperature PL is much more intense than EL.....80

Figure 5.11 Change of peak position and intensity of EL emission for varying voltage for annealed samples of M4 and M2. Red curves represent the peak position belong to right side and black ones represent intensity belong the left side of the graphs.....86

LIST OF TABLES

Table 3.1 Compact polymorphic forms of SiO ₂	21
Table 4.1 Physical conditions of the prepared samples for the device fabrication.....	59

CHAPTER 1

INTRODUCTION

Invention of vacuum tubes at around 1904 could be accepted start point of today's information era. Big stimuli were given by the birth of transistor and laser in 1947 and 1960 respectively. Following these, developments in the field of fiber optic technologies and heterojunction low dimensional structures led to building of complex electronic, optoelectronic and optic systems.

Today many efforts are devoted to low dimensional systems and nanotechnology in almost all scientific and technical areas. Researches have focused on development of solid state devices based on low dimensional structures (quantum well, quantum wire and quantum dot (nanocrystal)), on molecular electronics that uses covalently bonded molecular structures in device configuration and integration of these structures in the same systems.

Low dimensional quantum heterostructure systems have been very attractive topic for 30 years in solid state physics for both theoretical and experimental studies. Using these structures lots of new and superior devices have been realized especially in the optoelectronic area. Nowadays zero dimensional systems known as quantum dots or nanocrystals have become much because physical properties of nanocrystalline material can be modified easily through playing with size of the quantum dot. Band gap energy of the quantum dot increases with respect to bulk value due to confinement of wave function of electrons in all direction. One of the main reasons of interest to quantum dots is to exploit their totally quantized energy levels and density of states and easily modified emission energy which offers very narrow emission and absorption spectrum. Therefore very reliable and temperature immune light emitting devices can be fabricated from these nanometer structures.

One of important outcomes of quantum confinement effect is realized in indirect gap materials. These materials known as very poor light emitter due requirement of phonons to conserve crystal momentum. However, in nanocrystalline structure of these materials momentum conservation phenomena is suppressed, as carriers confined in very small

dimensions in real space, their wave functions due to uncertainty principle extended in momentum space so in light emission and absorption becomes direct or quasi-direct transition as in the case of direct band gap materials. Therefore, opportunity of using indirect band gap materials becomes possible in light emitting devices.

Recent developments have shown that Si nanocrystals are most promising candidate to be the leading material in both microelectronics and optoelectronics. Electronic and photonic devices based on bulk Si crystal are facing important problems due to the increasing demands of today`s Si technology. In order to solve the problems of Si technology in future permanently, intensive researches have been conducted all over the world to shift the technology towards Si nanocrystal based micro photonics and microelectronic integrated systems. Although efficient PL emission has been obtained from Si nanocrystals, EL emission which is important technologically is still inefficient to use as electrically driven optical components.

Major motivation behind the work carried out in this thesis is to shed light on the physical mechanisms taking place in a nanocrystal based EL device. Topic studied in this work is widely studied and discussed issue in the scientific community dealing with this field. The theoretical and experimental aspects of nanocrystals formation and their utilization in the light emitting devices have been reviewed and summarized in this work: Chapter 2 is devoted to general description of quantum dots and summary of quantum dot theory. In Chapter 3, Si nanocrystal in oxide matrix presented with general perspective; oxide matrix defects, nanocrystal formation kinetics, optical and electrical properties Si nanocrystal and few example of device structures based on Si nanocrystals are described shortly. Chapter 4 is devoted experimental procedures from sample preparation to LED fabrication. In Chapter 5, optical and electrical measurements are given and discussed qualitatively. In Chapter 6, main conclusions drawn in this thesis are summarized.

CHAPTER 2

QUANTUM DOTS

The advances in semiconductor technology allow one to fabricate heterostructures in which all existing degrees of freedom of electron propagation are quantized. These structures are called quantum-dot, quantum-box, nanocrystals, quantum crystallites, quasi-zero-dimensional structures, artificial atoms, or super atoms [1-3].

Complete quantization of electron's free motion is done by trapping it in a quasi-zero-dimensional quantum dot. Because of this, they exhibit quantum confinement effects. This was first achieved by scientist from Texas Instruments Incorporated with the creation of a square quantum dot having a side length of 250 nm, etched by means of lithography [4]. As a result of the strong confinement imposed in all three spatial dimensions, quantum dots resembles to the atoms in the way of totally discrete energy spectrum. Therefore, it is clear why they are called as macro or super atoms.

What makes the quantum dots such unusual structure is, first of all, the possibility of controlling their shapes, their dimensions, the structure of the energy levels, and the number of confined electrons. The most striking of these effects is the quantum dot size dependence of absorbed or emitted the light wavelength. This has done with how much place the electrons have to move. As in atoms and molecules, the electrons in quantum dot exist only in certain energy levels. The light absorbed when an electron in an energy level is excited to a higher energy level in the form of photon with energy equal to the difference in energy between the two levels. If the spacing between the energy levels is large, the quantum dot will absorb shorter wavelength photons. If the spacing between energy levels is small, the quantum dot will absorb or emit longer wavelength photons. It turns out that the smaller the quantum dot, the more energetic the electrons and this translates into larger energy spacing. Therefore, small quantum dots absorb short wavelength light, whereas large quantum dots absorb long wavelength light. Being able to control the optical properties of the quantum dot by changing its size is important in developing applications from these nanostructures.

Quantum confinement effects describe the modification of material properties of quantum dots (nanocrystals) or clusters depending on their size and brings about some new physical properties different from their bulk (three dimensional) structures. As a result of the confinement in all directions there is a change in the wave function describing the behavior of electrons, holes, hydrogen like bound state of electrons and holes known as excitons and consequently the number of state per unit energy, i.e. the density of state (DOS), changes as a function of energy E of the particles. In the case of bulk material, the density of states increases with energy of the particle following the parabolic law, being the DOS proportional to $E^{1/2}$. However, in the case of a 0-D structure, spatial confinement shifts both absorbing and luminescing states to higher energies and affect the density of electronic states due to rising of minimum kinetic energy and in the ideal case; the DOS of quantum dot is illustrated as delta function dependence of energy. It is generally known that the band-gap energy and the exciton binding energies increase with decreasing cluster size, and thereby the splitting energy, Δ , between singlet and triplet states can reach some tens of meV due to better overlap of electron and hole envelope wave functions from the strong confinement in the nanocrystals. This change is large at visible spectral region and so small changes in nanocrystal size cause large shifts in energy of the emitted photons. If the emission from the nanocrystal comes from band to band recombination of excitons in it, the band-gap energy determines directly the energy the energy of the emitted photon. The local concentration of e-h pairs in nanocrystal as the outcome of the geometric confinement is very high and this can lead to a variety of nonlinear optical phenomena.

In addition to all properties mentioned above, there is a big impact of the quantum size effect especially on the optical properties of the indirect-gap materials. In indirect band-gap semiconductors, the optical transitions are allowed only if phonons are absorbed or emitted to conserve the crystal momentum and cause these materials to be inefficient for photon emission devices. The spatial confinement by the finite size spread the electron and hole wave functions in the k (momentum) space inside the quantum dot and increases the uncertainty of their crystal momentum, thus allowing optical transitions in which phonons are not involved and significantly enhancing the oscillator strength of the zero phonon transitions. One of the general predictions from the theory is

that in small nanocrystals the probability of no-phonon (NP) transitions should increase with respect to phonon-assisted (PA) process. Therefore, optical properties of nanocrystals of indirect-gap materials have to be considered on the basis of a competition between indirect and quasidirect recombination channels. So, one can expect that the radiative recombination rate of excitons will be enhanced with decreasing quantum dot size.

The luminescence dynamics of optical centers in nanocrystals depends strongly on the phonon density of states (PDOS), which are quite distinct from of bulk materials. The PDOS in a QD becomes discrete and the low frequency phonon modes are cut off. Therefore all phonon assisted energy transfer processes, in which the energy mismatch between donor and acceptor is made up by lattice phonons, are affected because of the alteration of PDOS in nanocrystal, i.e. energy transfer efficiency based on hopping length between different states and the probability of finding the acceptor states or another nanocrystal as the energy matching acceptor in the neighborhood of a donor nanocrystal or in itself are highly restricted.

Although all mentioned outcome of the quantum confinement effects above, there are lots of important points in these system have not solved yet in both experimental and theory sides: for example formation process of quantum dots and the full development of the analysis about their band structures, etc.

2. 1. Wave Functions and Energy Levels

An electron in a semiconductor is characterized by the effective mass m^* generally smaller than the free electron mass m_0 . Then, the de Broglie wavelength of an electron in a semiconductor λ is greater than that of a free electron λ_0 :

$$\lambda = \frac{h}{p} = \frac{h}{\sqrt{2m^*E}} = \lambda_0 \sqrt{\frac{m_0}{m^*}} \quad (2.1)$$

Where h is Planck constant and p is electron momentum. If geometrical size of semiconductor sample with dimensions X, Y, and Z introduced: Since only an integer number of half-waves of the electron or hole can be put in any finite size system, instead

of continuous energy spectrum and a continuous number of the electron states, a set of discrete electron states and energy levels are obtained, which are characterized by the corresponding number of half wavelength. And this phenomenon generally referred as quantization of electron motion. One can distinguish four different cases, depending on the system dimensions:

- Three dimensional or bulk situation, in which quantization of electron is not significant at all, and an electron behaves like free particle in the crystal and characterized with the effective mass m^* :

$$\lambda \ll X, Y, Z,$$

- In quantum well or two-dimensional system, the quantization of electron occurs in one dimension in the growth direction while in the other two directions electron motion is free:

$$\lambda \sim X \ll Y, Z$$

- In quantum wire or one dimensional system case, quantization occurs in two dimensions and electron moves freely along the wire:

$$\lambda \sim X \sim Y \ll Z$$

- In zero dimensional or nanocrystal (quantum dot) case, the quantization occurs in all directions and the electron cannot move freely in any directions:

$$\lambda \sim X \sim Y \sim Z$$

Nanostructures are quantum mechanical systems inasmuch as their sizes are comparable with the typical de Broglie wavelength of electrons in solids, so that a quantum mechanical treatment of the problem is strictly needed to determining the wave function of a single electron or of the whole system. The wave function Ψ of an electron or electron system satisfies the principal equation of quantum mechanics, the Schrödinger equation,

$$i\hbar \frac{\partial \Psi}{\partial t} - H\Psi = 0 \tag{2.2}$$

Where H is the Hamiltonian of the system,

$$H = -\frac{\hbar^2 \nabla^2}{2m} + V(\vec{r}) \quad (2.3)$$

$V(\vec{r})$ is the potential energy and the first term is the kinetic energy operator. If $V(\vec{r})$ is assumed to time independent, Ψ can be separated to its time and spatial coordinates:

$$\Psi(\vec{r}, t) = e^{-\frac{iEt}{\hbar}} \Psi(\vec{r}) \quad (2.4)$$

Substituting this in to the Eq. (1.2) we get the time independent Schrödinger equation:

$$\left[-\frac{\hbar^2 \nabla^2}{2m} + V(\vec{r}) \right] \Psi(\vec{r}) = E \Psi(\vec{r}) \quad (2.5)$$

The major aim of solving this stationary Schrödinger equation in quantum dot system is related with electron (hole) bound states in dot. In this case, one can get discrete energies of bound state, can calculate relaxation of excited states due to the interactions with free electrons, phonons, and defects, and lastly results of interaction with electromagnetic field.

To solve the equation above two important simplifications can be imposed; isotropic effective mass m^* i.e. independent of both position and the energy of the electron and the other is idealized step like potential profile, which can be analyzed easily. The simplest potential $V(x, y, z)$ of this type is

$$V(x, y, z) = \begin{cases} 0 & \text{inside the dot (box)} \\ +\infty & \text{outside the dot (box)} \end{cases} \quad (2.6)$$

For this potential profile the solution of Eq. (1.5) can be written down as

$$\Psi_{n_1, n_2, n_3}(x, y, z) = \sqrt{\frac{8}{XYZ}} \sin\left(\frac{\pi x n_1}{X}\right) \sin\left(\frac{\pi y n_2}{Y}\right) \sin\left(\frac{\pi z n_3}{Z}\right) \quad (2.7)$$

$$E_{n_1, n_2, n_3} = \frac{\hbar^2 \pi^2}{2m^*} \left(\frac{n_1^2}{X^2} + \frac{n_2^2}{Y^2} + \frac{n_3^2}{Z^2} \right) \quad (2.8)$$

Where $n_1, n_2, n_3 = 1, 2, 3, \dots$, E_{n_1, n_2, n_3} is the total electron energy spectrum for the bound states in the quantum dot associated with the confinement. Existence of three direction of quantization cause to the presence of three discrete numbers directly, then threefold discrete energy levels and wave function localization in all dimension of the dot (box) can be obtained. Generally, all energies are different, that is not degenerated,

but if two or all dimensions are equal or the dimensions ratios are integers, some levels will coincide with different quantum numbers and this coincidence results in degeneracy. This discrete spectrum in quantum dot and the lack of free electron propagation are the main distinguishing features of quantum dots or boxes from other systems (3D, 2D or 1D). As it is well known, these features are typical for atomic systems.

Due to the similarity with atoms, QD generally studied with the shape of spherical dots. In this case, the potential is

$$V(r) = \begin{cases} 0 & \text{for } r \leq R \\ V_b & \text{for } r \geq R \end{cases} \quad (2.9)$$

Where R is the radius of the dot and r is magnitude of radius vector. It is known from quantum mechanics that for this situation the solution of Schrödinger equation can be expressed by separating it into its angular and radial parts.

$$\Psi(r, \theta, \phi) = R(r)Y_{l,m}(\theta, \phi) \quad (2.10)$$

$Y_{l,m}(\theta, \phi)$ is spherical function, r , θ , ϕ are spherical coordinates, and l and m are quantum numbers representing angular momentum and its projection along the z axis. Writing the Schrödinger equation for the radial function $R(r)$

$$\left[-\frac{\hbar^2}{2m^*} \frac{\partial^2 \chi(r)}{\partial r^2} + V_{\text{eff}}(r) \right] \chi(r) = E\chi(r), \quad R(r) = \frac{\chi(r)}{r} \quad (2.11)$$

and

$$V_{\text{eff}}(r) = V(r) + \frac{\hbar^2 l(l-1)}{r^2} \quad (2.12)$$

Therefore, we can easily observe that working on spherical coordinates reduces the equation into one-dimensional coordinate due to the spherical symmetry. It is clear from Eq. (2.11) that, the effective potential $V_{\text{eff}}(r)$ depends on quantum number l , but does not depend on m and the energy is function of principal quantum number n from and the angular momentum l .

In the simple cases for $l=0$ the solution of Eq. (2.11) can be easily obtained with the potential $V(r)$ as;

$$\Psi(r) = \begin{cases} A \sin \frac{k_w r}{r}, & k_w = \sqrt{2m^* E} & \text{if } r < R \\ B e^{-\frac{k_b r}{r}}, & k_b = \sqrt{\frac{2m^*(V_b - E)}{\hbar}} & \text{if } r > R \end{cases} \quad (2.13)$$

Using the boundary conditions the equation for the energy;

$$\text{Sink}_w R = \pm \sqrt{\frac{\hbar^2}{2m^* V_b}} k_w \quad (2.14)$$

Being the potential well deep enough, the solution to Eq. (2.14) is;

$$k_w = \pi n; \quad E_{n,l=0} = -V_b + \frac{\hbar^2 \pi^2 n^2}{2m^* R^2} \quad (2.15)$$

With the analysis of this last equation the condition on the existence of the level inside the spherical well is

$$V_b \geq \frac{\pi^2 \hbar^2}{8m^* R^2} \quad (2.16)$$

Therefore taking into account the dot radius, potential well must be large enough to confine the electron. That is the behavior of energies in confined system is expected as a function of the spatial dimension, namely the confinement energy decreases as the size of the system (nanocrystal size) increases.

In the practical application the confinement potential can be supplied by growing the nanocrystal in a higher band gap matrix than the dot material. The discontinuities at the conduction band and the valance band allow the confinement of electrons and holes. In the case of type-I heterostructures both electrons and holes are confined within the nanocrystal itself, for type-II heterostructures electrons and holes confined in either nanocrystal or matrix separately. This situation can be very useful for development of quantum dot solar cell and would increase the responsivity of the QDIP (quantum dot infrared photo detector) as a result of the different transport media for the excited carriers in the devices; the unwanted recombination of electrons and holes can be minimized. There is a terminology, scarcely mentioned, known as antidot structure which is the situation that the nanocrystal rejects the created carrier pairs in itself or near its surface. Now the band gap of confining matrix potential is lower in the potential value than the nanocrystal; therefore carriers tend to settle in the matrix material and rejected by higher band gap nanocrystal.

Actually, the mentioned theory above cannot exhibit full structure of real nanocrystals in practice but only gives some hints to the real case; in reality the confining potential can not be infinite. There are a lot of parameters affect energy band structure of nanocrystal that have to be accounted: strain in the bonds due to lattice mismatch, polarization effect due to differences in dielectric constants, surface states between the core and matrix and variations in the shapes, etc.

2.2. Density of States for Quantum Dot

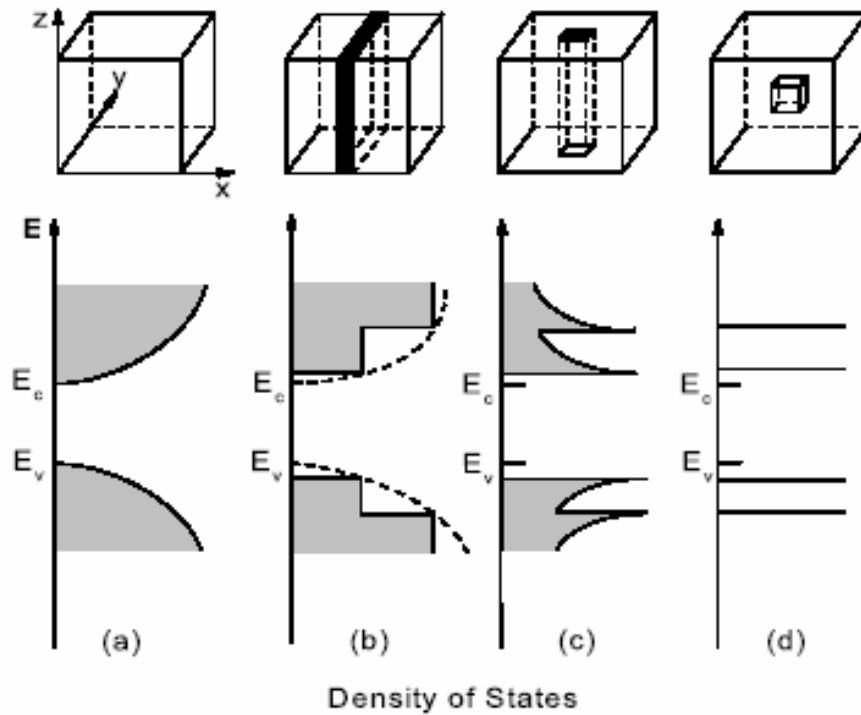


Figure 2.1. Representation of the density of states for different dimensional systems: (a) bulk (3D), (b) quantum well (2D), (c) quantum wire (1D), (d) quantum dot (0D) [6] (corresponding to ideal cases).

Many of the differences between the optical and electronic behaviors of the bulk and low dimensional semiconductors come from the difference in their density of states as a

result of the quantum confinement. Figure 1.1 illustrates the expected density of states for different systems varied with dimensionality. The density of state is defined as the number of states per energy per unit volume of real space i.e. how many electrons can exist within a range of energies [5]:

$$\rho(E) = \frac{dN}{dE} = \frac{dN}{dk} \frac{dk}{dE} \quad (2.17)$$

Starting from the Bloch theorem periodicity condition, with the unit cell side of L ,

$$k_{x,y,z} = \frac{2\pi}{L} n_{x,y,z} \quad (2.18)$$

n_x, n_y, n_z are integers, the volume of k -space occupied by single state defined by these integers is $(\frac{2\pi}{L})^3$. In k -space the total amount of N is given as, the total amount of volume of the sphere with radius k , divided by volume occupied by one state and by the volume of real space;

$$N_{3D} = 2 \frac{4\pi k^3}{3} \frac{1}{(2\pi/L)^3} \frac{1}{L^3} \quad (2.19)$$

using the parabolic dispersion relation between E and k from effective mass theory,

$$\frac{dk}{dE} = \left(\frac{2m^*}{\hbar^2}\right)^{\frac{1}{2}} E^{-\frac{1}{2}} \quad (2.20)$$

from Eq. (2.19) $\frac{dN}{dk} = 2 \frac{4\pi k^2}{(2\pi)^3}$, putting in to the Eq.(2.17) the density of state in bulk

case;

$$\rho_{3D}(E) = \frac{1}{2\pi^2} \left(\frac{2m^*}{\hbar^2}\right)^{\frac{3}{2}} E^{\frac{1}{2}} \quad (2.21)$$

The (DOS) in two dimensional systems follows analogously; but as there are only two degrees of freedom, successive states represented by integers values of n_x and n_y fill circle in k space. Therefore the total number of states per unit cross sectional area is given by the area of the circle of radius of k , divided by the area of occupation of each

state, multiplied by the spin factor 2. Following the same steps as in 3D case one can get the DOS for the 2D systems;

$$\rho_{2D}(E) = \frac{k}{\pi} \left(\frac{2m^*}{\hbar^2} \right)^{\frac{1}{2}} \frac{E^{-\frac{1}{2}}}{2} \quad (2.22)$$

by substituting k in terms of E from dispersion relation and if there are n confined states in the quantum well, then the density of states at any particular energy is sum over all bands below that point;

$$\rho_{2D}(E) = \sum_{i=1}^n \frac{m^*}{\pi \hbar^2} \Theta(E - E_i) \quad (2.23)$$

where Θ is unit step function. For the quantum wire with just one degree of freedom, the electron fills the state along a line. The total number of states is length of the line in k -space ($2k$), divided by the length occupied by one state ($\frac{2\pi}{L}$) and divided by the length in real space; following the same procedure as for the 3D and 2D cases, one can get DOS for one confined state:

$$\rho_{1D}(E) = \left(\frac{2m^*}{\hbar^2} \right)^{\frac{1}{2}} \frac{1}{\pi E^{\frac{1}{2}}} \quad (2.24)$$

where the E is measured from a subband minimum. If there are many (n) confined states within the quantum wire with subband minima E_i , then the DOS at any particular energy is sum over all the subbands below that energy:

$$\rho_{1D}(E) = \sum_{i=1}^n \left(\frac{2m^*}{\hbar^2} \right)^{\frac{1}{2}} \frac{1}{\pi(E - E_i)^{\frac{1}{2}}} \Theta(E - E_i) \quad (2.25)$$

It can be easily seen that, from 3D to the 1D there is a reduction in the functional form of $\rho(E)$ by a factor of $E^{\frac{1}{2}}$. DOS in three dimensions is continuous through the parabolic dispersion relation; on the other hand in quantum well it is a step function that closes to the DOS of 3D systems at high energy levels, and in the one dimensional DOS, $\rho(E)$ diverges at the bottom of each subband and then decreases as the kinetic energy increases.

The situation for 0D (quantum dot) is quite different from other dimensional systems. As the nanocrystal confined from all directions, then there are no dispersion curves; therefore the DOS for 0D is just dependent upon the number of confined levels inside the dot. For one single isolated dot, there would be just two states from spin degeneracy at the energy of each confined level, and the plot of the density of states as a function of energy Fig. 2.1. , would be a series of δ shaped peaks.

$$\rho_{0D}(E) = \sum_{E_i} \delta(E - E_i) \quad (2.26)$$

where E_i are discrete energy levels of the quantum dot and δ is the Dirac function. For an idealized system, the peaks are very narrow and infinitely large. In fact, interactions between carriers and impurities (any kind of defects in and outside the dot, and also natural broadening due to the uncertainty rule) as well as collisions with phonons bring about a broadening of discrete levels and, as a result, the peaks for physically realizable systems have finite amplitudes and widths. The δ -function dependence of the DOS is very important in the applications to the light emitting systems due to the very narrow emission spectra compared to the other high level systems.

2.3. Quantum Confinement Theory

There are some theoretical approaches to modeling the electronic, optic, and other physical properties of nanocrystals. Most of these approaches are difficult and required lots of parameters to describe the system, so it is tedious especially for experimentalist to check their results with theory easily. However, A. L. Efros and Al. L. Efros [2] proposed a simple quantum confinement theory and it improved by Brus, Lippens and Lannoo [8]. This theory based on the effective mass approximation (EMA) that relates the radius of nanocrystals R with their energy states in terms of bulk energy gap, kinetic energy and coulomb interaction energy . They take the nanocrystal as having perfect surface spherical dot confined by infinite potentials and with the EMA consideration, in which electrons and holes are assumed to placed at the edge of conduction and valence bands where the bands are follow parabolic dispersion relation and the both electron-

hole effective masses can be treated as isotropic. Depending on the dot size, there are two main case of quantum confinement regime; weak and strong confinement regions.

2.3.1. Weak Confinement

Excitons can be illustrated as single uncharged particle with mass $M=m_e^*+m_h^*$ with having translational center of mass motion and the energy dispersion relation can be written as:

$$E_n(K) = E_g - \frac{R_y}{n^2} + \frac{\hbar^2 K^2}{2M} ; \quad R_y = \frac{e^2}{2\epsilon a_B} = \epsilon \frac{m_0}{\mu} \times 0.53 \text{ \AA} \quad (2.27)$$

where K is wave vector for exciton and R_y is the exciton Rydberg energy, a_B is exciton Bohr radius ($a_B=a_e+a_h$, a_e and a_h are corresponding electron and hole Bohr radius) and μ is the reduced mass of electron hole pair bound system and written as $\frac{1}{\mu} = \frac{1}{m_e^*} + \frac{1}{m_h^*}$.

Therefore it can be understood from Eq. (2.27) that, the energy levels of exciton in the form of hydrogenlike energy level set. In the case of the creation of excitons by photon absorption the third term in the equation can be neglected.

Weak confinement regime refers to situation in which the dot radius R small but few times larger than that of exciton Bohr radius, a_B , of related material ($R>a_B$, so $R>a_e$ and $R > a_h$). In this case the quantization of exciton center of mass motion would occur and the dominant part of the energy comes from the coulomb interaction between electron and hole. Replacing the kinetic energy term in the Eq. (2.27) with the result obtained from the particle in a spherical dot. The quantized energy of the exciton can be expressed as:

$$E_{nlm} = E_g - \frac{R_y}{n^2} + \frac{\hbar^2 \chi_{ml}^2}{2MR^2} \quad (2.28)$$

where χ_{ml} are the roots of Bessel function. Therefore exciton in the nanocrystal can be described by quantum number n for the internal exciton states due to the Coulomb interaction and by two additional m, l describing the states due to the external confining potential barrier. For the ground state the energy of the exciton is given as;

$$E_{nml} = E_g - R_y + \frac{\pi^2 \hbar^2}{2MR^2} \quad (2.29)$$

so the first lying state energy is shifted up by the value of; $\Delta E = \frac{\mu}{M} (\pi a_B / R)^2 R_y$. Hence the increase in the exciton lowest energy is less than the Rydberg energy in the weak confinement regime.

2. 3.2. Strong Confinement

In the strong confinement regime the size of the nanocrystal (QD) much smaller than the exciton Bohr radius, so electron-hole Bohr radius. Therefore the Coulomb term become so small and it can be totally ignored or treated as perturbation and almost all energy up shift comes from the zero point kinetic energy of electron and hole as a result of considerable quantum confinement. At this situation, there is no correlated motion between electrons and holes, which means that formation of excitons most probably blocked and separate quantization of individual electrons and holes contribute the energy independently. At this point the conservation of momentum law changes to selection rule as in the atom or molecule and the optical transitions are allowed in the coupling of the electrons-holes having the same principal and orbital quantum numbers. The optical spectra in this regime can be considered as the series of discrete bands peaking through transition between subbands;

$$E_{nl} = E_g + \frac{\hbar^2}{2\mu R^2} \chi_{nl}^2 \quad \text{or approximately} \quad \Delta E \approx \frac{\hbar^2 \pi^2}{2\mu R^2} \quad (2.30)$$

It is important in here that, the Coulomb contribution to the lowest state is greater with comparing bulk, QW and quantum wire for which Coulomb energy of free pairs is assumed to be zero.

Actually there is a third confinement regime can be accounted, where the radius of crystallites much smaller than electron Bohr radius but larger than holes one, due to the large effective mass difference between the electron and the heavier hole. Now, the reduced mass μ in the above equation could be replaced by the effective mass of the electron, and the electron motion quantized, that the hole interacts with electron through

Coulomb attraction. However, as a result of Coulomb interaction, electron energy levels split in to several sublevels. Figure 2.2. gives the calculated exciton energy as a function of nanocrystal radius for Ge and Si.

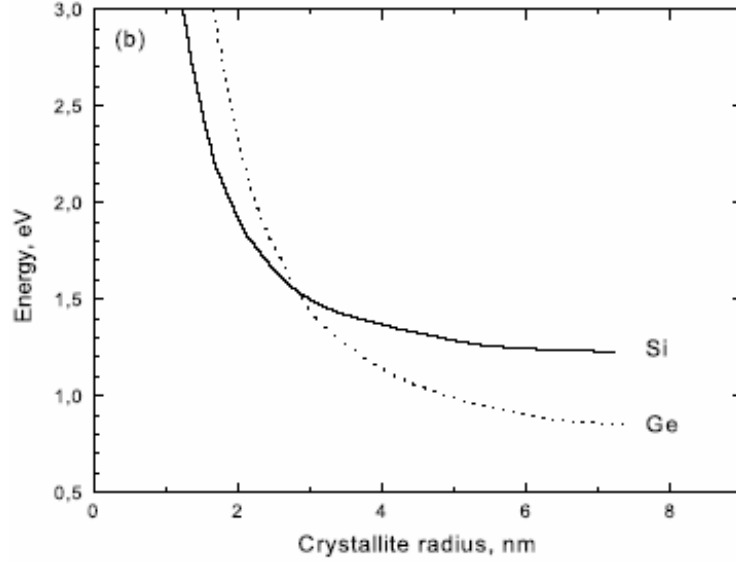


Figure 2.2. Absorption energy versus nanocrystal size calculated from effective mass approximation for Ge and Si [6].

Generally the dielectric constant of the confining matrix is less than the nanocrystal dielectric constant. The difference in dielectric constants, cause to surface polarization effects arising from an interaction of electron and hole inside a nanocrystal with induced image charges outside. The potential energy V^i for the interaction between the charge e with the polarization field that it induces known from the basic electromagnetic problems as dielectric sphere in different media:

$$V^i = \frac{e^2}{2\epsilon_N R} \left(\frac{R^2}{R^2 - r^2} + \frac{\epsilon_M}{\epsilon_N} \right) \quad (1.30)$$

where ϵ_N is the dielectric constant of nanocrystal, ϵ_M is the dielectric constant of surrounding matrix and R is the radius of nanocrystal. Therefore finite barrier height, polarization effects, the coulomb correlation between the electron and the hole and local field effects should be considered in the analyzing of the quantum confinement theory.

CHAPTER 3

SILICON NANOCRYSTALS IN SILICON DIOXIDE

(Pearls in the Oxide)

Due to having some unique properties, silicon is the dominant material of the today's electronic industry. Its band gap is very suitable for room temperature operation, abundant in nature (second after oxygen), very suitable for mass production with high purity and high crystal quality in the form of big wafers and the most important one is, its very stable and good quality oxide that allows the processing flexibility for device fabrication and very large scale integration. Demanding of speed and complex functionality in information area has already brought the chips very complex structures in both design and production. To overcome the speed problem up to now, the basic tool has been the reduction of the transistors size and increase of the number of component in the chip (the number of transistor on single chip exceeds hundred millions already). However, the standard silicon chip technology is getting close to its limits; one of the obstacles of the nowadays system is density of the transistor on the chip itself, as going to more cells per unit area the latch-up problem will emerge. In order to solve the latch-up effect, there are intensive researches to move the technology to SIMOX (separation by implantation of oxide) based system or fabricate the chips on sapphire substrate. The other, actually big problem is the signal carrier metallic line, as the dimension of the component decrease and the component density increase, same way the cross-section of metallic line reduced and its length will be increased per unit area (tens of Km per chip). This situation results in very big capacitive-resistive delay, information latency, overheating effect and the cross-talking between signal lines. The isolation lines only eliminate the cross-talking problem and the other problems require more appealing solutions. At this point, the potential is replacement of electrical lines with optical interconnects that promise high speed and information capacity. Signal transport by optic line and processing is actually mature technology, but it is pinned at the level of inter-chip data transfer. The main problem is that, most of the photonic devices are made

from direct band-gap material; it is too much difficult and expensive to integrate with existing silicon technology as intra chip transmission.

Although Si is the leading material of microelectronics, it is used in few photon absorbing devices and in the read-out circuitry of optoelectronic systems. Being indirect gap material, the absorption and emission of light is requires at least one phonon in bulk silicon that makes it inefficient emitter with very low internal quantum efficiency. Competitive non-radiative recombination rates are much higher than radiative ones and most of the excited pairs recombine nonradiatively. So, to make light emitting and high-speed telecommunication devices, more complex semiconductors, such as GaAs, InP, GaN, ZnSe and etc. are used. These materials are good at emitting light but are more expensive and hard to engineer compared with silicon.

In 1990, Canham achieved the efficient luminescence from porous silicon [9] and this study attracted many scientist interests towards the silicon nanocrystals. However from the application point of view, porous silicon consists of a network of nanocrystallites i.e. nanocrystals are not isolated from each other and it is a very complex system that depends on a variety of its fabrication and storage conditions. Because porous silicon suffer from poor stability due to the fragile hydrogen surface passivation, where oxidation of nanostructures easily takes place even at room temperature and it is not suitable for existing technology and mass production. To overcome these drawbacks of porous silicon, people have been searching of new techniques and approximation to produce efficient structures containing luminescent silicon nanocrystals [10- 12].

The most important approach is formation of nanocrystal inside the silicon dioxide (SiO_2), that have the superior properties compared with porous silicon in the side of mechanical strength and good passivation of grown structures to the both ambient conditions and non-radiative escape of excited carrier in the dots. Additionally, SiO_2 allows the fabrication of desired advanced devices in both electronic and optoelectronic area and gives someone tool of playing with the property of nanostructures by just changing the grown parameters easily. Today in SiO_2 matrix nanocrystalline structures of many materials can be grown: Si, Ge, SiGe, SiC, some metals and some other kinds of compound semiconductor such as CdS and CdSe. From these materials Si nanocrystals are mostly studied structures due to the good interface conditions with

SiO₂. Silicon nanocrystals are produced from the super saturated SiO₂ with Si atoms, introduced either by ion implantation or during the growth of the oxide such as by sputtering, chemical vapor deposition (CVD) or electron beam deposition of SiO_x film [13-17]. Among these techniques ion implantation is most appealing with contemporary silicon technology, but it can not allow building super lattice structures of Si nanocrystals sandwiched between SiO₂ layers.

With the quantum confinement effect nanocrystalline Si shows amazing behaviors that bulk silicon couldn't have. The most striking one is the efficient tunable luminescence from nanocrystalline Si due to the suppression of momentum conservation in the absorption and emission of the light. Becoming an efficient emitter Si has opened the door of all Si based micro photonics that is going to solve the all problem of current technology mentioned above. The tunability of emitted light color would give the engineering of efficient full color microdisplays and other light emitting devices. Er doped silicon nanocrystal devices are big candidate in the field of fiber optic technology as both signal source and electrically pumped light amplifier. The achievement of optical gain in Si dots [18, 19] gives the opportunity of the silicon lasers with varied wavelength. Although efficient light emission from nanocrystalline Si structures were realized, there is a big dilemma of the origin of the light whether it comes from the excited exciton inside the dot or from defect related centers at Si dot/ SiO₂ interface. And also, the problem of speed of the silicon nanocrystal based optic devices will emerge at soon because the original material itself has indirect band gap; the nanocrystalline silicon also assumed to preserve the band structure of its bulk at some level with slow radiative transitions despite the increased oscillator strength and it stays very slow compared to direct band gap semiconductors and their nanostructures as well.

In addition to the luminescence properties, Si nanocrystals show coulomb blockade and good charge trapping effect in its MOS structures. In the microelectronic area these properties allow very dense, fast and reliable single electron transistor (SET) and memory devices with low power consumption. As the device dimensions shrink, the problem of leaking of the charge carriers emerge laterally between devices or as the dielectric current of gate oxide that degrade the device performance and brings difficulty to the design of very dense microchips. On the other hand, nanocrystals in the gate oxide

of the MOSFETs can retain the charges in itself pumped from the substrate successfully and any degradation of some of the dots can not degrade overall device performance.

In the following sections, firstly the structures and some optical properties of the SiO₂ will be given, since being the host its relationship with the guests is very important. And following that section the ripening procedures of nanocrystals in the oxide is examined without any tedious theory. After coarsening section the properties of silicon nanocrystals; optical properties, various emitted wavelength engineering techniques, temperature dependence of luminescent states and exciton migration effect, Si nanocrystal light emitting devices and its current voltage behaviors and lastly the memory property of nanocrystals will be shortly summarized.

3.1 SiO₂ and Properties

Silicon dioxide has been the one of the most intensively studied materials in material science and condensed matter physics. Since SiO₂ plays a central role in many of today's technologies, including fiber optics and satellite data bus applications, as the gate and field oxides in 95 % of all contemporary metal-oxide-semiconductor (MOS) devices, as windows, photo masks, and transmissive optics for ultraviolet-laser chip lithography, and as thin films for highly reflective (or highly transmissive) coatings for laser optics. Moreover, SiO₂ has been becoming an important host matrix for the formation of nanocrystal structures of many elemental and compound materials. Despite the technological importance of SiO₂ and the amount of studies done on defects, color centers, kinetics etc. many puzzles still remain.

The general name called *silica* comprising all compounds of silicon and oxygen with the composition SiO₂. These compounds are among the most abundant on the earth's surface and adopt a large number of possible polymorphic forms; cristobalite, tridymite, moganite, keatite, alfa- and beta- quartz, coesite and stishovite. The forms are determined by thermodynamic stability ranges; pressure, temperature, reaction dynamics etc. The phase diagram of SiO₂ is given in Figure 3.2. But all of these solids share a common composition, a common chemistry, and even (with the exception of stishovite) a common structural element: substantially covalent [SiO₄] tetrahedral unit; but they are

structurally very different [20]. Amorphous SiO₂ preserves much of the ordering present in the crystalline forms on a short or intermediate length scale. Some properties of both crystalline and non-crystalline forms are given in Table 3. 1. The origin of this surprising structural multiplicity lies in a parameter known as rigidity that related to the structural topology i.e. the ways of atoms or group of atoms connected together [21].

Table 3.1 compact polymorphic forms of SiO₂ [20]

Crystalline

polymorph	polytype	symmetry	density (gr/cm ³)
HP-Tridymite	[SiO ₄] tetrahedron	Hexagonal	2.18
MC-Tridymite	[SiO ₄] tetrahedron	monoclinic	2.26
β-Cristobalite	[SiO ₄] tetrahedron	Cubic	2.21
α-Cristobalite	[SiO ₄] tetrahedron	Tetragonal	2.33
β-Quartz	[SiO ₄] tetrahedron	Hexagonal	2.53
α-Quartz	[SiO ₄] tetrahedron	Hexagonal	2.65
Keatite	[SiO ₄] tetrahedron	Tetragonal	2.50
Moganite	[SiO ₄] tetrahedron	Monoclinic	2.62
Coesite	[SiO ₄] tetrahedron	Monoclinic	3.01
Stishovite	[SiO ₆] octahedron	Tetragonal	4.35

Non-Crystalline

form	polytype	formation T	density (gr/cm ³)
Vitreous silica	[SiO ₄] tetrahedron	1333 K	2.21
Metamict silica	[SiO ₄] tetrahedron	0-846 K	2.26

The basic bonding unit for all these form of silica except stishovite is the SiO₄ tetrahedron illustrated in Fig. 3.1. Four oxygen atoms surround each silicon atom with the Si-O distance ranging from 0.152 nm to 0.169 nm; the tetrahedral O-Si-O angle is

109.18°. Each oxygen is bonded to two silicon atoms, with the Si-O-Si angle varying from 120° to 180° depending on the form of the SiO₂. All forms are constructed from the corner-sharing tetrahedra as the SiO₄ building block, tetrahedral units connected together at the tetrahedron vertices through a common oxygen atom, but there are many ways to do so, in both regular and irregular arrangements. In crystalline forms, the tetrahedral arrangements are regular and exhibit long range orientational and translational order. For the amorphous structures orientational and translational invariances are relaxed slightly or totally with short order arrangements. The smaller the bond angle, the denser the possible packing; cristobalite and tridymite have the largest bond angles, and have the most open structures [22].

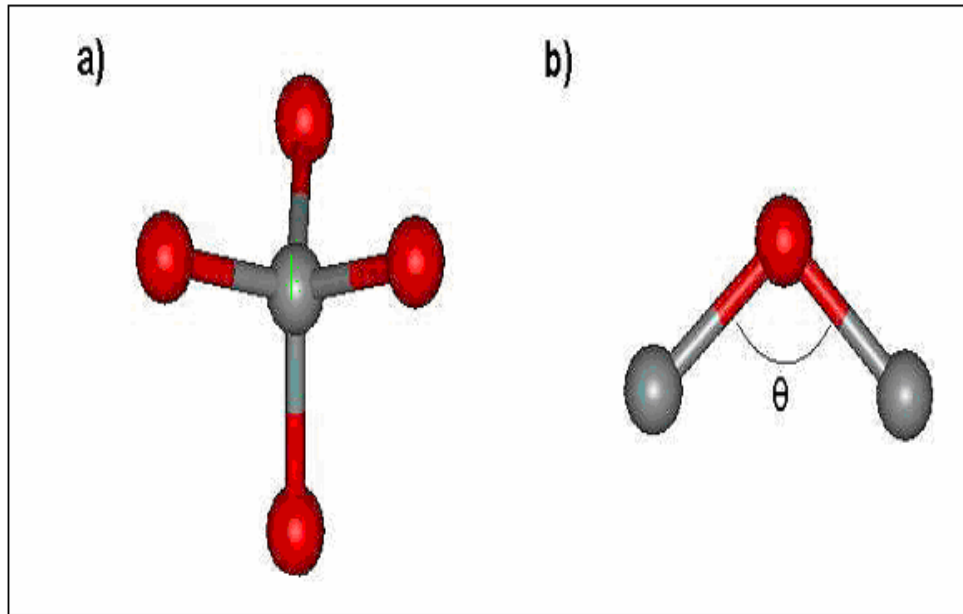


Figure 3. 1. (a) SiO₄ structural unit of most forms of SiO₂, showing the tetrahedral coordination. (b) Si₂O bonding configuration with Si-O-Si bond angle θ varying from 120° to 180° depending on the form of SiO₂

There are two model to describe the structure of amorphous SiO₂, continuous random network and microcrystalline model. In the first model, the local structural unit i.e. SiO₂

tetrahedron remains unchanged, and each tetrahedron corner shared with another tetrahedron (same in crystalline forms of SiO_2). However, the Si-O-Si bond angle will vary from one tetrahedron to another. In the second model, the SiO_2 is constructed from microcrystallites of the various allotropic forms of crystalline SiO_2 or alternatively, subunit cell sized crystallites of one form of SiO_2 . If the crystallites are so small, then continuous random network model and microcrystalline model converge to each other.

Today most of the studies on SiO_2 are about defects and their properties. Defects in SiO_2 can manifest their presence as e.g., by exhibiting luminescence and/or optical absorption bands or they may show themselves as charge trapping centers and detected electrically. Defects can be introduced in the manufacturing process or induced by ionizing radiation (X-ray, ultraviolet photons etc.) or particle irradiations e.g. ion implantation. If we consider the important applications above, it is easy to understand the control and the identifications of these defects could result in billions of dollars in cost savings to both photonics and semiconductor industries now and over the next decade.

There is some indefiniteness to describe the concept of a defect in amorphous materials. In crystalline case, long range orders are present which defines the perfection and any deviation from this perfection named as a defect. However, in amorphous materials, the concepts usually encountered in crystals (vacancies, interstitials, dislocations, etc.) are not well defined because the distance between neighboring atoms or the angle by any two pair of atoms does not have to follow any order. Amorphous SiO_2 is a network solid that is it composed of Si-O chains and rings. Every Si atom is four fold coordinated and every O atom is two fold coordinated and Si atoms always connected to O atom or vice versa, so in terms of any deviation or disruptions in this coordination and ordering can be defined intrinsic defects in SiO_2 [23].

There are lots of types of defects in silicon dioxide with exhibiting different behavior; some of them are luminescent centers at various color from red to ultra violet in the SiO_2 band gap, some of them are diamagnetic and others are paramagnetic; they exhibit different chemical reaction dynamics to the other species like photon, electron, other elements and to the temperature. In the identification and classification of these defects, electrical, magnetic, optical and combination of these methods are used depending on

the defect property. For example, defects with unpaired electrons are mostly studied with optical absorption/luminescence and electron paramagnetic resonance (EPR) together. In the framework of this study, only few absorbing and radiating /nonradiating (or luminescence bleaching) centers due to oxygen excess and deficiency in SiO₂ will be given shortly, the interested readers can look into the literature for more detailed explanation and the properties of oxide defects.

3.1.1 Oxygen excess centers

These centers are formed in SiO₂ either as excess number of oxygen or as displacement of oxygen by external excitations and radiations, such as ion implantation. The well known of this type center is oxygen dangling bond or non-bridging oxygen hole centers (NBOHC). This center can be visualized as the oxygen part of the broken Si-O bond in the oxygen excess SiO₂; O is bonded to single Si in the SiO₂ network. It is electrically neutral and paramagnetic and represents the simplest elementary oxygen related intrinsic defect in the oxide. With the collaboration of EPR and the optical spectroscopies, NBOHC ($\equiv\text{Si}-\text{O}\cdot$) is the best characterized intrinsic defect in SiO₂. This center has two absorption band at 1.97 eV and 4.8 eV and a luminescence band at 1.91 eV [24-26].

Other defects related with excess oxygen in the oxide are interstitial O₂ and O₃ molecules, peroxy bridges or peroxy linkages ($\equiv\text{Si}-\text{O}-\text{O}\cdot$, $\equiv\text{Si}-\text{O}-\text{O}-\text{Si}\equiv$) and ozonyl linkages ($\equiv\text{Si}-\text{O}-\text{O}-\text{O}\cdot$, $\equiv\text{Si}-\text{O}-\text{O}-\text{O}\equiv\text{Si}$). These defects introduce several absorption bands in to oxide at 4.8 eV, 7.6 eV, 6.4 eV, 1.6 eV and 0.98 eV and a peroxy related 2.25 eV luminescence band.

3.1.2 Oxygen deficient centers (or silicon rich sites)

Oxygen deficient centers can be generated by the excess silicon in the oxide or due to the lack of the homogeneous oxidation of silicon atom at the substrate surface as a result of difference in the chemical potential of Si and O atoms and morphology of the substrate and dielectric. The unoxidized Si atoms generally but not always contain

unsaturated valency, called as dangling bonds. Actually many defects can be described due to the oxygen vacancy depending on the coordination number of silicon and paramagnetism of the center, but three of them are well known: P_b center ($\text{Si}\equiv\text{Si}\bullet$) (P stands for paramagnetic) is the dangling Si bond at Si/SiO₂ interface and the dangling bond towards the oxide. P_b centers are electrically amphoteric [27], i.e. they act as electron donors as well as electron acceptors. This defect also plays a major role in the luminescence quenching of the silicon nanocrystals. The other two important oxygen vacancy generated defects are E' ($\text{O}\equiv\text{Si}\bullet$) and B_2 ($\text{O}\equiv\text{Si}-\text{Si}\equiv\text{O}$) centers having known absorption bands at 5.79 and 5 eV and luminescence bands at 3.1 and 2.7 eV [28,29].

The growth conditions whether SiO₂ dry or wet, can cause small variations in the absorption and luminescence wavelength of these defects. Furthermore the ambient (H, O, N and etc. incorporation after growth, electron and ion excitation or high energy photons) can cause elimination, formation or transformation of defects from one structure to another.

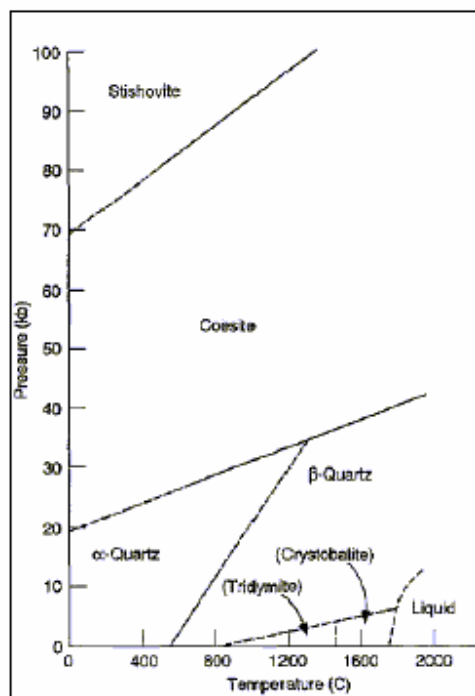


Figure 3. 2 Phase diagram of SiO₂ [22].

3. 2. Coarsening of Si Nanocrystals from Si Rich Oxide

Understanding and modeling of coarsening mechanisms or formation stage of nanocrystals very crucial to produce well described nanocrystal systems.

3.2.1 Ostwald ripening of nanocrystals

At the beginning of the twentieth century a biologist W. Ostwald discovered the ripening process in biosystems. However, his discovery had been forgotten for the time period of about six decades and at the sixties the theory was constructed by Lifshitz, Slyozov and Wagner [30, 31]. After them the theory has been elaborated and adapted to the formation dynamics of the almost all systems including the formation kinetics of the nanocrystals. Quantitative analysis of this theory requires detailed case by case modeling involving numerical methods. So formation stage of nanocrystal will be represented by simple qualitative explanations.

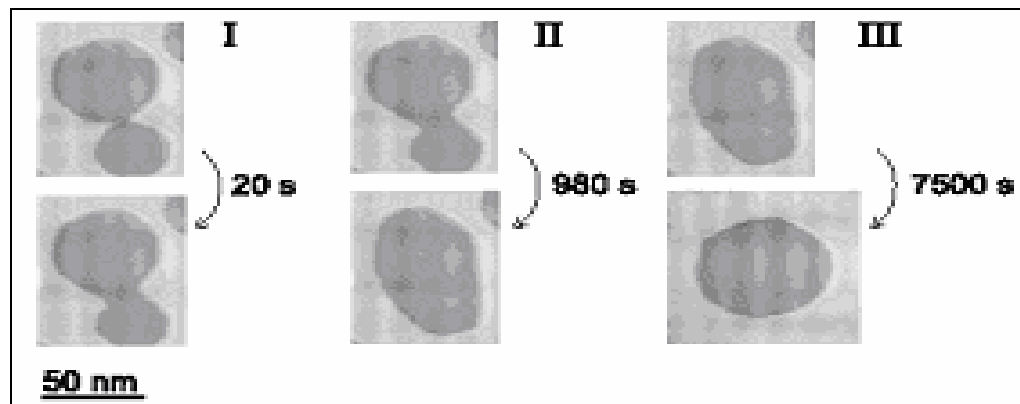


Figure 3. 3. Smoluchowski coalescence of islands on Ag. (I) island movement and collision (II) mass transferring and (III) relaxation from elongation to equilibrium shape [32].

In principle, actually there are two kind of ripening, Ostwald ripening and Smoluchowski ripening (or cluster diffusion) [32, 33]. Both Ostwald and Smoluchowski ripening clarify the increases in average size of islands, but there is a big difference in the way of ripening process. In Smoluchowski ripening mass transport occurs by moving island and the increase of island size is done by the process of the collisions of islands as seen in figure 3. 3. However in the Ostwald ripening the islands do not move, the growth occurs as the exchanging of atoms between small and big neighbor islands by detachment of atoms from smaller one and attachment to bigger one. In the coarsening of nanocrystals studies, Smoluchowski ripening is almost disregarded in the literature, so it will be disregarded also here.

In the past several models to study the Ostwald ripening process were developed, and all models have the distinction of a stationary precipitated phase and a dissolved phase in common. As a main disadvantage the diffusion either totally neglected, only roughly approximated or limited to one or two dimensions [34-36]. Today using very efficient numerical methods, it is possible to simulate Ostwald ripening accurately taking the influence of diffusion in three dimensions and large simulation volumes in to account. The model is described by the diffusion equation extended by a source term:

$$\frac{\partial C(r,t)}{\partial t} = D\Delta C(r,t) + Q(r,t), \quad (3.1)$$

where D is the diffusion coefficient of solute atoms, $C(r,t)$ is concentration of solute atoms at the position r at time t and $Q(r,t)$ is the change in concentration due to the absorption (attachment) or emission (detachment) of solute atoms by the precipitates. If D is assumed to be constant i.e. independent of local concentration, interdiffusion effects are neglected. The behavior of the precipitates described by a well known reaction equation based on the Gibbs-Thomson equation [37-39] under the assumption that precipitates are spherical with a fixed centre and lattice distortion energy is ignored.

$$\frac{dN_i(t)}{dt} = kN_i(t)^{2/3}[C(r_i,t) - C_{GT}(N_i)], \quad (3.2)$$

where $N_i(t)$ specifies the amount of particles in the precipitate indexed with i , k is a rate constant $C(r_i,t)$ is the concentration of solute atoms in the vicinity of the

precipitate positioned at r_i and $C_{GT}(N_i)$ is the Gibbs-Thomson concentration depending on the precipitates size.

To combine these two equations, $Q(r, t)$ in Eq. (3.1) is replaced by

$$Q(r, t) = \sum_{i=1}^p \delta(|r_i - r|) \frac{dN_i(t)}{dt} \quad (3.3)$$

The constant p is the amount of precipitates involved in the system. The multiplication with delta function leads to a localization of the absorbed and emitted particles from precipitates and islands.

The decrease in surface energy is usually assumed as the driving force for the Ostwald ripening, so that when two microparticles interact with each other by exchanging mass, the larger one grows at the expense of the smaller one. Because separation of phase occurs and new phase coarsens in order to lower the interfacial free energy [40]. Larger clusters or droplets are energetically more favorable due to their smaller interface curvature or smaller surface area to volume ratio. Thus they grow at the expense of smaller clusters which resolve again and finally disappear. This collective behavior leads to increase in average island size and simultaneously to decrease in the total number of inclusions. At the end, the system reaches full thermodynamic equilibrium. To handle the whole set of microparticles, precipitates or nanoclusters, it is generally assumed that the clusters (microparticles) are in the average environment, and there is a critical size, R_C , so that a microparticle larger than R_C always grow, and particles smaller than R_C will always shrink [41]. In this approach, three functions assumed independently acting on a set of microparticles. The first one, F_1 , concerns redistribution of mass to decrease the surface energy. This is achieved by taking an amount of volume of the smaller crystallites and adding to the larger one. The second one, F_2 , concerns redistribution of mass to increase the entropy of the system of microparticles and done by the opposite process of F_1 . And the third one, F_3 , is a further redistribution of mass that vanishes a microparticle. Once vanished, its mass is distributed among the bigger neighbors. F_1 and F_3 release energy, whereas F_2 absorbs energy and released energy by F_1 and F_3 should be available to sustain F_2 and any extra energy is released to the ambient.

In addition to the decrease of the surface energy, the collective behavior should also be taken into account through the entropy of the microparticle set i.e. its distribution between particles must be considered. To maximize the entropy, this distribution must be uniform, and the space distribution of particles should be uniform. Consequently, there is also an intrinsic tendency in the interaction of the particles to achieve all of them with the same size and form [42, 43].

A nano cluster releases mass (atoms) at a rate depending on its solubility in the matrix, but it also absorbs mass released by the other nanocrystals or clusters at a rate depending on its surface area (size), the concentration of emitted mass at its position and the reactions involved in the absorption process. The energy necessary to increase the surface area or size of the nanocrystal as a consequence of the absorption is supplied from the energy released when the surface area of another (the smaller one) is decreased due to the detachment of the atoms. Ostwald ripening can be considered in two mechanisms which are diffusion limited and attachment limited [44]. In the diffusion limited mechanisms diffusion of atoms away from or toward the islands is limited by some barriers. In the second mechanisms, all diffusion, attachment and detachment of atoms to the islands are limited. Both mechanisms can be described by chemical potentials. If clusters or any island described in ripening process is very dense, that situation generally occurs at the beginning of ripening, the main limit to the rate of the process is the attachment and detachment reactions at the surface of islands. As the ripening proceeds diffusion of atoms from small islands to larger one is become difficult and coarsening will be limited by diffusion process instead surface reactions. Therefore, if there is no barrier energy to limit the attachment of atoms to the islands, then we can say ripening process is diffusion limited on that surface.

3.2.2 Coarsening of silicon nanocrystals

For the formation of the Si nanocrystals in SiO₂ the first requirement is the super saturation of the oxide by the silicon atoms, as mentioned before it can be done in two ways; either during the growth of Si rich oxide or by high dose Si implantation in to the thermally grown oxide. It means that Si incorporation in to stoichiometric oxide must be

much higher than the solid solubility of Si in the SiO₂ to start phase separation of Si from the oxide for the nanocrystal evolution. And the second one is phase separation of Si by thermal treatment from the oxide.

When the dose of Si in SiO₂ exceeds 10²¹ cm⁻³ (~2 at %) with the average distance between Si excess atoms is around 1 nm [45]. For such doses or more, the distance between the most closely spaced Si atoms become comparable with the Si – Si bond length and atoms are in interaction with each other. Even without any thermal treatment Si – Si bonds can be formed resulting with small clusters or percolation chains. For the doses less than 1 at %, small cluster formation requires temperature enhancement.

Subsequent annealing is needed in phase separation of the Si from Si rich oxide. Since, thermal treatments can stimulate an onward growth of the induced precipitates up to the state of coalescence, where closed buried layers or nanocrystalline structures can be formed. In general, phase separation process is expected to be a sequence of few physical mechanisms; nucleation growth and Ostwald ripening of Si precipitates. This sequence is illustrated in Fig. 3.4. for the ion implanted case. All these mechanisms are the result of some randomly occurred elementary events like bond breaking, bond forming, diffusional jumps of atoms, chemical reaction etc [46].

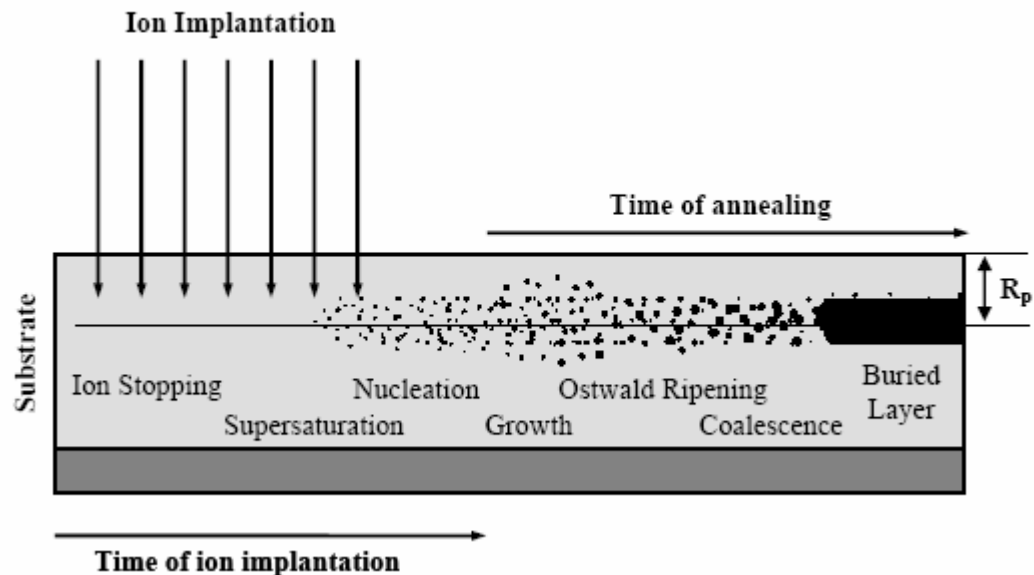


Figure 3. 4. Illustration of nanocrystal formation sequence of Si in the SiO₂ by ion implantation technique [6]

There are few parameters that effect the formation of nanocrystalline Si structures in SiO₂; annealing temperature, annealing time, initial excess of Si atoms etc. However there is an obstacle that, the diffusivity and the solubility of Si in SiO₂ are not well known. The diffusion coefficient of Si in SiO₂ is very low and assumed to be between 5×10^{-18} and 1×10^{-16} cm²/s depending on the temperature [47- 49].

Having such a small diffusion constant, the formation of Si nanocrystal in the oxide requires very high temperature treatments with long annealing time. Si nanocrystallites do not form below 900 °C annealing temperature and very long period of time is needed between 900 °C and 1000 °C. Therefore we can accept the threshold temperature for Si nanocrystal in SiO₂ is at least 1000 ° C [49-51].

For a fixed super saturation and temperature, the mean radius increases only very slowly when increasing the annealing time up to 16 hours. This very slow evolution is consistent with the low values of diffusion coefficient of Si in SiO₂ given above. When annealing time and Si excess are fixed, the mean radius is increased with the increase of temperature by decreasing of the nanocrystal density. At very high temperature annealing (over 1100 °C) the mean radius will be stable for some period of time of annealing because at this temperature there is a competition between the Ostwald ripening process and the dissolution of nanocrystal with migration of Si atoms to the substrate Si/SiO₂ interface. This Si loss to the interface decreases the density of nanocrystal, but Ostwald ripening is more effective than Si loss to the interface, so at the end, size of the nanocrystal will increase with decreasing number in the oxide. In the case of varying degree of supersaturation, as other fixed parameters (annealing temperature and time), both size and the density of nanocrystal increase with the concentration of excess Si. This situation can be easily seen for ion implantation method due to the Gaussian concentration distribution of the Si atoms. The highest concentration is seen at the peak of distribution and it decreases toward the tails at both sides, then one can expect that the larger nanocrystals will be formed at the middle of the implanted area and they reduce in size and density toward the tails in accordance with the concentration profile.

Imaging of Si nanocrystals embedded in SiO₂ is difficult because of the small difference of atomic number and the density between Si and SiO₂. As a result, these nanoparticles show only weak amplitude and phase contrast when imaged by TEM (Transmission Electron Microscope). Also having the Si substrate, Raman and XRD (X-Ray diffraction) spectroscopies are difficult to resolve the signal coming from Si nanocrystal and from the substrate. FTIR (Fourier Transform Infra Red) spectroscopy can give some information about the formation of nanocrystal by evaluating the varying signal of asymmetric stretching band of SiO₂ as a result of temperature treatment [52].

3.3 Optical Properties of Silicon Nanocrystals

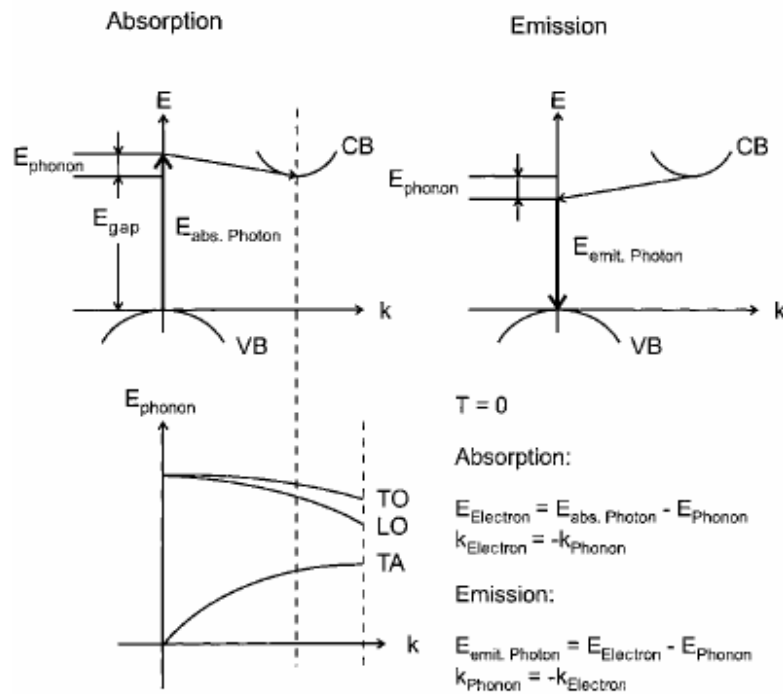


Figure 3. 5. Band structure of silicon, possible optical transitions and dispersion curve of phonon branches [54].

Before discussing the general predictions of the quantum confinement effect on the basic light emission/absorption behavior of Si nanocrystal in the oxide, it will be

meaningful to give general optical properties of bulk silicon. The simplified band structure of bulk Si is shown in Fig. 3. 5. The top of the valance band is located at the Γ point ($k=0$) at the center of Brillouine zone and six equivalent conduction band minima in the symmetries of $[53]$ directions, centered at the $\Delta = (0.85, 0, 0) \pi/a$ points. Where a is the lattice constant of Si. Therefore direct absorption and emission of light are impossible and require the emission or absorption of phonon to supply the discrepancy in the momentum between these extreme points. The only possible scenario for the optical transitions is the following: a photon causes a vertical virtual transition at $k=0$ (top of the Γ point) or $0.85 \pi/a$ with subsequent electron phonon scattering process. So with these secondary processes the probability of absorption and especially the emission of photons in the Si stay very low compared with any direct band material. Since the radiative time of indirect transitions are very long, excitons can travel very long distances in their thermalization process and the chance of finding nonradiative recombination channels become very high. The only possible direct transition is the Γ - Γ absorption of the photons ~ 3.1 eV between valance band maxima and conduction band maxima (not minima).

However, in the case of nanocrystalline structure of the silicon in SiO_2 due to the quantum confinement effect, the spatial confinement cause to spreading of exciton wave function in momentum space that result with the breakdown of k - conservation rule in Si nanocrystals. Therefore, no-phonon optical transitions become possible with increased oscillator strength which is directly proportional to the reciprocal space overlap i.e size of the nanocrystal. It is mentioned that for the same confinement energy no-phonon transitions are about three times stronger in Si nanocrystals in SiO_2 or having a SiO_2 shell [54, 55, 56]. Two effects of opposite nature can be accounted for the observed tendency depending on the quality of the Si- SiO_2 interface. First one is the carrier scattering at the Si nanocrystal oxide heterointerface, responsible for the suppression of the k -conservation rule and it is assumed to be strongly dependent on the interface abruptness. Second one is the confining potential (for a fixed size) is lower for a Si nanocrystal surrounded by SiO_x compound ($x < 2$) than SiO_2 . To achieve the same confinement energy, smaller size nanocrystals are required, giving rise to a relative increase of no phonon (NP) transitions. The lower confinement potential will lead to as

well to the smaller size dependent variation of the photo luminescence (PL) maximum [57]. To obtain good confinement effects, Si nanocrystals must be well separated from each other; there is a low limit of distance between neighbor nanocrystals to produce efficient emission.

Although Si nanocrystals have high PL yield, they behave as indirect semiconductors, keeping some properties of bulk Si with long radiative lifetime. In the photon absorption-emission cycle both NP and phonon mediated (1TA, 2TA, 1TO, TO+TA and 2TO) processes take place simultaneously. Therefore optical properties Si nanocrystals have to be considered on the basis of competition between indirect and quasidirect recombination channels [58]. As nanocrystal size goes to decrease, it can be predicted from the confinement theory that the probability of NP transitions should increase with respect to phonon-assisted (PA) transitions which imply the radiative oscillator strength and absorption cross section per nanocrystal are much larger for smaller size Si nanocrystal than larger ones [59]. However, it is rather complicated to find accurately the exact ratio of NP/PA transitions because the exact shape of the size distribution and the energy dependence of the absorption/emission in Si nanocrystal are not known. The major scaling parameter in all these effects is the size of the nanocrystal R [60, 61] and NP transitions are expected to be proportional to volume of crystallite inversely $(1/R)^3$, depending this expectation NP transitions begin to dominate at the confinement energies of the order of 0.65 – 0.7 eV.

In addition to the enhancement in the optical transitions in Si nanocrystal relative to the bulk case, the important feature related with the quantum confinement is the increasing of band gap energy as a function of the nanocrystal size. The band gap variation as a function of size can be simply written from confinement theory for three dimensionally confined Si nanocrystal as;

$$E(eV) = E_{bulk} + \frac{C}{R^2} \quad (3.4)$$

where E_{bulk} is the bulk silicon band gap, R is the dot radius, and C is the confinement parameter [62]. Therefore the expected result from the theory is that, as the size of the nanocrystal decrease there is a blue shift in both absorption and emission of the photons.

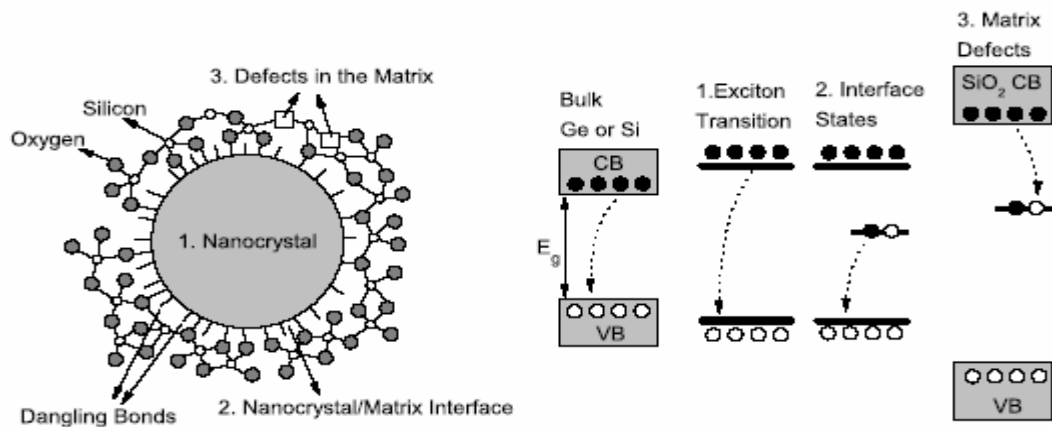


Figure 3. 6. Possible light emission mechanisms of Si nanocrystal SiO_2 system (1) recombination of electron-hole pairs in the nanocrystal, (2) recombination through radiative centers at the nanocrystal/ SiO_2 interface and (3) radiative defect centers at the matrix [6].

From the luminescence experiments, PL spectrum of wide range between 400 nm-1000 nm has been achieved from Si nanocrystalline structures in SiO_2 [62-66]. Except for few authors who claim all emission range come from nanocrystals, generally the emission range of 400-670 nm is attributed to the radiative defects at Si/ SiO_2 interface or directly to the oxide matrix and the range of 670-1000 nm emission attributed to the Si nanocrystals depending on their size and annealing temperatures etc.

The emission mechanism of light in Si nanocrystal systems remains unclear yet. There are two possible approaches: In the first one both absorption and emission of the light occurs in the nanocrystal and absorption/emission energy of the light is expected to be blue shifted with the decreasing size of crystallite. The optical emission of Si nanocrystal under optical pumping related through a series of processes; firstly, an electron is excited from the valance band to one of the higher lying electronic levels in the conduction band of the nanocrystal, leaving a hole behind. Subsequently these excited carriers relax to their minimum energy states to form a bound exciton in the Si nanocrystal in a picosecond time range. Then the exciton recombines accompanied by the emission of photon that gives the excitonic characteristics of the quantum dot states,

in a time scale of from tens of microseconds to several milliseconds [67]. In the second approach, it is suggested that; absorption occurs in the crystalline core of nanocrystal but the emission occurs radiative centers at the Si/SiO₂ interface of the nanocrystal. The possible mechanisms of the second approach are illustrated in Fig. 3. 6. Therefore contrary to the first one in which the exciton localization is in the nanocrystal itself that is the classical model for exciton recombination in semiconductor quantum dots, in the second one the created exciton or electron and hole can migrate to the surface states of the Si nanocrystals and localized there and recombine radiatively or non radiatively. Today the first approach is less appealing than the second one for Si nanocrystal grown in the oxide. Because experimental measurements have confirmed that the excitonic emission energy of Si nanocrystal increases as the nanocrystal size decreases, but the increase is much smaller than the expected theoretically, this discrepancy suggests the presence of excitonic recombination through localized states whose energy level lies within the band gap of smaller nanocrystals. Moreover, Si nanocrystals (NC) without an oxide protection matrix do not emit light in some experimental studies [68-70], this is also supporting the surface related radiative excitonic recombination. It is believed that the main luminescence peak around 800 nm is due to the Si=O bond and peak position can red shift or blue shift as a function of nanocrystal size.

In the extended version of the second approach, the system composed of three regions: nanocrystalline Si core, SiO₂ matrix and the bridge (suboxide) layer between nanocrystal and the oxide matrix. The interface between Si/SiO₂ is not sharp and there is a strained transition region most probably modified by the core Si dot. It is calculated that the Si – Si bond length is highly strained in the Si nanocrystal compared to the bulk case in the range of 14% to 33% [71]. Now the assumption become more clear as: The classical quantum confinement in Si nanocrystal does not work at all, it may work good for the case of the absorption of the excitation light i.e. as the size of the crystallite decrease the absorption threshold would increase, however, having the life time of in the order of the milliseconds the created excitons (electrons or holes) would be attracted to the Si core/ strained shell interface through the dipole-dipole attraction in the short range or by coupled to the long range field of polar optical Si-O modes due to the polar characteristic of the Si-O bond, or by thermally activated diffusion process, at the end

the attracted/diffused excitons localize at the interface or within the shell and recombine radiatively.

Y. Kanemetsu et al. [57] calculate the interfacial region band gap as around 1.6 eV, so when the core diameter less than 7 nm, the bridge shell would be energetically sandwiched between the Si nanocrystal and the oxide matrix which is the configuration of quantum well. So the model can be extended further as, let say two confinement with two interfaces: The first confinement is the quantum dot structure of Si core itself and the second one is the quantum well (quantum shell or nanoshell), the interfaces are nanocrystal/shell interface and shell/oxide matrix interface. The quantum confinement modify the Si dot bandgap depending on the size, then modified quantum dot can change the shell structure (also shell can affect the core self consistently) and the quantum shell structure most probably the main unit to determine the energy of the emission.

Now the origin of the emission from Si nanocrystalline system would become clearer in the following way: First the core nanocrystalline silicon absorb the light and carriers are excited, second the excited carriers transferred to quantum shell region and at the last step carrier recombine radiatively/nonradiatively in the strained well region. Thus the discrepancy between the theory and experimental result can be solved by this last approximation.

3. 4. Exciton Migration and Electron-Hole Exchange Interaction

Both exciton migration effect and electron-hole interaction are two important phenomena that strongly affect the optical properties of nanocrystal. These effects are experimentally determined by temperature dependent PL measurement.

2.4.1 Exciton migration in Si nanocrystal system

An exciton has not only having property of recombination radiatively and nonradiatively and also can migrate to another nanocrystal around them which have lower band gap energy than the donor one [72-75]. It is illustrated in figure 3. 7. with simple schematic. Due to their extremely long radiative life times of excitons in the

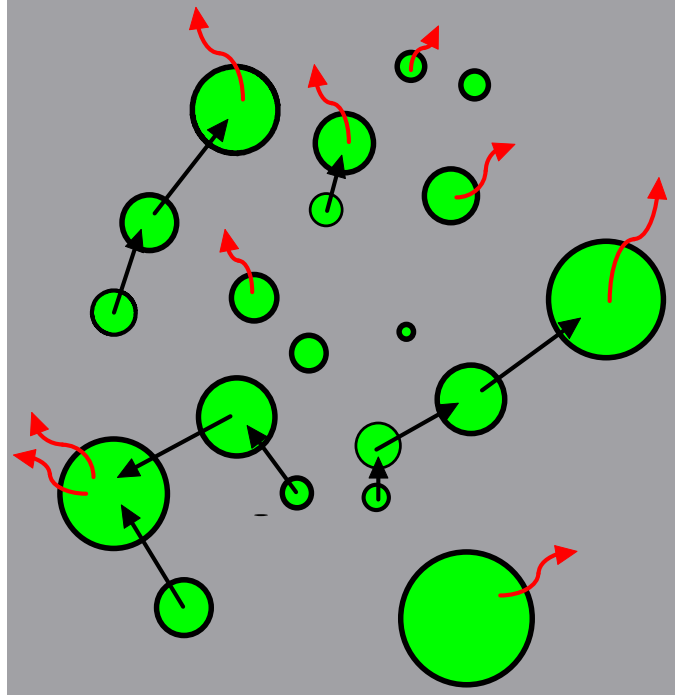


Figure 3.7. Exciton migration or energy transferring and exciton trapping in Si nanocrystals

broad temperature range, this process is favored for Si nanocrystals. Therefore the rate equation of exciton in nanocrystal can be written as:

$$\frac{dN_i(t)}{dt} = -\frac{N_i}{\tau_r} - \frac{N_i}{\tau_{nr}} - \sum_j P_{ij} N_i(t) + \sum_j P_{ji} N_j(t) \quad (3.5)$$

where τ_r is the radiative lifetime of the electron-hole recombination, τ_{nr} nonradiative lifetime $N_i(t)$ is the number of excitons in the nanocrystal i and P_{ij} is the migration probability of exciton from nanocrystal i to the j . The probability of this migration depends on the energy difference between these nanocrystal ΔE_{ij} and their distance (oxide barrier thickness) r_{ij} . Then the migration probability can be written,

$$P_{ij} = \nu \exp(-\gamma.r_{ij}) \quad \text{for } \Delta E_{ij} \leq 0 \quad (3.6)$$

$$P_{ij} = \nu \cdot \exp(-\gamma.r_{ij}) \cdot \exp\left(-\frac{\Delta E_{ij}}{k_B T}\right) \quad \text{for } \Delta E_{ij} \geq 0 \quad (3.7)$$

where ν attempt frequency of hopping of the exciton and the potential barrier due to the SiO_2 is involved in γ . This mechanism is called as trap controlled hopping mechanism and based on exciton migration between different nanocrystals. On the other hand, due to the higher band gap energy or the thickness of the oxide, several nanocrystals act as a trap acceptor for the exciton. It can be easily seen from Eq. (3.6) that, the exciton transfer from larger nanocrystal to the smaller nanocrystal is not easy. In the Eq. (3.7), the first exponential term is dominant in higher temperatures whereas the second exponential term is dominant at lower temperatures. In other words, at high temperatures, the migration of the excitons from small nanocrystals to the larger one is more probable, and at the lower temperatures nanocrystal will behave as exciton traps.

What would be the possible results in the PL spectrum of Si nanocrystal due to migration effects? Thermodynamically excited carriers want to be in possible lowest state, as the excited exciton energy is higher in small nanocrystals than the larger ones; the excitons have the tendency of populate the larger neighbors if they have enough energy to overcome the oxide barrier. Therefore, depending on the temperature, they can migrate by the assisting of the thermal energy, depending on energy separation ΔE_{ij} between them and the thickness of the isolation oxide. Then as the temperature is high, the emission of the larger nanocrystals dominates the PL spectrum because small nanocrystals further populate the larger ones at the expense of their depopulation. As the temperature goes to decrease, both exciton migration and non-radiative recombination rates would go to decrease as well, peak position of the PL spectrum will shift to the higher energy (blue shift) with increasing intensity.

This exciton migration process can also stretch the exponential time decay of the Si nanocrystal,

$$I(t) = I_0 \exp \left[-\left(\frac{t}{\tau}\right)^\beta \right] \quad (3.8)$$

where I_0 is PL intensity at $t=0$, $I(t)$ is the intensity at the time t and β is the dispersion factor (between 0 and 1) in the PL decay and the τ is the life time of the PL. Dispersion factor can be taken as the measure of the migration process. If the nanocrystals are totally isolated from each other, β will be unity with single exponential decay without considering other stretching effects.

3.4.2 Electron hole exchange interactions

The exchange interaction between electron and hole can be considered as a very weak perturbation and in bulk semiconductors it weakly changes the energy and the structures of the excitons. Exciton represents electron hole pairs bound by their coulomb attraction and by parallel spin exchange interaction. In the nanocrystals of direct band gap material, coulomb attraction merely shifts uniformly the energy of the lowest excitonic state, while the exchange interaction splits the excitonic line into a low lying forbidden (dark) state and a higher energy allowed (bright) state. Thus this gives rise to an absorption versus emission stokes shifts and it can be used experimentally to determine the exchange splitting energy of the excitons. However, for the case of nanocrystals of indirect band gap materials, the coulomb attraction already splits the excitons into spatially allowed and forbidden excitons. Exchange interaction leads to further spin splitting. This splitting is manifested both in the strong dependence of luminescence lifetime on temperature, and as an energy gap in the resonantly excited photoluminescence spectrum.

When the size of the nanocrystal approaches the bulk exciton radius, sharp enhancement of this effect is expected. So its value is proportional to the spatial overlap between electron and hole wave functions. The total angular momentum of the exciton may have $J=1$ or $J=2$ ($S=0$ or $S=1$) based on the mutual electron hole spin orientation. It has been recognized that electron-hole exchange interaction involved in the description of some basic properties of nanocrystal systems. It plays a crucial role to explain the size dependent stokes shift of the resonant PL and anomalous temperature dependence of the

PL decay time [76]. These states have different energies due to the exchange interaction, and the energy splitting is extremely size dependent, scaling with the inverse of third order of size. The state with $J=1$ ($S=0$ or antiparallel spins) is optically active since a photon can carry only the angular momentum one. The second state ($S=1$ or parallel spins) is dipole forbidden and stay in lower energy than the first one.

The upper and lower exciton states are assumed to be an optically active spin singlet ($S=0$) and optically passive or not allowed spin triplet ($S=1$) respectively, or shortly singlet and triplet. Exchange splitting energy in bulk silicon is very weak, around 150 μeV . However it has exhibited an important role in Si nanocrystal with splitting energy range of tens of meV because of the confinement depending on nanocrystal size. The radiative lifetime of a pure triplet state would be infinite, but the spin orbit interactions mixes some singlet character into the triplet state making transitions weakly allowed. Based on the effective mass approximation the exchange splitting energy can be written as [77]:

$$\Delta_{exch} = J \int |\varphi(r_e, r_h)|^2 d^3r \quad (3.9)$$

where $\varphi(r_e, r_h)$ is the envelope function for the exciton and J is electron-hole coulomb integral [78] and is defined as twice the exchange integral per unit inverse volume for the conduction band minimum and valance band maximum states in bulk silicon.

Excitons are mostly created in a singlet rather than a triplet state because the absorption strength is inversely proportional to the radiative life time and the singlet is 400 to 1200 times faster than the triplet state depending on the photon energy. At low temperatures, after a fast spin flip process the exciton relaxes to the forbidden triplet state with following electron hole annihilation.

This very small energy splitting cause to strong temperature dependence of the exciton lifetimes. When $k_B T \ll \Delta_{exch}$ only the lowest triplet state is occupied and the decay time is very long because of the optically forbidden character of this transiton. In the other extreme limit $k_B T \gg \Delta_{exch}$ both states are equally occupied and the transitions occur mainly through the fast singlet state. The overall temperature dependence of the exciton life time can be calculated on the basis of Boltzman statistics as:

$$\tau_r = \frac{3 + \exp\left(-\frac{\Delta_{exch}}{k_B T}\right)}{3\tau_t^{-1} + \tau_s^{-1} \cdot \exp\left(-\frac{\Delta_{exch}}{k_B T}\right)} \quad (3.10)$$

where three comes from the lower triplet state degeneracy, τ_r radiative life time, τ_s singlet state lifetime and τ_t is triplet state lifetime. As the rate is the inverse of the lifetime, by inverting the above equation, the radiative rate equation can be taken.

However, the equation above could not reflect the realistic case at all, for in which the surface polarization effects, thermal activated tunneling of excitons both migration between nanocrystals and to other surface related sites and lastly the Auger recombination dynamics should be included.

3. 5 Erbium (Er) Doped Si Nanocrystals

Erbium doped silica is widely used in telecommunication network as an optical amplifier for long range optical interconnections. The Er^{+3} ions produce light emission from the intra-4f transition (${}^4\text{I}_{13/2} \rightarrow {}^4\text{I}_{15/2}$) at around $1.54\mu\text{m}$, which corresponds to the minimum absorption in silica glass. However, the optical cross section for intra-4f transitions is quite small, typically on the order of 10^{-21} cm^2 . Therefore, it requires very high optical pump power to reach the population inversion.

Increasing the absorption crosssection of the Er^{+3} levels and combination with common Si based technology is very crucial for using erbium in integrated optoelectronics and Si microphotronics. In order to combine Er with Si technology different techniques were tested so far [79, 80]. One of them is discussed above. Er implantation into bulk Si gives quite high Er luminescence at $1.54\mu\text{m}$ at very low temperature. Excitons are formed at Er induced defects and transfer their energy to the Er ions through Auger process. Because this emission state of Er just below 0.15 eV lower than Si band gap the excited level of Er ions depopulated by thermal activation at higher temperatures back injected into the Si, since excitons cannot localize at the very shallow defect levels anymore as the temperature increase. This structure may be used as photo detector for the exact matching of the $1.54\mu\text{m}$ wavelength. It has been recognized that the, the most feasible solution would be the Er doped Si nanocrystal systems in the

SiO₂ by using nanocrystal as sensitizer. On the contrary Er in Si bulk, in this case back transfer of excited carriers suppressed by oxide layer between Er and nanocrystal by increased band gap of nanocrystal structures.

In addition to act as a sensitizer, it allows electrically pumped amplifier and source devices. Exciton mediated optical excitation of Er ions proceeds via absorption by the Si nanocrystals, generation of a confined carrier pairs, and rapid and efficient excitation exchange leading to luminescence from Er ions. Excitation of the Si nanocrystals is achieved through above band gap illumination; the transfer of excitation energy to nearby Er ions quenches the characteristic optical emission from the Si nanocrystals, and luminescence at 1.54 μm from Er ions is achieved. Due to the large absorption crosssection of Si nanocrystals at visible spectral region, the effective absorption crosssection of Er can be increased by up to fourth order as a result of the interaction without temperature quenching of Er emission. Thus large absorption crosssection allows the population inversion in Er systems with relatively low pump intensities. It is calculated that, one nanocrystal can excite 10 to 40 numbers of Er ions with a high transfer rate $R \geq 10^6 \text{ s}^{-1}$. When the excitons created inside the nanocrystal it can recombine radiatively, emitting a photon with an energy that depends of the nanocrystal size. However if an Er ion is located close to the nanocrystal, excitons can recombine nonradiatively by bringing Er ion into one of its excited state shown in Fig. 3.8. After a fast thermalization sequence, the luminescence of 1.54μm comes from ${}^4I_{13/2} \rightarrow {}^4I_{15/2}$ transition.

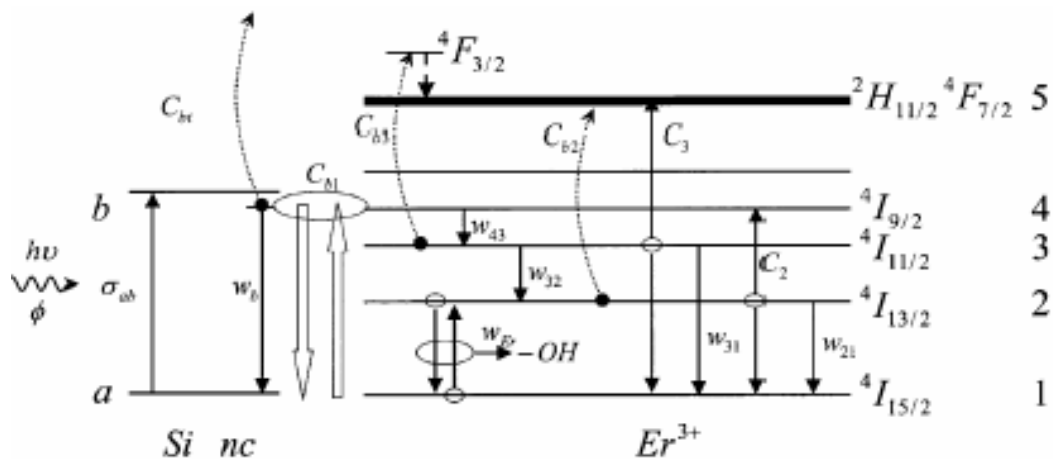


Figure 3.8. Detailed scheme of the Si nanocrystal interacting levels with the main physical processes [81].

In addition to act as a sensitizer, it allows electrically pumped amplifier and source devices. Exciton mediated optical excitation of Er ions proceeds via absorption by the Si nanocrystals, generation of a confined carrier pairs, and rapid and efficient excitation exchange leading to luminescence from Er ions. Excitation of the Si nanocrystals is achieved through above band gap illumination; the transfer of excitation energy to nearby Er ions quenches the characteristic optical emission from the Si nanocrystals, and luminescence at 1.54 μm from Er ions is achieved. Due to the large absorption crosssection of Si nanocrystals at visible spectral region, the effective absorption crosssection of Er can be increased by up to fourth order as a result of the interaction without temperature quenching of Er emission. Thus large absorption crosssection allows the population inversion in Er systems with relatively low pump intensities. It is calculated that, one nanocrystal can excite 10 to 40 numbers of Er ions with a high transfer rate $R \geq 10^6 \text{ s}^{-1}$. When the excitons created inside the nanocrystal it can recombine radiatively, emitting a photon with an energy that depends of the nanocrystal size. However if an Er ion is located close to the nanocrystal, excitons can recombine nonradiatively by bringing Er ion into one of its excited state shown in Fig. 3.8. After a fast thermalization sequence, the luminescence of 1.54 μm comes from ${}^4\text{I}_{13/2} \rightarrow {}^4\text{I}_{15/2}$ transition.

The energy transfer from Si NC to Er ion is partly limited by the number of optically active Er ion in the system. So there would be an optimum concentration of Er ion in the system and it is expected that it should be much less than $2 \times 10^{20} \text{ cm}^{-3}$. If the Er concentration exceeds this value, the luminescence of 1.54 μm is quenched in the favor of 980 nm emission (${}^4\text{I}_{11/2} \rightarrow {}^4\text{I}_{15/2}$ transition) of Er ion. This situation is called as up conversion or pair induced quenching as a result of the interaction between Er ions [82-85].

3. 6 Wavelength Engineering

One of the most important motivations of producing Si nanostructures in the oxide is to get very narrow and variable emission wavelength, as the outcome of the changing in dot size. However it is recognized that the emission has very broad range around the peak position, especially in the case of the nanocrystals produced by ion implantation technique, this broadening is much larger. So this is one of the problem that should be solved to produce efficient devices. There are mainly two reasons for this broad band emissions; the first one is the size distribution or maybe the shape variation of the nanocrystals in the oxide and the other one is the phonons or surface Si – O bond vibrations involvement in the optical transitions of Si nanocrystals. The phonon dependent broadening can not be inevitable as inert to the nanocrystal system of Si. However the size distribution can be minimized by some approaches especially for ion implantation case. One of them is implantation with low energy as will be explained in experimental chapter the implanted ion distribution is Gaussian and this distribution broaden as the energy of the implanted ions increase, so the large variation in the grown nanocrystal size. The larger nanocrystals located at the center zone of the distribution and decrease in size as going to the tails end at both sides. So when the implantation energy is decreased the distribution will be narrowed, followed by smoothing in the size distribution of nanocrystals. One of another potential solution is the sequential multi energy ion implantation. In this approach, the idea is to get constant ion distribution through the integration of few Gaussian profiles with different energy and dose in the implantation process. Therefore, as the size distribution minimized, then the broad emission band will be narrowed.

To change the peak position of the luminescence, lots of techniques can be used. In the case of ion implantation the dose and annealing temperature can be varied to change to change nanocrystal size. In addition, doping with other atoms and oxidation of nanocrystal surface are useful in particle size adjustment.

As explained in the ripening section, contrary to the Ostwald theory, the size of nanocrystal is independent of initial dose, the size of the nanocrystals increase with the initial excess Si or vice versa. When the size of nanocrystals are large/small depending

on the initial excess Si, the emitted wavelength of the light will be large/small as well. Respectively, again referring to that section by changing the annealing temperature and time, one could arrange the size of the nanocrystal, so the wavelength. These approaches could be applied all Si nanocrystal formation techniques mentioned before.

Oxidation of nanocrystals is very efficient way of wavelength engineering. As the samples with Si nanocrystal oxidized, in the first few minutes of the oxidation the PL signal increases up to four times of the initial value, due to the elimination of Si rich non radiative surface centers. As going on oxidation, there will be a continuous blue shift in PL peak position accompanying decrease in intensity. On the other hand, in a long duration of oxidation, as all Si nanocrystal will become oxidized then luminescence would totally quenched [86].

Ge doping of Si nanocrystal is another tool [87] in controlling the PL peak position. The wave length of the emission can be red shifted, without sacrificing the PL intensity, by an amount of 125 nm by increasing Ge doping concentration. Also indirect way of controlling Si nanocrystal emission can be achieved by doping of rare earth atoms and luminescence comes from doped atoms at the expense of the nanocrystal emission. For the case of Er doping discussed above the emission of 1.54 μm and 980 nm has been achieved efficiently. Depending on the doped atom species the energy of the emitted photons can vary.

3.7 Electroluminescence and Current-Voltage Characteristics

After having an efficient photo luminescence from the Si nanocrystal structures, a great deal of this effort will be focused on the fabrication of efficient and electrically driven room temperature light emission sources compatible with the integration of electronic and photonic devices in novel Si ULSI (ultra large scale integration) technology. Anticipated applications of Si nanocrystal based structures include an optical emitter for integrated optical circuits, logic memory and interconnects; electro optic isolators; massively parallel optical interconnects and cross connects for integrated circuit chips; lightwave components; high power discrete and array emitters; and optoelectronic nanocell arrays for detecting biological and chemical agents. There have

been some approximations to built Si light emitting devices; p-n junction diode, dislocation loop formation, rare earth doping the depletion region of Si p-n junction, porous Si microcrystalline structures, MOS structure with Si NC etc. Among, the most promising one is the nanocrystalline based MOS structure although its quantum efficiency still lower compared with its high efficient PL.

In traditional optoelectronic devices, the emission operation is based on the creation and annihilation of the electron hole pairs. In bipolar devices, electrons are injected from one side and the holes from the other side of the p-n junction, and they recombine in the depletion region or sandwiched active layer, producing photons under forward bias. In a unipolar device, the leakage of electrons in valence band or holes does not exist, so light must be produced by other means. In Si LED, this may be the case, since hole injection from Si valence band to the SiO₂ valence band is difficult because of the larger energy barrier than for electrons from metal to the conduction band, illustrated in Fig. 3.9. Any small difference in barrier height can result in huge difference in current; due to the fact that injected current exponentially depends on the barrier height, which situation makes the electron hole recombination much improbable. Although large amount of theoretical and experimental studies of Si NC present in the literature, only a few amount of articles have been reported on the electroluminescence (EL) characteristics, mainly due to mentioned difficulties of efficient carrier injection into an insulating SiO₂. Electroluminescence is explained by mechanisms that include field ionization of the luminescent centers, charge trapping and impact excitation by hot carrier and radiative recombination. In the model of the excitation, two conduction mechanisms have been mostly used for these structures; direct tunneling and Fowler-Nordheim (FN) tunneling. Having high threshold voltage of EL, around 8 V, the dominant mechanism is likely to be the tunneling of hot carriers (FN) from a nanocrystal to another one through insulating matrix. A way to reduce the high voltage requirement, is to narrow the oxide thickness. In this case, good quality oxide layers are needed to prevent the increasing leakage current near the breakdown operating conditions of oxide layer, and to produce enough hot carriers. However, high concentration of Si atoms is needed for generating enough efficient luminescence centers inside the oxide. Another disadvantage of the thin oxide layer is the reduced possibility of carriers to recombine radiatively. Because the

oxide is thinner, the numbers of nanocrystals in the direction of current flow is reduced. If the current injection occurs via percolation paths, it could be assumed that impurities near the oxide-silicon barrier may lower the voltages needed to inject holes to the oxide layer. In this situation, the trade off with higher doping of Si would be made at least with lower breakdown voltage. However, the reducing excess Si at the favor of threshold voltage will cause the reduction in the number of emitted photons.

Major current mechanisms, direct tunneling and FN tunneling are discussed, below there may also present other mechanisms as indicated in Fig. 3.9.

3.7.1 Direct tunneling

The direct tunneling is characteristics for very thin oxide layers (< 4 nm). The analytical equation that presents the current density passing through an oxide layer with thickness t_{ox} under an applied voltage V can be written as:

$$j = \frac{AE^2}{\left[1 - \sqrt{1 - \frac{qV}{\phi_B}}\right]^2} \exp\left\{-\frac{B}{E}\left[1 - \left(1 - \frac{qV}{\phi_B}\right)^{3/2}\right]\right\} \quad (3.10)$$

where $A = \frac{q^2}{2\pi\hbar}$ and $B = \frac{4\pi\sqrt{2m^*}}{h}$ (3.11)

ϕ_B is the effective barrier height, m^* effective electron mass in SiO₂, E is the electric field and q, h are the usual known physical constants. The direct tunneling is possible between Si nanocrystals and substrate to nanocrystals if the separation is less than 4 nm. For this case, electrons see a higher barrier than the voltage drop due to the SiO₂ and the barrier appears as trapezoidal form. The electrons, by this mechanism, can pass between a nanocrystal to another one and so move through the SiO₂ matrix.

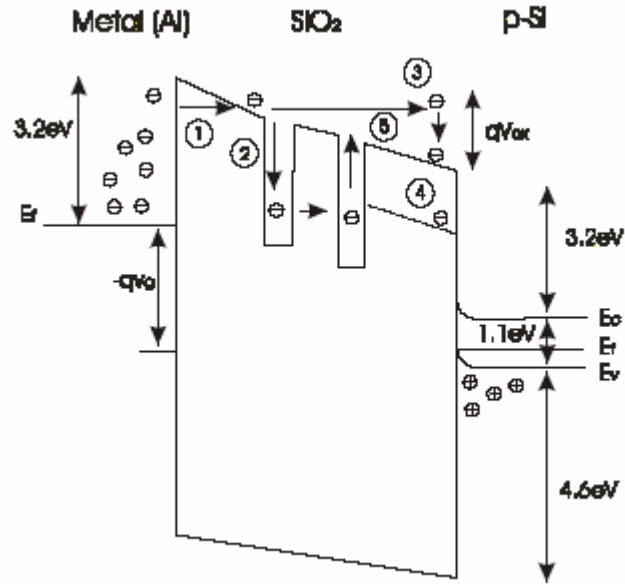


Figure 3.9. Transport mechanism in MOS structure: (1) Fowler-Nordheim tunneling, (2) trapping at cluster and tunneling from cluster to another, (3) quasi free movement of electrons within the conduction band of SiO₂, (4) hopping conduction, (5) Poole-Frenkel tunneling.

3.7.2 Fowler-Nordheim tunneling

Fowler-Nordheim tunneling in Si NC MOS structures has been studied extensively. It is assumed that, this is the dominant current injection mechanism into the SiO₂ matrix, especially for the thick oxide. The tunneling of highly energetic particles can occur by FN injection. The analytic equation for FN conduction mechanism is:

$$J_{FN} = \frac{A}{4\phi_B} E^2 \cdot \exp\left(-\frac{2B\phi_B^{3/2}}{3E}\right) \quad (3.12)$$

where constants A and B are the same given in the Eq. (3.11). The electrons pass through the barrier, due to the high electric field, which is the triangular barrier of oxide band under high voltage.

Actually the conduction and EL excitation mechanisms are not clear at all. Because, under high field levels, impact ionization may involve other mechanisms, therefore total

outcome could not be predictable both in transport and recombination channels. In transport side, the current mechanisms of normal oxide is directly applied to the oxide with nanocrystal. The micro or nanotransport between the nanocrystal always excluded and any current behavior depending on nanocrystal size is unclear. Further information about the EL properties of Si nanocrystalline LED will be given in discussion chapter.

3. 8 Memory Effects

Solid State nonvolatile memory devices (NVM) were first introduced at the late sixties, and commercial exploitation followed quickly. During the early growth stage of the industry, a dominant design emerged as floating gate (FG) device. Today, the stacked-gate FG device structure continues to be the most prevailing NVM implementation in both code and data storage applications. In such a device, Fig 2. 10, information stored in the form of charge in a polysilicon layer completely surrounded by dielectrics and located between the channel region and gate of a FET. The amount of charge stored on the FG layer can be easily sensed since it is directly proportional to the threshold voltage of the FET. Several physical mechanisms are available to accomplish the charge transfer from the substrate or towards the substrate. The most commonly used ones are either channel hot electron injection or FN tunneling for the write operation, and FN tunneling for the erase operation. The other widely used structure is the metal-nitride-oxide-silicon (MONOS) memory structures, in which, excess charges are stored in deep traps at or near the nitride oxide interface.

As the device packing density increases, lower programming voltages will be employed for memory cells. For the tunnel oxide technology, programming voltages can be reduced by thinner oxide involvement. However, limitations such as defect density, retention degradation and direct tunneling problem become more significant when scaling the oxide thickness. It becomes more difficult to achieve a desired lower programming voltage using polyoxides. The requirement is that, on the one hand, the tunnel oxide has to allow quick and efficient charge transfer by using low voltage low voltage for high speed operations. On the other hand, the tunnel oxide needs to provide superior isolation under retention to maintain information integrity over periods of up to

ten years. The hot carrier injection, after some time, cause the accumulated effects of repeatedly stressing the oxide alternate write erase operations, which at the end cause leakage to the substrate and lateral tunneling.

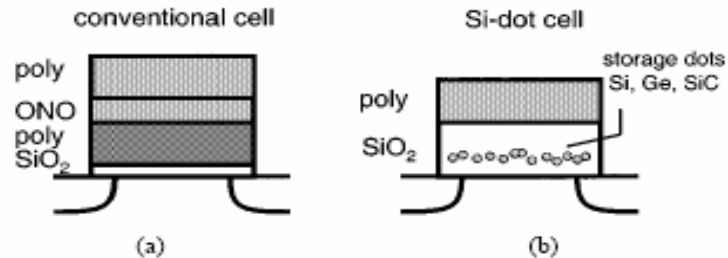


Figure 3.10. Simple schematic representation of; (a) conventional FG nonvolatile memory cell. (b) nanocrystal nonvolatile memory cell. ONO (oxide-nitride-oxide layer), poly is the polysilicon [88].

Nowadays, metal-oxide field-effect-transistor (MOSFET) memories based on Si nanocrystals operating at room temperature has been researched extensively, due to the promising applications in near future very large scale integrated circuits. In such memory structures, Si nanocrystals are used as charge storage elements embedded in the oxide layer between the control gate and the source-drain conduction channel. Charge injection takes place by direct tunneling from the Si substrate and is controlled by applying a voltage bias to the gate. A nanocrystal memory offers several attractive characteristics in comparison to current floating gate technologies, for example, fast write erase times at smaller injection voltage, extremely small degradation due to the absence of hot carrier injection from the substrate, long retention times, smaller lateral leakage current and inherent scalability even down to single electron devices [89-91].

Figure 3.11. Shows a schematic cross section and band diagram during injection (write cycle), storage and removal (erase cycle) of an electron in the device having p-type substrate (or n-channel FET). A thin tunneling oxide separates the inversion surface of silicon FET from distributed film of nanocrystals of Si that covers the entire surface channel region. A thicker control oxide separates the nanocrystals from the control gate. An injection of an electron occurs from the inversion layer through direct tunneling

when the gate is forward biased with respect to source and drain. Then the resulting stored charge in the nanocrystals screens the gate charges and reduces the conduction in the inversion layer, which means that these charges effectively shifts the threshold voltage of the device to be more positive, and this shifts can be approximated by under the assumption of each nanocrystal stored only one electron as:

$$\Delta V_T = \frac{qn_{well}}{\epsilon_{ox}} \left(t_{cntl} + \frac{1}{2} \frac{\epsilon_{ox}}{\epsilon_{Si}} t_{well} \right) \quad (3.13)$$

where ΔV_t is the threshold voltage shift, t_{cntl} control oxide thickness, t_{well} linear dimension of nanocrystal well, n_{well} is the density of nanocrystal, ϵ is permittivity and q is electronic charge magnitude.

In the production of these devices the main challenge is the formation of nanocrystals enough close to the channel without compromising the integrity of the gate oxide and the quality of the interface with the substrate and also nanocrystal itself. Although, it is assumed that the interface defects at Si NC oxide can play a role in the charge trapping process, they can degrade charge retention through allowing back tunneling of the stored charge.

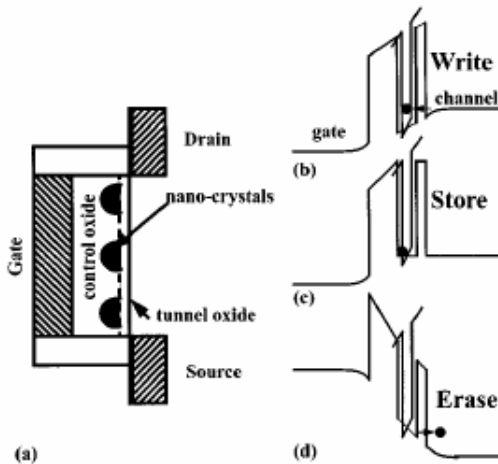


Figure 3. 11. (a) schematic cross section (b) band diagram during injection (c) storage (d) removal of an electron from a Si nanocrystal [92].

CHAPTER 4

EXPERIMENTAL PROCEDURES

For the fabrication of EL devices, two different types of silicon substrates were used; P- type Si substrate with 40 nm thermally grown oxides and n-type Si substrate with 100 nm thermal oxide. Experimental studies can be divided into to three main topics; sample preparation, device fabrication and the characterization of the devices. Under each topic, all the followed steps will be explained.

4.1 Sample Preparation

In this part of the study, the samples were firstly implanted with Si ions with different doses and energies depending on the oxide thickness on the Si substrates. For 100 nm oxides two different samples (both are n-type) named as M2 and M3 were implanted with the same dose of $5 \times 10^{16} \text{ cm}^{-2}$ at 40 KeV and 50 KeV ion energy of Si. For 40 nm oxide two different set were used (both are p-type) given the identity as M1 and M4, implanted with the same ion energy, but having different doses. In Table 4.1 all parameters of the samples can be seen.

4.1.1 Ion implantation

Ion implantation is the introduction of controlled amount of energetic, charged particles into the solid substrate with ions energy of KeV to MeV energy range. By introducing such impurities, mechanical, electrical, optical, magnetic and superconducting properties of the host material can be changed in a desirable way. The main advantages of ion implantation technique are; its more precise control on the total number of doped atoms with good reproducibility; wide dopant concentration range, independent control of penetration depth from the dose; lower processing temperature requirements compared to those of other techniques such as diffusion process; less sensitive to surface cleaning procedure; flexibility to large material and dopant selection

and excellent lateral dose uniformity which is very important today micro electronic production line. The major disadvantage is the creation of damage due to the ion bombardment. Damages can be reduced or recovered by the subsequent thermal annealing.

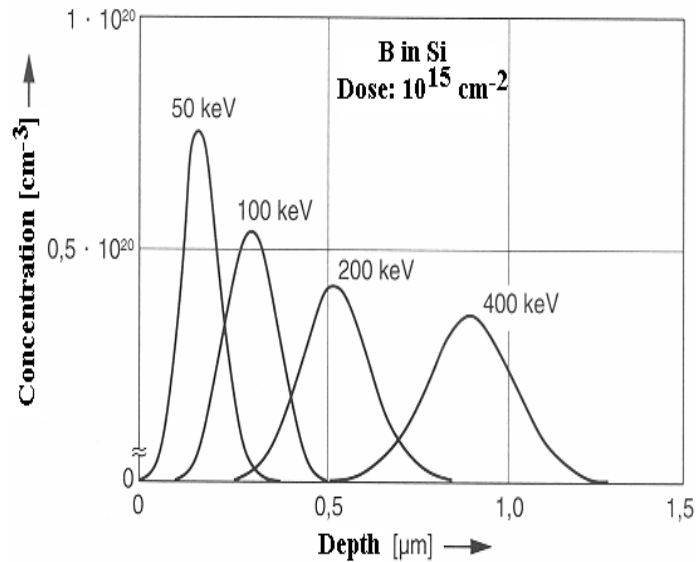


Figure4. 1. Distribution of B in Si with varying implant energy

The energetic ions lose their energy through collisions with electrons and nuclei in the substrate and finally come to rest. The total distance that an ion travels in coming to rest is called its range R . The projection of this distance along the axis of incidence is called the projected range R_p . Since the number of collisions per unit distance and the energy lost per collision are random variables, there will be spatial distribution of ions having the same mass and the same initial acceleration energy. The statistical fluctuations in the projected range are called projected straggle ΔR_p . There will be also a statistical fluctuation along the axis perpendicular to the axis of incidence.

Along the axis of incidence, the implanted ion profile can be approximated by a Gaussian distribution function:

$$n(x) = \frac{S}{\sqrt{2\pi}} \frac{1}{\Delta R_p} \exp\left[-\frac{(x - R_p)^2}{2\Delta R_p^2}\right] \quad (4.1)$$

where S is the ion dose per unit area. The depth and distribution profile of the implanted atoms within the substrate depends on energy and mass of the ions and also depends on the substrate used. The change in distribution is given for different energy with the same dose for B in Si Fig. 4.1. [93, 94].

4.1.2 Applications of ion implantation

- Doping of impurities into both unipolar and bipolar devices in the microelectronic industry
- In the field of new material synthesis on selected area
- Surface treatment and hardening of metals
- In etching and sputtering facilities
- Adhesion of glass substrates
- SIMOX processing
- In the area of nanocrystal formation of group four and other metal and compound semiconductors in SiO₂ and other matrix material [95-97]. However, the drawbacks of implantation process for this purpose are difficulty of controlling distribution and the profile of the light emitting or light bleaching defects inside the matrix.

4.1.3 Implantation system

In the implantation processes Varian DF4 ion implanter that allow the ion energy in the range of 5-200 KeV, was used. In Fig. 3. 2. Overall schematics and the major components of the implantation system are illustrated. Generally, implantation system consists of three main units; source, beam line and the end station. All these regions are pumped through diffusion pumps that are backed by the mechanical pump. The high vacuum level so important to eliminate the neutralization of implanted species. In the implantation process, the vacuum level of around 1×10^{-7} Torr was achieved.

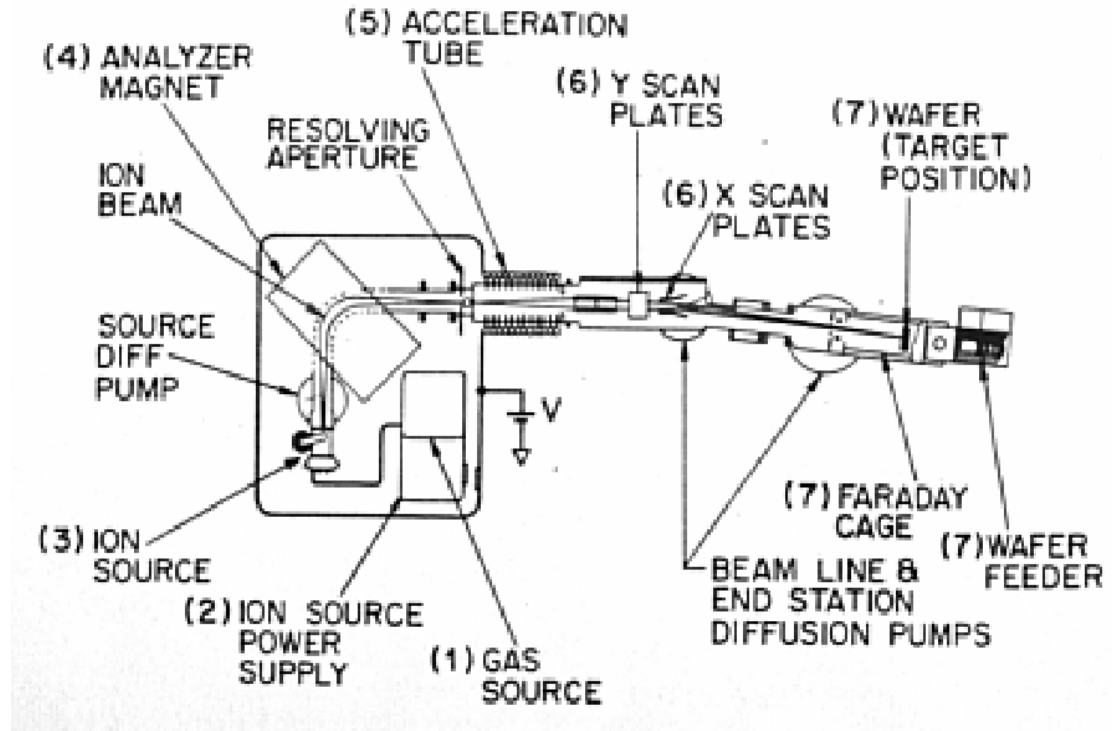


Figure 4. 2. Basic schematic of ion implantation system from top view

In the source region, plasma formed in the molybdenum chamber by the electron emission from the tungsten filament by passing through large amount of current (~150 A) on it. The ionized atoms then extracted by a potential difference of 25 kV and plus the 2 kV to reject the escape electrons, at the end total extraction voltage is 27 kV. Both solid and gas sources can be used for the plasma formation. In this study SiF₄ gas was used for Si ion source. The extracted ions having the energy of 27 KeV, pass through analyzer magnet to separate the desired ions using their mass and charge by changing the magnitude of the magnetic field. Because not only the desired atoms are extracted but also other ion species and high order ionized atoms also extracted, they have to be separated.

In the beam line unit, the ions exit the magnetic analyzer accelerated by a potential up to 200 KeV. In the deceleration mode for low implantation energy, this potential applied oppositely to decelerate the ions. Through the beam line section, the distribution of

beams can be controlled in the X-Y direction by applying dc voltage. There is a 7 degrees bent in the way of the beam line section to prevent the neutralized ions to reach the target in order to get rid of excess atom implantation, the constant applied voltage bent the ionized species seven degree and neutralized ones cannot deflected, and stopped at the bent region.

End station is the region of the implanter where wafers are installed for implantation. The accelerated ions at the end inserted into the substrate and measured by the dose processor.

4.1.4 Simulation of ion distribution for the samples

For the distribution of Si ions in the SiO₂, SRIM 2003 code were used, that allow anybody to simulate any kind of atom in any target material. Target material can be single or stacked layers of few different materials. SRIM code is actually Monte Carlo simulation of 99999 ions inserted into target one by one considering the stopping mechanism at the end gives the desired statistical distribution of the implanted atoms.

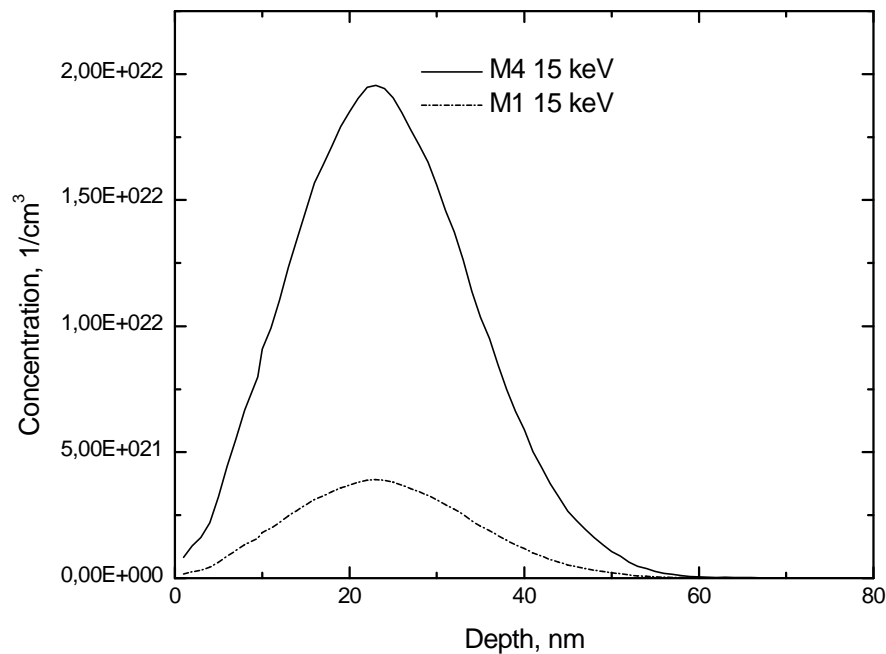


Figure 4. 3. Simulation result of the Si atoms for the samples series of M1 and M4 having the oxide thickness of 40 nm, the simulation energy of 15 KeV was chosen. The peak concentration of implanted ions is at the depth of ~ 23 nm from the SiO₂ surface.

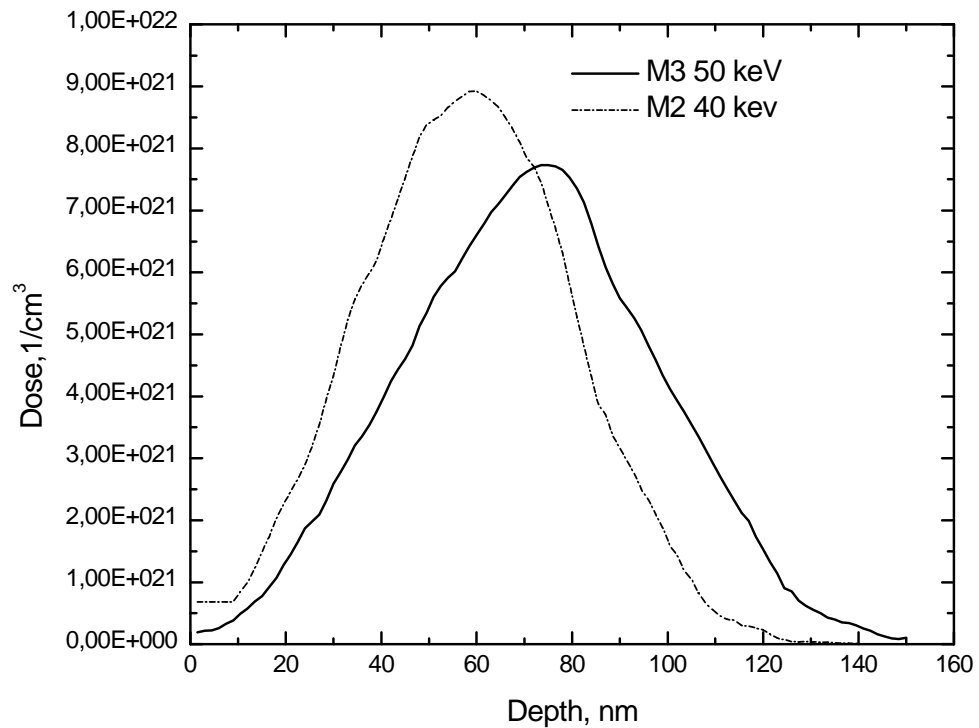


Figure 4. 4. Simulation result for the samples series of M2 and M3 having the thickness of 100 nm. Si ions were implanted with the energy of 40 KeV and 50 KeV with the peak positions are 60 and 72 nm respectively measured from SiO₂ surface.

When the ion coming to the target surface, depending on its mass, energy and the type of the target material it lost energy via consequent scattering events randomly and at the end stopped in the target by giving all its kinetic energy.

4.1.5 Annealing Procedure

Following the implantation procedure, each set of sample was cut with the diamond scriber into four parts, and one part left as implanted reference sample, other three parts were annealed under the nitrogen atmosphere except the sample with name 2VM1150 which was annealed under the vacuum level of 2.5×10^{-5} Torr. The nitrogen atmosphere prevent the further oxidation of the sample, if it is very pure, nitrogen is inert at the temperature up to 1200 °C unless catalyzing agents exist in the sample or in the environment. The furnace used in the annealing process is standard three zone resistively heated quartz furnace. The annealing stage is required for the formation of the nanocrystal, it is expected that, the threshold temperature for Si nanocrystal in the SiO₂ is at least 1000°C. Details of the annealing parameters of the samples are given in the table below.

Table 4. 1. Physical conditions of the prepared samples for the device fabrication

Series	Sample name	energy KeV	ion dose cm ⁻²	Anneal Temp °C	Anneal Time (h)	Oxide thickness (nm)	Substrate type
M1	2NM1900	15	1×10^{16}	900	2	40	p
	2NM11050	15	1×10^{16}	1050	2	40	p
	4NM11050	15	1×10^{16}	1050	4	40	p
	2VM11050	15	1×10^{16}	1050	2	40	p
M2	M2 AS	40	5×10^{16}	—	—	100	n
	2NM2900	40	5×10^{16}	900	2	100	n
	2NM21050	40	5×10^{16}	1050	2	100	n
	4NM21050	40	5×10^{16}	1050	4	100	n
M3	M3 AS	50	5×10^{16}	—	—	100	n
	2NM3900	50	5×10^{16}	900	2	100	n
	2NM31050	50	5×10^{16}	1050	2	100	n
	4NM31050	50	5×10^{16}	1050	4	100	n
M4	M4 AS	15	5×10^{16}	—	—	40	p
	2NM4900	15	5×10^{16}	900	2	40	p
	2NM41100	15	5×10^{16}	1100	2	40	p
	4NM41100	15	5×10^{16}	1100	4	40	p

4.2 Cleaning Procedures

After the annealing of the samples, the cleaning procedure given below was followed.

- Boiling in trichloroethylene (TCE) about 10 minutes
- Ultrasonic bath in acetone about 10 minutes
- Ultrasonic bath in isopropanol about 10 minutes
- Ultrasonic rinse in de ionized water around 10 minutes two times
- Drying with N₂ gas

4.3 Device Fabrication

In the device fabrication, the first step is the removing the oxide at the unimplanted side of the silicon substrate for metallization of the back contact by 30 % HF solution. After the oxide etching, below steps were performed

- Metal back contacts; aluminum (Al) for p-type substrates and gold-antimony (Au-Sb) for n-type substrate, were evaporated. Standard resistive thermal evaporator was used for aluminum and electron beam evaporator was used for the gold-antimony metallization. The vacuum level for the both system was around $2-3 \times 10^{-6}$ Torr at the time of evaporation. The thickness of Au contact is 750 nm, in the case of Al contacts the thickness was not known, but expected around 1 μ m.

- Metal evaporated samples annealed in the quartz furnace around 20 minutes, in order to diffuse the metal atoms into the substrate for good ohmic contact. Annealing temperature for Al ~ 400 °C and for Au-Sb ~ 500 °C.

- ITO (indium tin oxide) was grown on the implanted side of the samples having the thickness of 150 nm. ITO sputtered through the copper shadow mask included arrays of dots with 3 mm diameter. The aim of using ITO is to make transparent window for light extraction and spreading the current all over the device area. ITO is good transparent material between 400 and 1100 nm with an efficiency of 90 %. Only for the M3 series of

the samples, Au window with thickness ~ 30 nm were evaporated using electron beam evaporator.

- To increase the conductivity of the ITO window, samples annealed at ~ 380 °C around 30 minutes. And for the Au window, annealing temperature was ~ 500 °C in a time period of 15 minutes.

- Top contacts were deposited via copper shadow mask, co centered with the optic windows, having diameter of 1 mm.

- Using silver paste, devices were mounted on to the printed circuit board (PCB), and using gold wire, connections were taken from top contact to the PCB board.

4.3.1 Design and making of copper shadow masks

Shadow masks used for both optic windows and top contacts made by using 0.3 mm copper sheet. The description of steps for making mask is:

- Masks were designed by using Microsoft VISIO 2003 drawing software. Two kinds of masks have designed; mask having 3 mm diameter dot arrays for optic window and arrays with 1 mm dot diameter, shown in Figure 3.5.

- Designed masks printed on to the transparency

- Under ultraviolet light in the dark room, patterns transferred to the serigraphy silk covered with negative photo emulsion

- The patterns on the silk transferred to the copper sheet. In the transfer process, serigraphic acid resistive ink diffused through the silk to the copper sheet by using rakle. Other side of the copper covered with same ink and dried.

- The patterned copper sheet etched in the hydrogen peroxide- water- hydrochloric acid solution and the remaining part of the copper sheet dropped in to acetone in order to clean the ink resist.

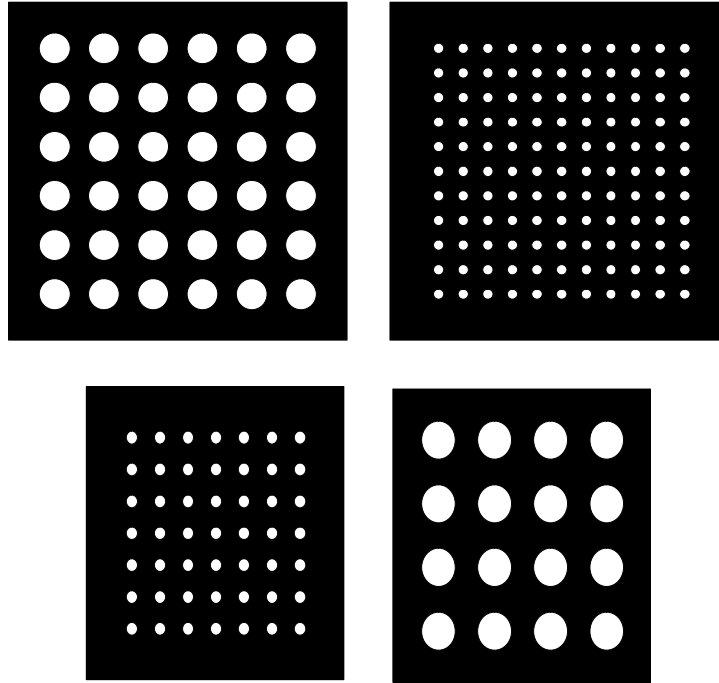


Figure 4.5. Copper shadow masks used in fabrication of the devices, larger dots for optic windows and smaller ones for top contacts.

4.3.2 Device Schematic

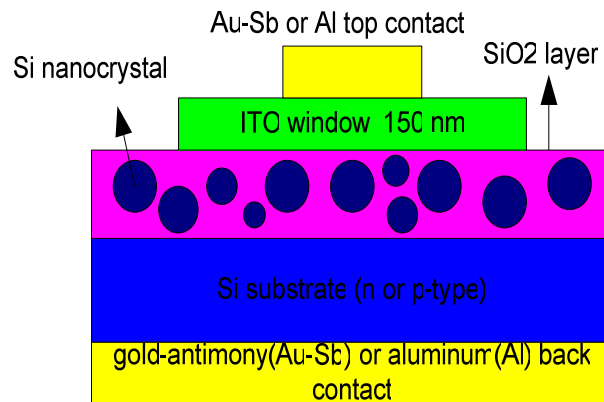


Figure 4.6 Cross section of the fabricated light emitting device structure. Back and top contacts are Au-Sb for n-type substrate, Al for p-type case.

4.4 Device Characterization

In the characterization of the fabricated devices, both optical and electrical methods were used. Firstly, PL measurement was performed before fabrication of the devices using continuous mode 532 nm duplicated NdYAG laser as an excitation source. Absorbed laser light create excitons in the Si NC, then the emission from radiative recombination of excitons was measured. The measurement system used in PL characterization consist of; excitation source as Nd YAG laser (it can be other lasers and any light source as well that have larger photon energies than the band gap of Si NC), MS-257 type monochromator of Oriel Instrument Company and Hamamatsu CCD camera for detecting the emission. Gathered data from the measurement corrected according to sensitivity of the CCD camera and grating in the monochromator.

For the I-V measurements Hewlett-Packard 4140 B Pico Ampermeter/DC voltage source was used in both polarity of bias to devices. By this I-V set up current level up to 10 mA can be measured, any current level larger greater than this value limited by the set up. In the measurement both forward and reverse bias applied to devices up to 10 V, higher applied bias voltage rarely applied as the current limited by the Pico Ampermeter.

In EL measurements, same set up used as in the case of PL. In the EL measurements, dc voltage source was used as an excitation source with an applied output voltage between 0-35 volts. To align the devices to the input port of monochromator He-Ne laser was used. Measurements conducted by applying both forward and reverse bias between bottom and top contact using load resistor of 47 ohms.

CHAPTER 5

RESULTS AND DISCUSSIONS

In this chapter, experimental results of the samples and devices will be presented with discussions and analysis. PL results of the all samples in Table 4.1 will be discussed in the first section. In the second section current-voltage (I-V) results of three MOS device series (M1, M2, and M4) will be given and discussed qualitatively. Excluding M3 series samples with gold optical window, electroluminescence (EL) results observed from different sample types will be presented and emission generated in the EL process will be compared with the PL results.

5. 1. Photoluminescence (PL) Results

PL spectroscopy is one of the simplest and non-destructive method used for the characterization of Si nanocrystals (NC) in the oxide matrix. By illuminating a suitable light source, electron-hole pairs are created in the NC. When these electron hole pairs recombine radiatively, photons with energy equal to the difference between two energy levels is created. By measuring the spectrum of the released photons the life time of excited carriers, type of recombination, etc. can be depicted.

Although intensive experimental and theoretical researches have been conducted on Si NC in the oxide, the light emission mechanisms still remain unclear. There are three models being discussed today: recombination of excited excitons in nanocrystal, recombination through defect levels in the oxide or recombination at Si NC/SiO_x interface and strained shell region between core NC and SiO₂ matrix [98-101]. However it should be noted that these three mechanisms can not exclude each other, i.e. all can exist at the same time.

The broad light emission from Si NC in the oxide matrix is usually observed with a wavelength range from 400 to 1000 nm. The emission bands between 400-700 nm are attributed to the defects in the oxide matrix as a result of deformation in the oxide structure. The other band in 700-1000 nm is attributed to the recombination in Si NCs.

The peak position of this band can be varied depending on the size of NC through quantum confinement effect: as the NC size increases wavelength of emission also increases towards 1000 nm, namely showing a redshift in the emission spectrum.

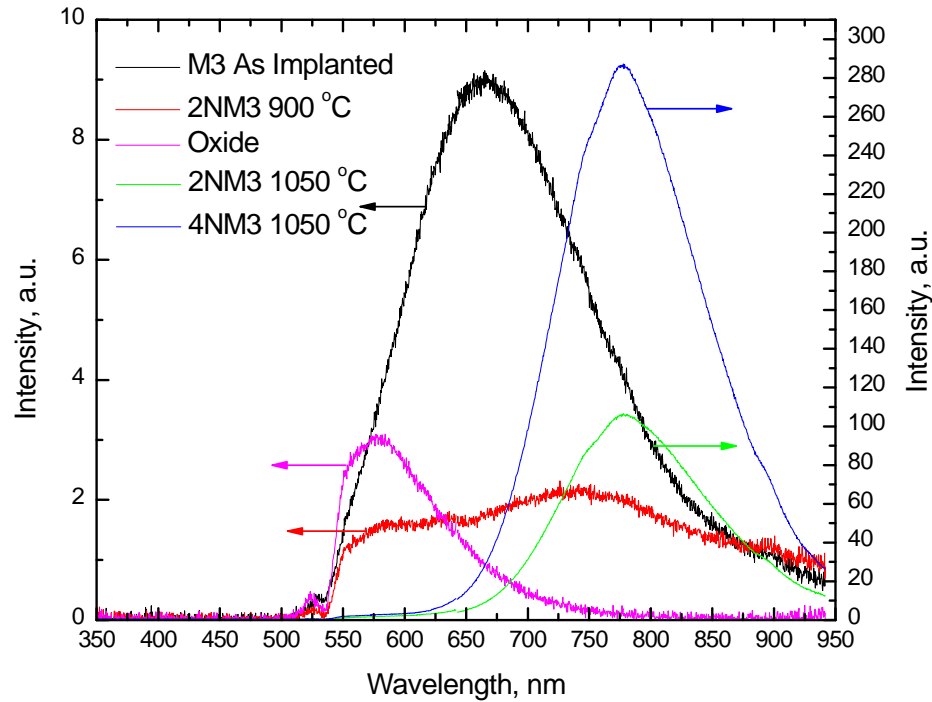


Figure 5.1. Room temperature PL results of the sample series M3 (n-type Si substrate with 100 nm thermal oxide) annealed at different temperatures and duration. Arrows on the spectra indicate corresponding scale. Implanted Si dose is $5 \times 10^{16} \text{ cm}^{-2}$ with implant energy of 50 keV.

In Fig. 5.1. PL spectra obtained at room temperature from M3 samples annealed at different temperatures for different duration are given. It is seen that, the virgin oxide has an emission band at around 570 nm. This band is less studied band in Si NC/oxide system, due to lack of reliable information on the possible sources for this emission band. When comparing with the energy of the known defects types it coincides with peroxy-radical defects due to high oxygen content in oxide, as evidenced by Barthou et al. and Sakurai et al. [26, 53]. In the as-implanted reference sample, very broad emission

band is observed with the main peak at about 650 nm, which comes from well known non-bridging oxygen hole centers (NBOHC) [53,102] formed as a result of Si implantation. When as-implanted sample is compared carefully with the sample annealed at 900 °C, it can easily be seen that, emission from as-implanted sample is composed of two defect related spectra, i.e., peroxy radicals and NBOHC. Upon annealing the samples at 900 °C for two hours, intensity of peak at ~ 650 nm decreases and a new peak at ~ 745 nm with relatively low intensity emerges. It is very much likely that the annealing at 900 °C suppresses NBOHC and enhances the formation Si crystallites. The new peak seen at 745 nm can then be attributed to the presence of the small crystallites surrounded with Si rich oxide. Sharp decrease in intensity at 650 nm can be due to formation of P_b or any luminescence quenching defects around small clusters at the expense of NBOHC. When the annealing temperature is increased to 1050 °C, it is expected that NCs are formed in oxide matrix and the luminescence band at peak position of ~ 780 nm is originated from these nanocrystals. Two important changes are observed as the annealing temperature is raised from 900 °C to 1050 °C. First one is that, defect peaks at ~570 and 650 nm disappear totally, and the second one is the red shift in the peak position accompanying sharp increase in the intensity and narrowing the PL band. On the other hand, in the peak position and the shape between PL spectra of the samples annealed for 2 h and 4 h at 1050 °C are same. The intensity of the emission in the sample annealed for 4 h is however more efficient in than the sample annealed for 2 h.

The enhancement in the intensity for long time annealing is probably due to the reduction in the number of P_b defects in the system, especially on the surface of NC. P_b centers are very stable at high temperatures [101], and it requires longer time to eliminate them even at such a high (1050 °C or more) temperature. From here, we can assume that, 2 h prolonged annealing enhances elimination of P_b defects three times in number, if increase in PL intensity of these two samples taken into account. The elimination of the defects most probably is done through mild oxidation of the samples via high temperature annealing under N_2 atmosphere. Also 4 h annealing can provide good crystallinity further, which can be also accounted in intensity increase. To test the

relative percentage of those effects, these two samples can be passivated by through forming gas at low temperatures ~ 450 °C.

Figure 5.1 demonstrates clearly that the very broad emission band with width of ~ 375 nm in range results from the Si NCs formed in the oxide matrix by means of ion implantation method. The broadness of the peak might be attributed to two phenomena: first one is the Gaussian distribution profile of implanted ions, which creates a nonuniformity in the size and distribution of the nanocrystals. Serincan et al, [103] supported the presence of this phenomenon by etching the oxide including Si NC in a systematic way. Other broadening mechanism is inevitably peculiar to Si NC and oxide matrix relationships. Except very small NC, the dominant recombination of excited excitons occurs at the surface or strained suboxide shell region through coupling with localized Si – O vibrations at the interface. Involvements of these vibrations result in further broadening in emission spectrum.

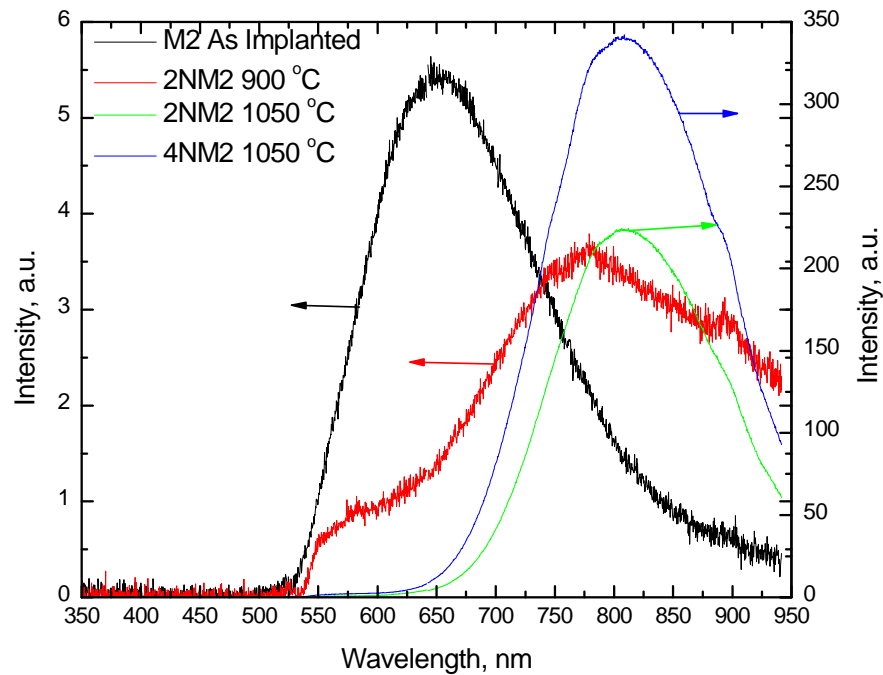


Figure 5.2. Room temperature PL results of the sample series M2 annealed at different temperatures and durations. Implantation energy is 40 keV and other parameters are same as series M3

Figure 5.2. Shows the PL results of the sample series M2 which have the same properties as the series M3 except for the implantation energy (Table 4.1). When Fig.5.2 compared with Fig.5.1, some differences in PL spectrums can be seen easily. First of all emission intensity from NBOHC decreased in the as-implanted sample of M2 compared to M3. This is due to either, higher implant energy in M3 that can break much more bonds in oxide, or higher density of implanted Si per unit volume of the oxide in M2. As the number of Si atoms increased per unit volume of oxide, the probability of interaction of Si and O increases, so the number of NBOHC would decrease. When the samples annealed at 900 °C are compared, we see a remarkable increase in PL intensity with the peak position at ~ 780 nm for M2 (peak position for M3 is at ~ 745 nm). In addition, there is ~ 45 nm red shift in the peak position. The reason for this is clear: when Si atom density increases, size and the density of the cluster will increase accordingly. Due to the quantum confinement effect, the exciton emission energy of larger clusters or NCs is lower than that of smaller structures, leading to light emission with larger wavelength for bigger clusters. Experimental results presented here exhibit a complete consistence with theory, excitons created in clusters of M2 series have lower emission energy (clusters of M2 series have lower band gap energy) than M 3 series.

Samples of M2 that annealed at 1050 °C for 2 h and 4 h show the same behavior as M3 series samples having the same annealing conditions. Peak positions stay at 810 nm for both 2h and 4h annealed samples (M2). When we compare this value with M3 series samples (1050 °C, 2 h and 4 h annealed) ~ 30 nm shift of peak position to the higher wavelength can be seen due to larger NC formation in M2. The increased PL intensity can be attributed to the higher NC density as a result of higher dose per unit volume. Because, in M3 series implant energy of Si 10 keV higher than M2, so part of implanted ions inserted in to substrate by decreasing density of Si in oxide. There seems a controversial situation when width of the spectra are compared, M2 series samples show broader luminescence band than M3. Considering the implantation energy, it is expected that luminescence band of M2 series would be narrower than M3. Moreover, as the size of NC increase, recombination through interaction with Si-O vibration increase accordingly. This interaction further increases the width of the spectrum to the low

energy side. Then one can say that, optical transitions via vibronic processes in Si NC would tend to increase in accordance with increase in size.

In Fig. 5.3 and Fig. 5.4, PL results obtained from series M1 and M4 are given. Both series have the same preparation conditions except for the implanted dose and the annealing temperature. The annealing temperature was 1100 °C for M4 whereas it was 1050 °C for M1. Both series have p-type Si substrate, and the implanted dose for M1 is five times lower than for M4. From the figures, it is seen that, for all the case, as implanted samples exhibit PL emission at approximately same peak position, but with different intensity. Therefore it can be concluded that, type of the substrate (whether n-type or p-type), dose and energy of implanted Si atoms do not affect the shape and peak position of the PL band seen in the as-implanted samples; only the intensities increase or decrease depending on the energy and the dose through which only the number of NBOHC is effected. In Fig 5.3 PL spectra of two M1 samples annealed at 1050 °C for 2 h are shown. The difference between two samples is the annealing condition: one of them is annealed under nitrogen atmosphere and the other one under vacuum at a level of $2-3 \times 10^{-5}$ Torr. When these two PL spectra of M1 are compared, we see a significant difference between them: sample annealed under vacuum have a weak PL peak at ~ 790 nm, while the sample annealed under N₂ atmosphere has a main peak, which can be attributed to the formation of NC, at ~ 765 nm, accompanying with very broad shoulder at the high-energy side. Two possible reasons might be mentioned for this observation: the shoulder seen in the high energy side can be attributed to either peroxy- radical defects via further oxidation during annealing (due to the trace amount of oxygen in the N₂ atmosphere) or very small nanocrystals because of low dose Si implantation. The lower PL intensity for the sample annealed under vacuum can be due to larger number of non-radiative defects than the sample that annealed under N₂; for the former one, very low level oxidation during annealing process would suppress non-radiative defects by saturating broken bonds at Si NC surface. It can be concluded that the annealing under high vacuum atmosphere prevent further oxidation of nanocrystals leading to the formation of larger nanocrystals. In addition, it was realized that from Fig 5.3, there is a red shift ~ 15 nm in the peak position as the annealing time increased to 4 h under N₂ atmosphere.

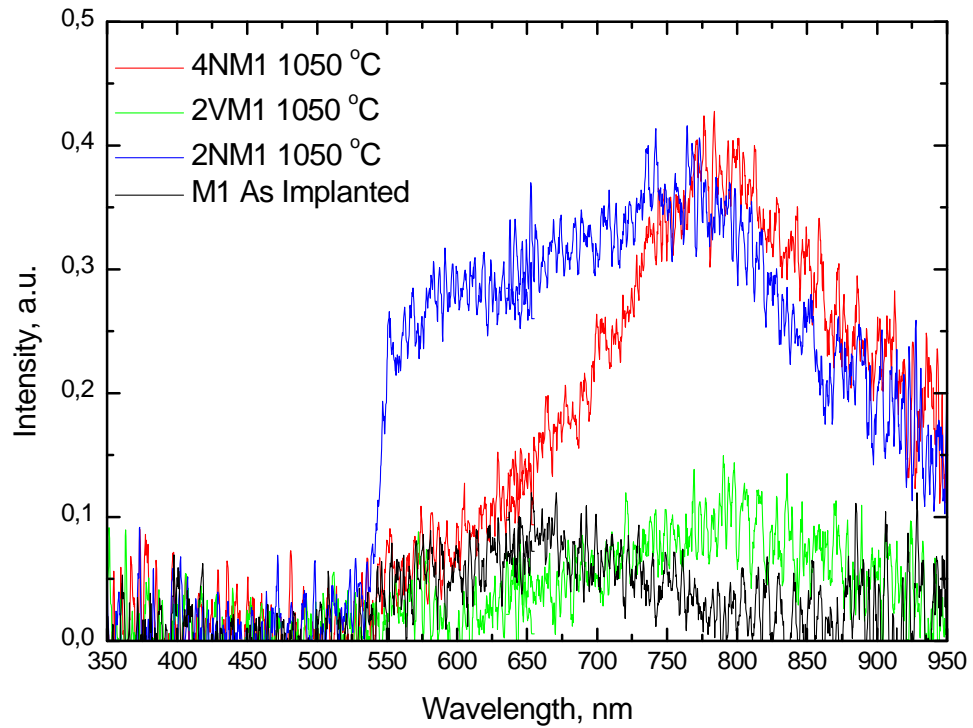


Figure 5.3. Room temperature PL observed from the series M1 (p-type Si substrate with 40 nm thermal oxide). Green spectrum from the sample annealed under vacuum, others are annealed under N_2 atmosphere. Dose of implanted Si is $1 \times 10^{16} \text{ cm}^{-2}$ with implantation energy of 15 keV.

From Fig.5.3 and Fig 5.4, when spectrums of samples annealed under N_2 atmosphere compared, there is a red shift in emission in M4 series with respect to M1, due to both higher Si content and higher annealing temperature, which induce larger NC in M4 accompanying with larger wavelength of emission. Fig. 5.4 shows $\sim 25 \text{ nm}$ blue shift in 4 h annealed sample with respect to 2 h annealed one. There are two possible explanation of this: first one is, further oxidation of NC surface that results in size reduction because of for 2 h prolonged temperature treatment. The other one is exciton migration effect which is expected for the case of M4 having high excess Si content. In 2 h annealed sample excitons created in small nanocrystals can migrate to larger one through possible tunneling events, then recombine there radiatively by emitting larger

wavelength photons. Therefore, as the number of photon emission at high-energy side bleached, PL spectrum shows red shift. When annealing time raised to 4 h, oxide matrix become more resistive to exciton tunneling between dots and created excitons recombine at their NC and total spectrum shows blue shift with increasing intensity of emission. Exciton migration or energy transport effect can be also seen other samples but it is much more effective in series M4 due to higher density of NC, which enhances tunneling between dots. However, both mechanisms can takes place at the same time; to analyze exciton transport effect in this situation; careful analysis has to be done over temperature dependent PL experiments.

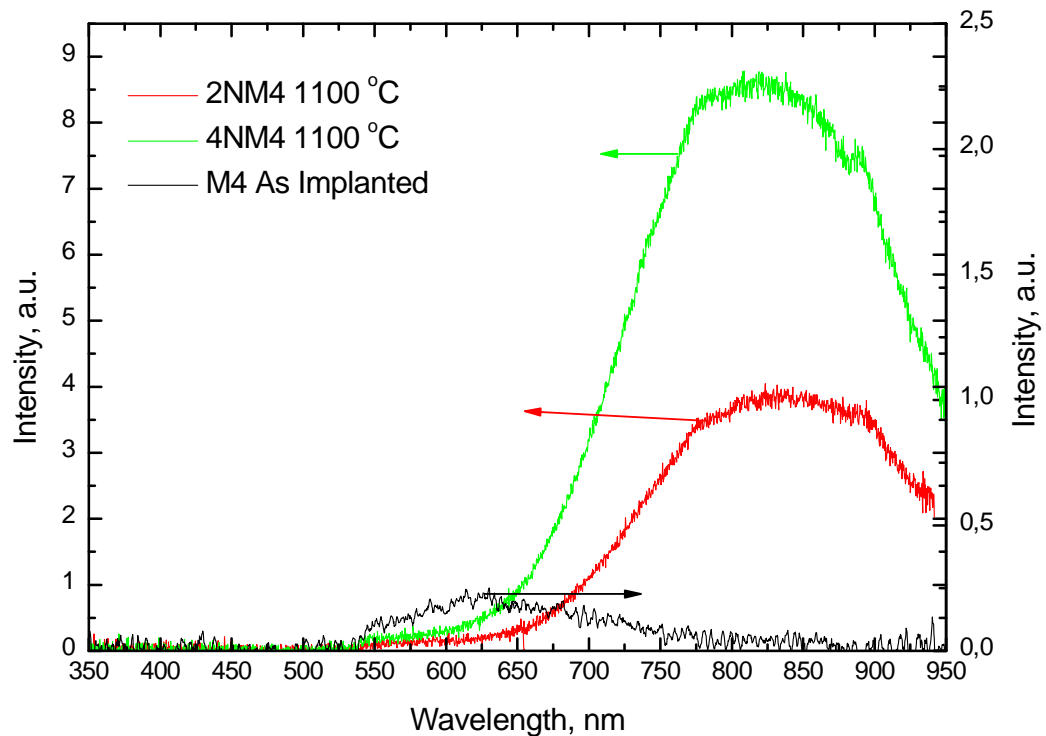


Figure 5.4. Room temperature PL spectrum from series M4. Implanted Si dose is $5 \times 10^{16} \text{ cm}^{-2}$, and all other parameters are same as M1. (PL spectra of sample annealed at $900 \text{ }^\circ\text{C}$ is absent)

5.2. Current-Voltage (I-V) Results

Understanding the carrier transport mechanisms is critical for engineering improved devices (memory, light emitting devices etc.) based on Si NC MOS structures. There are many transport mechanisms adapted to MOS structures without NC inclusions; some of them are given in Fig.3.9. Today, for the case of Si NC MOS structure, these mechanisms are applied directly as in the case of bare oxide MOS structures.

The most frequently used mechanisms in Si NC MOS structures are single step tunneling processes: the direct tunneling through trapezoidal barrier between anode and cathode and the Fowler-Nordheim (FN) tunneling through triangular barrier of oxide (also rarely two step tunneling process are considered; field assisted, trap assisted etc.). However, in the realistic case these adaptations cannot give accurate transport phenomena in Si NC systems synthesized in the oxide. The problematic sides of these mechanisms can be summarized as follows for Si NC oxide layer. First, FN tunneling is developed for the smooth barriers without any local field variation in oxide matrix. Second, classical FN transport treated the carrier tunneling between Si substrate and top contact directly. Third, both Direct and FN tunneling exclude size variation in Si NC and Coulomb blockade effect because of charge trapping in/on Si NC surface. Therefore, any resonant tunneling effects via quantized energy levels between neighboring Si NC and so on are also ignored. As expected, transport properties of Si NC become very complex when all these parameters are included.

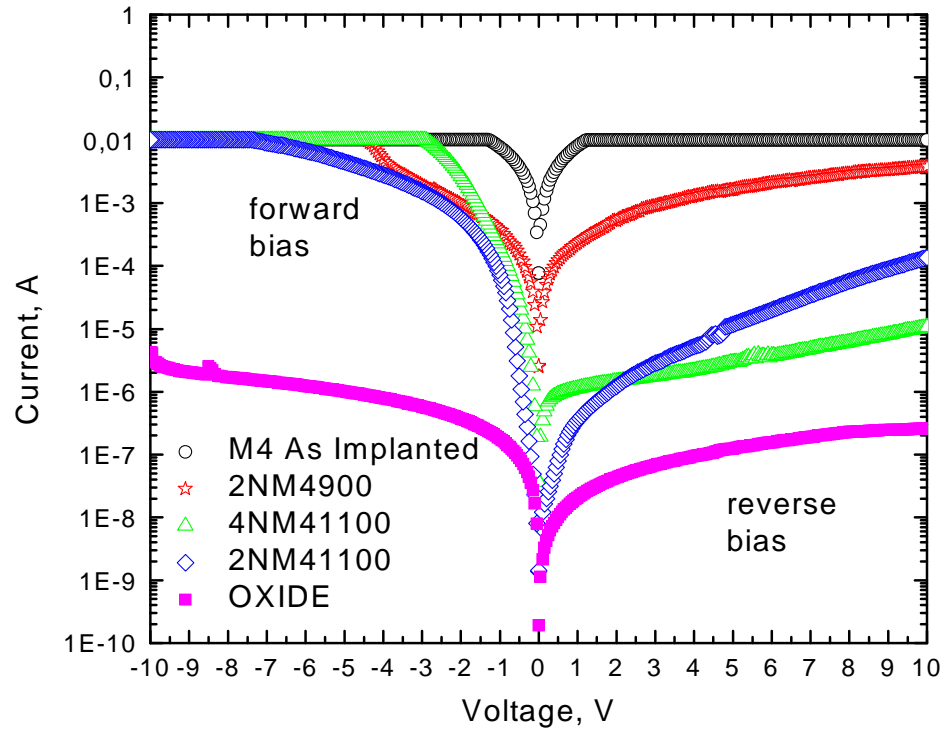


Figure 5.5. Observed I-V results from Series M4 for different annealing time and duration. Samples substrate is p-type, oxide thickness is 40 nm, implant energy 15 keV and dose is $5 \times 10^{16} \text{ cm}^{-2}$.

In Fig. 5.5 observed I-V results for the series M4 is given including the oxide under both forward and reverse bias conditions. Maximum current through devices was limited by the measuring set up to the 10 mA. As the substrate is p-type, in the forward bias case substrate voltage is positive with respect to top contact and opposite situation holds for the reverse bias. Therefore, in the forward bias, electrons are injected from ITO window and holes are injected from the Si substrate. In reverse bias case, injection of electrons occurs from inversion region (minority carriers, electrons, accumulated at the Si/SiO₂ interface under the SiO₂) of the p-type Si substrate. From the figure, it is seen that, there is a systematic change in I-V spectrum as a function of annealing temperature and time. Conductivity of Si NC oxide is largest for the as implanted sample, resistance of the layer increases following annealing treatment, accordingly. Observed change in the current through the oxide layer is more significant for reverse bias. The conduction

mechanism for as implanted sample could be percolation type conductance through resistive network created across the implanted oxide layer, in which the carriers follow the least resistive paths. Implantation process results in reduction in oxide band gap through excess Si, and the barrier for the charge injection will be reduced by either band gap narrowing of the oxide or enhanced via created traps at interfaces and in the oxide. At annealing temperature of 900 °C, both formation of small crystallites and reconstruction of destructed oxide matrix are expected to be initiated. Therefore, resistance of oxide increases resulting in small reduction of current. It is seen in Fig.5.5 that there is a jump in the current around voltage value of 4 V in the forward bias, which indicates change in the transport mechanism probably due to a new mechanism like the trap assisted tunneling to the direct tunneling. Actually, upon annealing at 1100 °C, as NCs form and increase in size through Oswald ripening process at the expense of dissolved Si atoms and small crystallites in the matrix, resistance of oxide increase further. This reduction in conductivity is because of increased tunneling barrier both at interface and between neighboring NCs. It is seen that, there is a distinct transport behavior between samples annealed for 2 and 4 h at 1100 °C, both at forward and reverse bias. Difference in the reverse bias case can be attributed to the Coulomb blockage effect due to the trapping of the electrons in Si NCs especially at or near substrate /SiO₂ interface, and can be concluded that, in 4 h case NCs are well passivated. Difference in forward bias case might also be related to the degree of passivation through which tunneling mechanisms change. Therefore, it is expected that direct tunneling is more dominant over trap assisted one and starts at low voltage values for 4 h annealing sample compared to two hours case. The field across the Si NC oxide layer was calculated to be $\sim 10^6$ V/cm under the assumption of all voltage drop occur on oxide layer and oxide treated as bare and perfect. This field level is approximately corresponding to the starting threshold of Fowler- Nordheim (F-N) tunneling via triangular barrier. Therefore, when Si NC and any voltage drop at substrate and contacts included, it can be concluded that, at this bias range, F-N tunneling does not occurs in these samples.

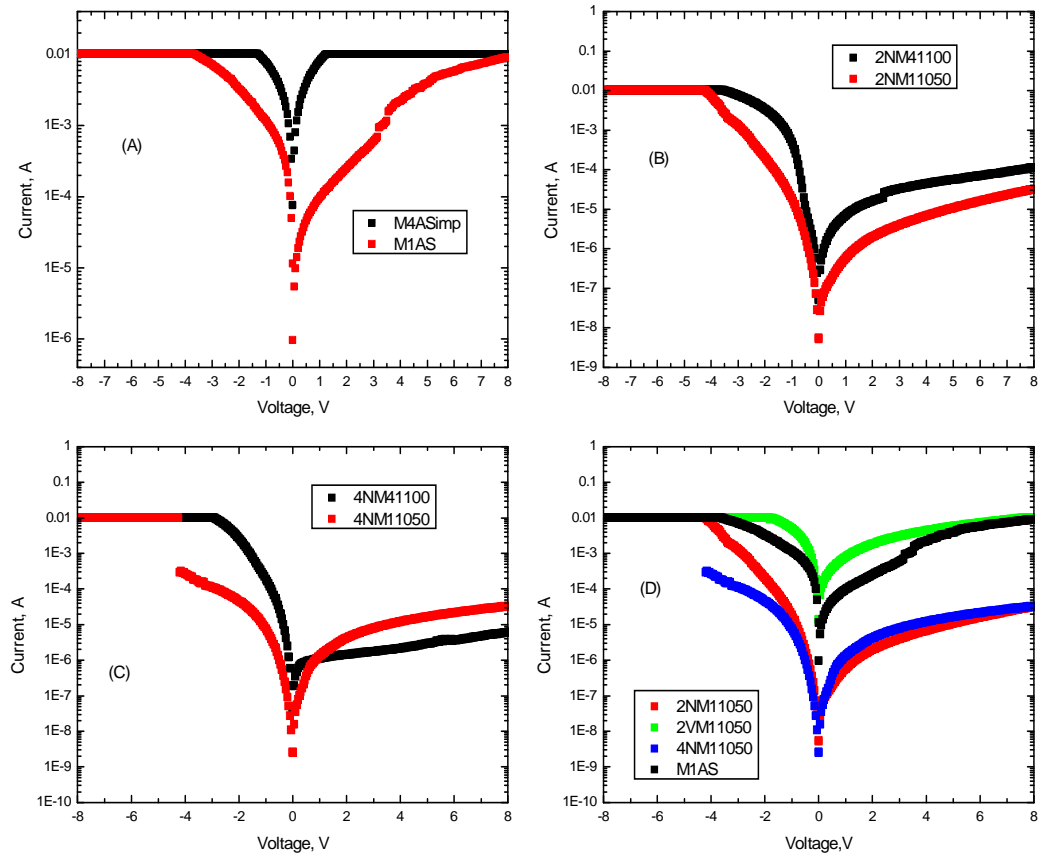


Figure 5.6. Comparison of I-V results of series M1 and M4. (A) As implanted samples, (B) 2 hours annealed at 1050 °C (M1) and at 1100 °C (M4), (C) 4 hours annealed samples, (D) I-V results of series M1. Substrate, oxide thickness and implant energy are same for both series.

Fig. 5.6. (D) Shows I-V results of Series M1. An important feature is observed for the sample annealed under vacuum that, current passing through vacuum annealed samples is higher than as implanted sample. Reason for this situation could not be understood. The other two samples annealed at 1050 °C shows the same tendency as in the case of M4. Other graphs of the Fig 5.6 represent the comparison between three samples of both series. Except reverse bias side of 4 h annealed samples, M4 shows higher conductivity than M1, although they were annealed at higher temperature. From these comparisons, it

is observed that, increase in excess Si atoms in oxide result in higher current level accordingly. NC density is proportional to excess Si the in oxide, therefore tunneling transport is enhanced. As mentioned for M4, F-N tunneling also seems impossible for M1 in this voltage range.

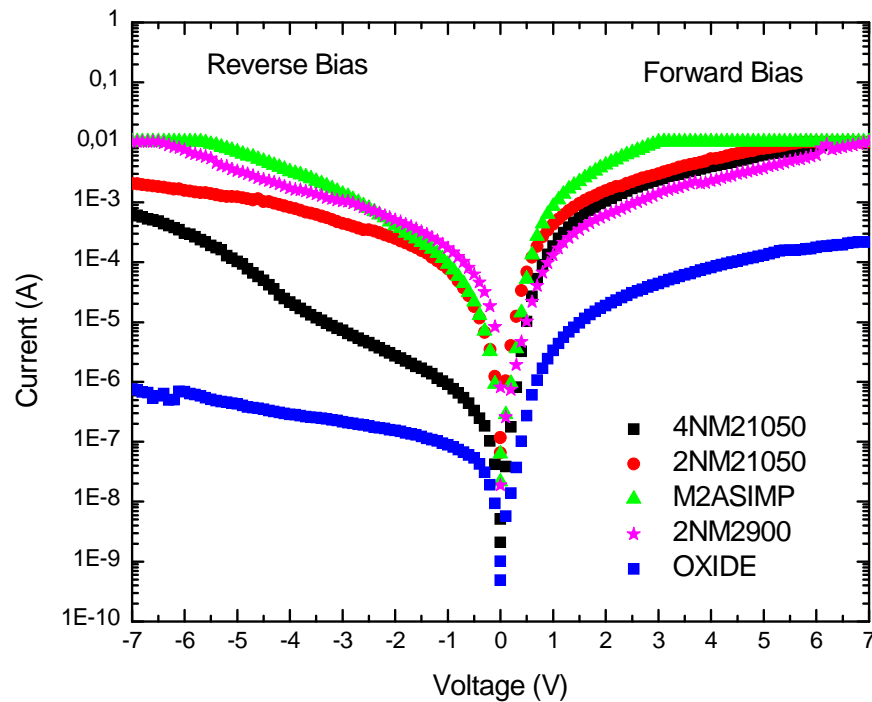


Figure 5.7. Observed I-V spectrum of series M1 at both forward and reverse bias range of 7 V. Substrate is n-type, oxide thickness 100 nm, implanted Si dose $5 \times 10^{16} \text{ cm}^{-2}$ with an implant energy of 40 keV.

I-V spectrum of series M2 is given in Fig. 5.7. For these samples substrate is n-type with an oxide thickness of 100 nm, so in forward bias case applied voltage to the top contact is positive with respect to the substrate, in the reverse bias case opposite is true. In forward bias electron injection occurs from substrate into Si NC oxide layer, in reverse bias electron injection from top contact to oxide and hole injection from inversion region of Si substrate into oxide occurs. Spectrum shows that, for samples of M2, changes in current level are lower with changing annealing temperature and time, compared to p-type samples M1 and M4, especially in reverse bias regime. Rectifying

property of p-type samples was enhanced for a given voltage range as the annealing time and temperature increase; for the case of M2 current level at both bias regime was found to be more symmetric and little rectification is pronounced for the samples annealed higher temperature and longer duration.

In both n and p-type substrate samples, dominant current mechanism is electron transport, because hole current gives small contribution due to the higher barrier at SiO₂/Si substrate interface for holes. Barrier height between oxide and Si for a hole is 4.6 eV, for the case of electron it is 3.2 eV. In addition, mobility of hole is much smaller in the oxide compared with electron mobility; mobility of an electron and a hole is 20 cm²/Vs, 4x10⁻⁹ cm²/Vs respectively. Although implanted samples in figures (both n and p-type) show enhanced current transport compared unimplanted oxide through decreased oxide barriers, there is a huge asymmetry between electron and hole injection into Si NC oxide, that is the main problem of this systems in the production of light emitting devices.

5.3. Electroluminescence (EL) Results

Contrary to PL spectroscopy in which suitable light source was used to create electron-hole pairs, in EL, current across Si NC oxide layer was used via applied voltage for the same purpose. Understanding the electron-hole pair excitation and recombination mechanisms are very crucial for making reliable and efficient electrically driven Si NC based EL devices. As mentioned in Chapter 3, due to difficulty in injection of carriers especially of holes, limits the efficiency in EL emissions compare to PL ones. Because of this reason, although large number of papers about Si NC systems appeared in the literature, only few of them are related with EL studies. One of the main obstacle for Si NC oxide structure, to suppress or minimize the difficulties mentioned above, is the lack of appropriate theoretical transport modeling in the nano-scale range to engineer efficient device design.

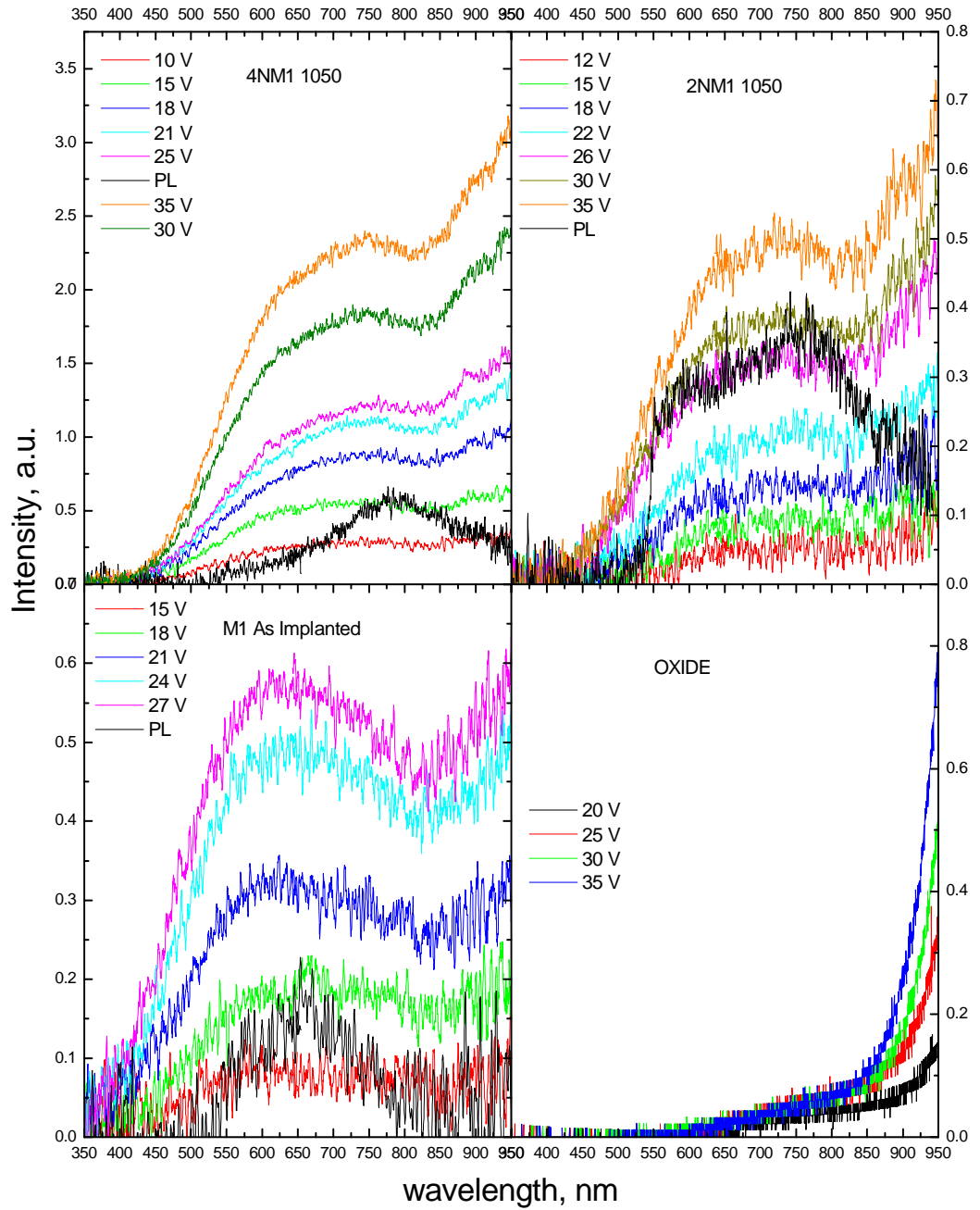


Figure 5.8. EL spectrum of series M1 and oxide as a function of applied voltage under forward bias. PL spectrum given for comparison and EL spectrum of oxide is given as a reference. Both side of y scale refers to intensity for each sample. Intensity of EL and PL are comparable.

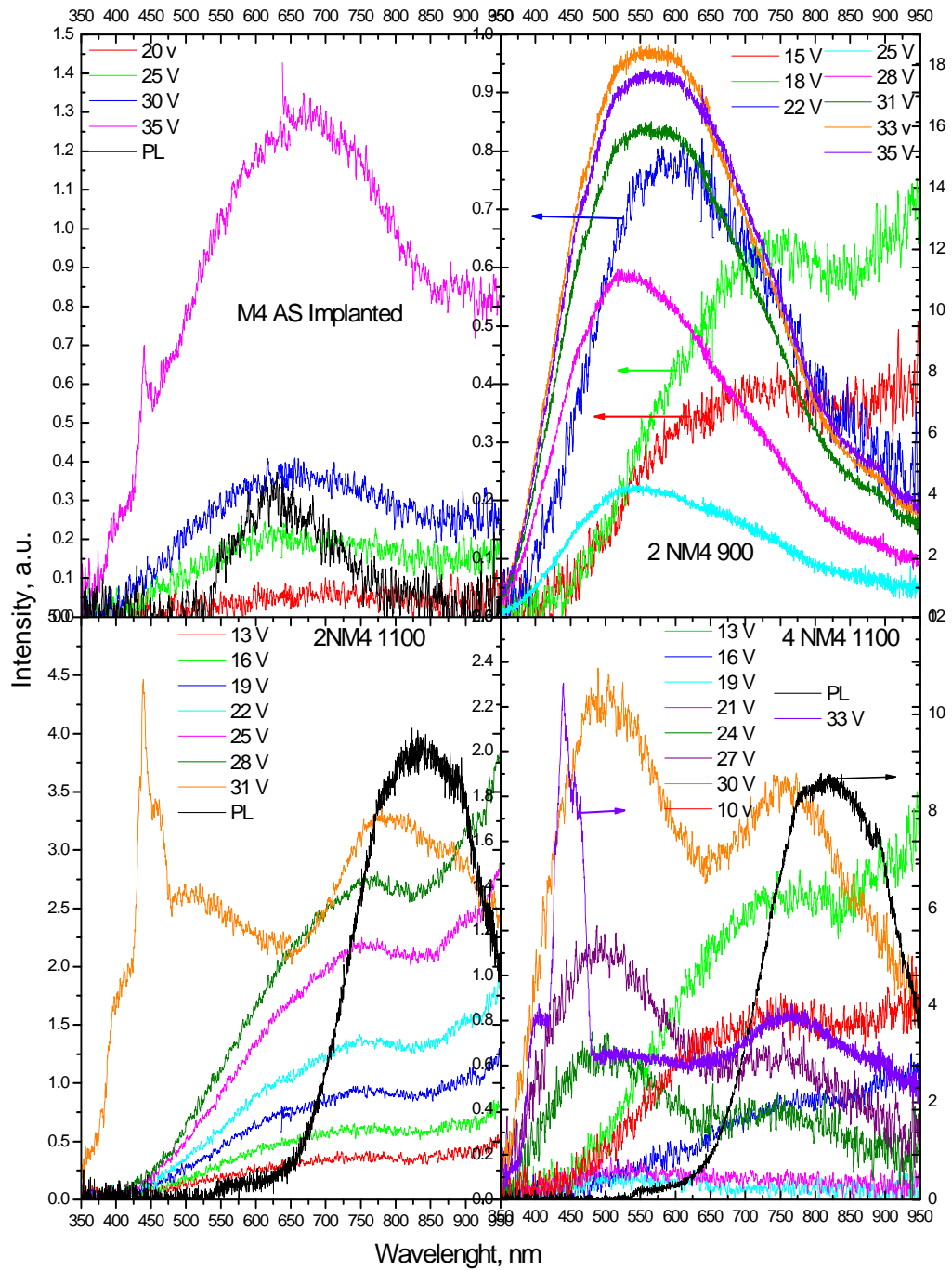


Figure 5.9 Observed EL results with varying applied voltage under forward bias for the series M4. Corresponding PL spectrums are given for comparison for each sample. Arrows indicate corresponding intensity scale.

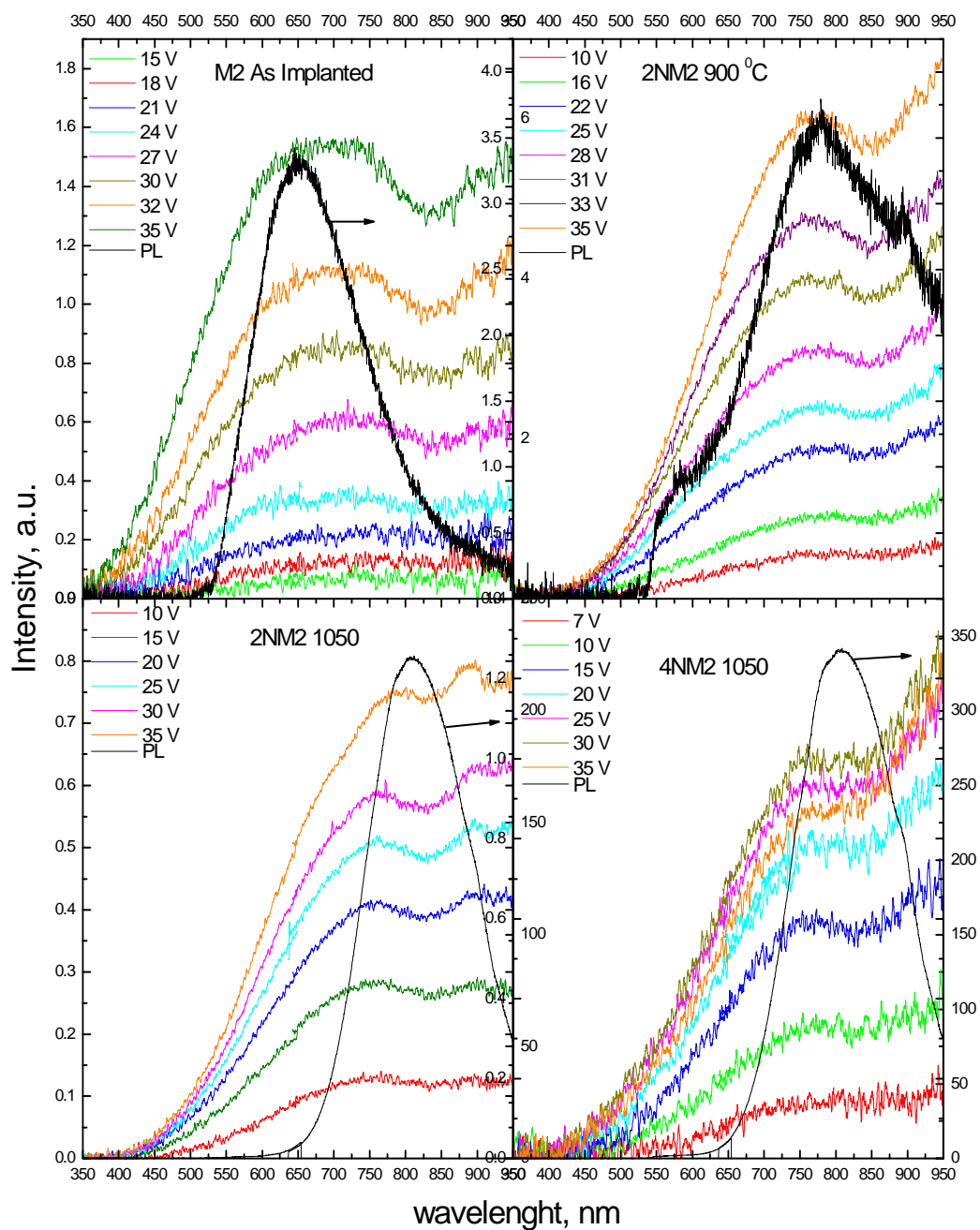


Figure 5.10. EL results taken from series M2 as a function of applied voltage under reverse bias. EL intensity increases with increase in applied voltage. For as implanted and 900 °C annealed samples EL and PL intensities are comparable. At higher temperature PL is much more intense than EL.

EL study was performed using around 80 device structures on 16 different substrates that have different parameters of implant dose, implant energy, substrate type, annealing temperature and duration. All EL measurements were done in a dark room by applying dc bias voltage in a range of between zero and 35 V with 47 ohms one watt load resistor. Due to, set up limitation, I-V characteristics of the samples above 10 V bias could not be observed. For the case of devices fabricated from M3 series with gold optical window and the devices from vacuum annealed sample of M1 series, no valuable data was observed. The main reason for this is that the gold window was not transparent enough for light extraction. Also some of devices from other series did not emit at any applied bias voltage, most probably due to presence of low resistive paths that current follow easily without passing through nanocrystals. Two of the device from M2 was tested for a time period of 90 minutes by applying constant voltage value of 18 V and there was no change in the measured EL spectrum. Moreover, it was seen that devices on the same substrate with the same processing parameters could exhibit small differences in the EL spectrum and in the detection threshold of the emission. This situation can be result of local variation in the oxide layer and ITO window as the devices have large area with higher probability for this kind of effects.

When compared EL results with spectra observed in PL measurements, there are some discrepancies that can be accounted for differences in the mechanisms of excitation and recombination mechanisms. EL spectrums are much broader than PL ones and relatively weak in intensity, accompanied by the Si substrate emission. Except one device of series of M2, EL emission was not observed for the cases when the holes didn't supplied by Si substrate.

EL spectrums of the series M1, M4 and M2 are given in the figures 5.8, 5.9 and 5.10 respectively. In all cases, it is easily seen that, at low energy side of the spectrums, tail of the Si emission is present. The intensity of this emission in some cases was much larger than the interested ones that attributed to Si NCs. However, Matsuda et al. [104] speculated that, this emission may result from Si nanocrystal , but there is no any author reported to support for this explanation. As it is shown in the figures, EL spectrums are

broader than corresponding PL results, it is getting wider with increase in applied voltage accordingly. For the p-type samples spectrums that were taken under forward bias, i.e. holes are supplied by substrate in accumulation condition under which holes are accumulated at the Si/oxide interface with positive voltage applied to back contact. In the case of n-type samples holes are supplied again by substrate under inversion condition, i.e. electrons are depleted from near interface region and holes are inserted there with positive back contact.

EL results of as implanted samples almost follow PL ones, but small blue (in M4) and red sifts (in M1 and M2) at the peak position can be recognized. There is ~ 200 nm broadening at high energy tails depending on voltage value. For the low energy tail, we can not say anything without de-convoluting the spectrum, since participation of substrate emission seems very significant up to 750 nm. Moreover, intensity of emission also increases beyond the PL case except M2, as the voltage increases. These (broadening and increase in intensity) can be either excitation of higher energy luminescent defect centers existing through implanted region, which couldn not be excited in PL case at high energy tail because of lower photon energy of exciting light, or creation of these defects through current flow or both of them. Either blue or red shift in the peak position can be related to the relative number of defect centers (NBOHC, B₂, E', etc.) determined by dose and energy of implanted excess Si.

For the devices from samples annealed at 900 °C, (for M4 there is no PL result to compare), significant changes was observed in EL spectra compared to as implanted ones. Width of the spectrum is narrowed by ~ 100 nm from the high energy side, indicating that, annealing eliminated or decreased concentration of defects which have the emission band at higher energy. EL spectrum of M2 series at 900 °C is given in Fig.4.10 and it is consistent with the PL spectrum peaked at 775 nm. Peak position at 10 V is around 760 nm, increased to ~ 770 nm with 16 V and pinned for all bias voltage. As mentioned before PL emission was attributed for small nanocrystallites in amorphous phase, having similarity with PL, we can assume that both EL and PL originated from same source. Big changes were observed in the case of M4. Upto 22 V peak position showed red shifts from 725 to 740 nm and intensity increased; with bias voltage of 22 V peak shifted to 595 nm. Further, increase in voltage first resulted in blue shift to 535 nm

then red shift to 570 nm and stabilized there. It is seen from Fig 5.9, the width of the spectrum follows increase in the applied voltage, and relative intensity of lower energy side tail decreases as the peak start to shifts to high energy side. The main reason of this emission might be larger content of Si in the oxide. As the Si content increases defect related yellow blue emission increases, contrary to the previous observations [105]. This situation can be seen in PL results as a blue shift in the as implanted samples peak positions. During the Si implantation and following annealing steps, oxygen deficient centers and E' centers are formed. It is suggested that hole trapped at Si – Si bond of oxygen deficient centers broken and are transferred to E' centers [106]. Therefore, as the bias voltage increases tunneling of holes from the substrates to these centers increased, then at the expense of luminescence around 740 nm, the yellow emission increases much larger. At moderate bias voltage this process is thought to be the precursor breakdown initiation of the device. It is also seen within the same figure (Fig. 5.9) that intensity of the emission decreases from 33 V to 35 V, which can be result of leakage current path formation that would either saturate or decrease the emission intensity. Also formation or increase in number of non radiative defects by hot carrier can be considered.

For the samples of M2 annealed at 1050 °C for 2 and 4 h, it is seen from Fig 5.10 that almost linear increase in the intensity and emission wavelength that's are more pertinent for the case of 2 h annealed sample. For this sample the peak position is at ~ 750 nm at voltage value of 10 V and systematically increases and reaches the value of ~ 790 nm at 35 V. The peak centered at 900 nm is a property of our measuring system not related with sample. For the sample annealed for 4 h peak position increases slowly and reaches ~ 770 nm at 35 V which is at ~ 760 nm at lower voltage values. PL peak of these samples centered at ~ 810 nm, blue shifts observed at highest applied voltage which are the smallest shift if other voltage values are considered, shifts values are 20 nm and 40 nm for 2 h and 4 h compared to PL spectrum.

For the case of samples of M1 series annealed for 2 h and 4 h, same tendency was observed as in the case of samples of M2 series. About 45 nm a blue shift is seen in 4 h annealed sample at the highest voltage of 35 V and in 2 h annealed samples shows it is about 30 nm at same voltage value, with respect to PL results.

Samples of M4 series, especially 4 h annealed one showed different behaviors. Two hours annealed sample had almost the same tendency for both of M1 and M2 up to 31 V, the peak at the low energy side is ~ 45 nm is centered at high energy side of PL peak. Two new bands are likely to be related with E' and B2 defect centers, indicating trace amount dissolved Si atoms in the oxide matrix. In the case of 4 h annealed sample, this behavior starts at lower threshold voltage as shown in Fig 5.9. As seen in this figure, the substrate emission is suppressed or decreased in relative intensity, when this defect related emission is triggered.

As mentioned before, there are two suggested excitation mechanisms in the literature, first one accounts for the recombination of electrons and holes under direct tunneling transport from the substrate and top contact in to the nanocrystals. The second mechanism depends on excitation of NC by impact ionization under high field mostly through F-N tunneling. However impact ionization mechanism is accepted for most of the researches working on EL emission.

Contrary to literature, we observed strong EL emission related to Si substrate at low energy side of the spectrum in both n and p-type samples. It was assumed here that this emission originated as tunneling of electrons from the top contact acrossing the Si NC oxide layer in to Si substrate. These electrons recombine with holes beneath the oxide layer present at the interface either under accumulation or inversion condition depending on the type of the substrate, and any quantum confinement effect especially under inversion condition modify this emission toward high energy tail of bare substrate emission. It is qualitatively concluded in the previous section that the main transport is the electron transport; therefore if some of the electrons are trapped or recombine through oxide, but most of them reach substrate. Most of these recombination should be non-radiatively as the substrate is indirect gap material, only small percentage would recombine radiatively. Therefore it can be suggested that, this situation may be the one of the reasons, which decrease the efficiency of Si NC EL in MOS structure, by reducing the hole number which may tunnel in to the oxide. Although we assumed this mechanism, other mechanisms suggested by Matsuda et al. [104] that relate this emission to Si NC, or any defect related emission could not be totally excluded.

As shown in figures and explained above, peak of the EL spectrum stays at higher energy compared to PL one. There is an important point is that, as the bias voltage increase EL peak shifts towards the PL peak position. This shift is more recognizable in samples annealed for 2 h with respect to 4 h annealed case. The possible reason is discussed below. The other important point is that, with increased voltage the high energy tail of EL spectra shifts towards higher energy further, possibly emissions from radiative defect centers, and this result is consistent with literature.

Although impact ionization may take part in EL emissions at high voltages, observed results indicate that, the most probable mechanisms are cold carrier tunneling either direct or trap assisted. It is also proved by the cases when hole injection did not occur from the substrate, no EL emission observed, except one device at bias of 35 V. If impact ionization was possible mechanism, devices should have emitted at both bias polarities.

When the voltage increased with suitable bias, holes from substrate tunnel in to the nearby Si NC when they meet the electrons supplied by top contact they recombine and emit light. As the excess Si has Gauss distribution in the oxide, relatively small size NCs are expected at the tails of distribution i.e. at the edges of the oxide layer. Therefore at low voltage the expected emission could have high energy photon. As the voltage increased the number of holes that populate the larger NCs would increase and the EL emission peak is dominated by longer wavelength photon. (the important point is here that the mobility of hole is so much small in the oxide that with increasing bias voltage they can tunnel in to the deep of the oxide, but most of the holes populate the NC close to the substrate depending on bias voltage). When 2 h and 4 h annealed samples of M2 series are considered which have the almost same PL peak, this point becomes clearer. When the annealing duration increases, oxide matrix becomes more resistive to tunnel especially for holes, and NC becomes more isolated from each other. So tunneling of holes or exciton toward larger NC from the substrate side become more difficult. It is seen that due to this effect a shift about 25 nm is observed between 2 h and 4 h samples at the voltage value of 35 V, the peak position of 4 h sample stays 25 nm at higher energy with respect to 2 h case. There is another important observation to prove this suggestion in Fig. 5.10, as the bias voltage increases EL intensity of the 4 h annealed

sample goes to saturation compared with 2 h sample. This can be result of either exciton crowding in the NC which enhances the Auger recombination or any leakage current path at high voltages, then EL intensity get to saturate or decreases

Those observations in this study strongly reject the impact ionization based emission mechanism in our devices. In impact ionization, the excitation of NCs, first start with the largest NC whose band gap is the smallest, as the voltage increases the energy of hot carries also increase. Therefore they can excite the smaller NC at high voltage values, exhibiting blue shift in the peak position of EL spectrum.

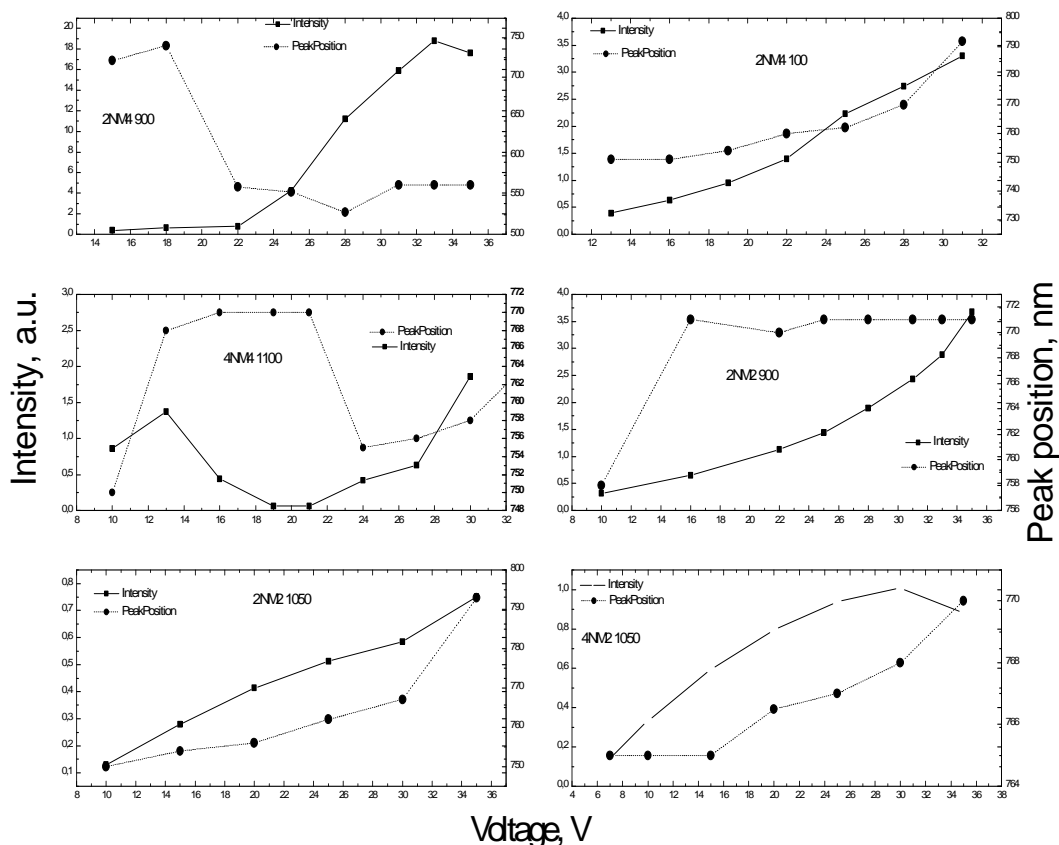


Figure 5. 11. Change of peak position and intensity of EL emission for varying voltage for annealed samples of M4 and M2. Red curves represent the peak position belong to right side and black ones represent intensity belong to left side of the graphs.

Fig. 5.11. Shows voltage dependency of EL intensity and peak position for annealed samples of M2 and M4. As clearly seen peak positions stays constant for samples annealed at 900 °C and might be indicative of almost same size nanoclusters. For the samples of series M2 at higher voltage values, there is a remarkable change in behavior of intensity is seen as NC becomes well isolated from 900 °C to 1050 °C with increasing annealing duration; intensity shows some power dependency on voltage and tends lowering power of function with increasing isolation. However, for the case of M4 series, no clear voltage dependence of intensity on applied voltage is seen.

CHAPTER 6

CONCLUSION

Quantum dots are nm size structures in which motion of electrons/holes is totally confined leading to quantization of energy. This quantization brings some physical properties which have not seen in bulk materials: by changing the size and the shape of this structure one can easily engineer optical and electronic properties of materials via quantum confinement effect. Due to their discrete density of states, production of very narrow line and temperature immune light emitting devices with very high efficiency is feasible.

Silicon is the primary material of today's microelectronic industry due to its superior properties compared with other group four and compound semiconductors. Although transport properties of Si stay at poor level with respect to compound semiconductors, it has advantage of high quality stable oxide and high crystal quality in the form of big wafers, which allow complementary very large scale integration on Si. Today Si technology forces its limits. It is believed that in near future it cannot supply the requirements of increasing demands in high speed and complex functionality of information area. There are some approaches to overcome difficulties in Si systems; however, replacement of metallic lines with optical ones is the most appealing solution. The difficulty of this solution is necessity of light emitting and detecting devices in the same chip with very clean junctions to Si.

Being indirect gap material, Si is useless in light emitting device applications; therefore bulk structure of Si cannot be used in chip level optical data transmission or any emitting device applications. However Si nanocrystals, especially embedded in SiO₂ has opened the opportunity of Si micro photonics, because nanocrystalline structures suppress momentum conservation requirement in emission and absorption of light through quantum confinement and leading to efficient light emission from these structures. There are several methods used for producing Si nanocrystal in oxide matrix, among them ion implantation is most versatile technique to engineer size, depth and

distribution of nanocrystals in the oxide, and it is very suitable for mass production in microelectronic industry.

In this study, Si ions were implanted into thermally grown SiO₂ films on both p and n-type Si wafer at various doses and energies in order to form Si nanocrystals in oxide matrix. Implanted samples were annealed at different temperatures and duration under N₂ atmosphere. LED structures were then fabricated using annealed samples. ITO optic window was used for both extract light and spread current over window area, ITO is transparent between 400 nm and 1100 nm with an efficiency of 90 %. PL measurement performed prior to device fabrication, I-V and EL measurements were done on the same devices. As explained in Chapter 5, it was observed that both optical and electrical properties showed differences depending on implanted ion dose, ion energy, annealing temperature and duration.

From PL measurement we observed that emission peaked at ~ 570 nm is from virgin oxide. This emission is not well addressed in literature, however we attributed this emission to the peroxy linkages/bridges known as oxygen excess luminescent center, probably result of non homogeneous oxidation of Si.

For all as-implanted samples, there is a very broad PL emission with maxima positioned at ~ 650 nm formed as a result of ion implantation process. This emission is well studied in Si NC/oxide systems and attributed to non-bridging oxygen hole centers (NBOHC). Depending on dose and energy of implantation this emission can exhibit small changes in peak position and intensity. As the implantation process also introduces nonradiative defects, NBOHC emission generally stays at weak intensity.

When samples (M2 and M3) annealed at a temperature of 900 °C, PL spectrums showed two important changes compared to as-implanted samples. A new emission band was observed peaking around at 750 nm, it can be due to formation of small Si nanoclusters. If the implanted dose is very high, small crystallites can form in the as implanted samples. Another identified change is a decrease in the intensity of NBOHC emission. Decreasing intensity of NBOHC may indicate formation of nanoclusters via reduced excess Si atoms in oxide matrix. Inefficient PL emission of nanoclusters can be both due to formation of Pb defects around them and crystalline structure of these clusters. There is a red shif of ~ 40 nm observed in emission around 750 nm for samples

having higher density of excess Si which induce larger nanoclusters, this redshift is consistent with quantum confinement effect.

For samples annealed at 1050 °C for 2 h and 4h, it was observed that the peak positions red shifted with respect to 900 °C annealed samples, and also sharp increase in intensity is pronounced with well shaped PL spectrum. At this temperature, NCs are expected to have good crystalline phase and the number of nonradiative defects on surface region of NC especially Pb centers decreases. Samples having more excess Si and annealed at 1050 °C showed red sifted PL peak position about 30 nm (from 780 nm to 810 nm) compared to those having less excess Si due to larger NC in former one. Except increase in intensity there is no red shift observed from duration 2 h to 4 h, there may be two reasons for this situation; first, Ostwald ripening process can be very difficult due to possible high diffusion barrier for Si atoms between nanocrystals. Second, any further oxidation process can prevent formation of larger nanocrystals. This oxidation effect can be supported by vacuum and N₂ annealed samples for 2h of M1 series, PL maxima of vacuum annealed sample shows ~ 25 nm red shift with respect to sample annealed under N₂. High vacuum atmosphere prevent oxidation of sample and relatively larger NCs can be formed. Furthermore more intense PL emission from N₂ annealed sample indicates the reduction of nonradiative defects through saturation by oxygen. Therefore, shoulder at high energy side (Fig. 5.3) of this sample may result from very small NC structures near the surface and reduced in size by oxidation of NC Si core. When we look at 4 h annealed sample this point becomes clearer: longer annealing duration results in consumption of NC at tail side of Gaussian distribution near the surface region.

Results of I-V measurements exhibited dependence of current passing through device on implantation and annealing parameters. Three different classes of MOS with NC structures have been analyzed. It is clearly seen in I-V curves that, current in implanted oxides are much larger than virgin oxide. We have observed that, as the implantation dose increases, current also increases at a constant voltage. When individual sample series are considered, largest amount of current is seen in as-implanted samples compared to annealed ones. This is because implantation introduce trap states are distributed everywhere in the oxides and these states lower the oxide barrier significantly and allow charge transport through oxide easily. There is a general

tendency which is clearly seen from I-V figures: increasing annealing temperature and annealing duration cause a reduction in the current. Annealing reduces number of available states involved in transport, as NCs are formed and the number of excess Si atoms reduced, oxide barrier increase between NC and available states in oxide matrix. Using the I-V curves we have qualitatively concluded that, Fowler-Nordheim tunneling is not possible in our devices because of large currents at low voltages. We could not identified current mechanisms, however it is expected that both single step and two step tunneling processes may involved.

EL results revealed significant differences between PL and EL spectrums due to different excitation mechanisms. When compared with PL emission, EL emission exhibited much broader spectrum and increasing bias voltage broaden the spectrum further. Two possible reasons for this result are luminescent centers at the high energy side; which can not be excited by the used light source and the other one is at low energy side, which is attributed to emission of Si substrate. For all samples, EL intensity increases with increasing bias voltage. For as implanted and 900 °C annealed samples, both EL and PL emissions peaked at almost same position indicating both emissions are from the same origin. For other samples, EL emissions maxima stayed at high energy side of PL emissions. When voltage increased, peak position shifts toward PL peak. However, in the case of M4, EL peak first approaches PL peak up to some voltage level, and further increase of voltage cause shift to green emission due to higher Si inclusion in the oxide, which promote luminescent defect E' emitting in green band. As a final remark, we have seen that EL emission is weak due to asymmetric charge injection in to the NC oxide. EL emission is observed only for biases for which hole is supplied by the substrate. As an excitation mechanism tunneling of carriers seemed to be very suitable for our devices, any effect of excitation through impact ionization was not identified. Both mechanisms can work at the same time at high voltage level, but tunneling seems much more dominant than impact ionization.

REFERENCES

- [1] V. V. Mitin, V. A. Kochelap, M. A. Strosio, *Quantum Heterostructures Microelectronics and Opto electronics*, Cambridge University press, 1999
- [2] S.V. Gaponenko, *Optical Properties of Semiconductor Nanocrystals*, Cambridge University press, 1998
- [3] L. Jacak, P. Hawrylak, A. Wojs, *Quantum Dots*, Springer, 1998
- [4] M. A. Reed, R.T. Bate, H. F. Kuhfuss, T. Shinn, J. Vacuum Sci. Technol. B, 4, 358 (1986)
- [5] P. Harrison, *Quantum Wells, Wires and Dots*, John Wiley and Sons (1999)
- [6] U. Serincan, Phd. Thesis, METU, June (2004)
- [7] M. Grundman (Ed.), *Nano-Optoelectronics Concepts, Physics and Devices*, 2002
- [8] A. D. Yoffe, *Advances in Physics*, 1993, Vol. 42, No. 2, 173-266
- [9] L. T. Canham, *Appl. Phys. Lett*, 57, 1046 – 8, 1990
- [10] Y. Kanemetsu, K. Shiraishi, T. Ogawa and K. Takeda, *Phys. Rev. B*, 48, 7 (1993)
- [11] M. Fujivara, T. Matsumoto, H. Kobayashi, K. Tanaka, N. Happo and K. Horii, *J. Lumin.* 12, 5-11 (2004)

- [12] J.Linnros, N. Lalic, A. Galeckas and V. Grivickas, J. Appl. Phys., 86, 11 (1999)
- [13] L. D. Negro, M. Cazzanelli, B. Danese and L. Pavesi, Physica E., 16, 297 (2003)
- [14] M. Cazzanelli, B. Danese, C. Spinella, S. Boninelli, J. Appl. Phys., 96, 10 (2004)
- [15] L. Khriachtchev, S. Novikov, J. Lantinen, J. Appl. Phys. 92, 5856 (2002)
- [16] M. Rasenen, S. Novokov et al., Appl. Phys. Lett. 79, 1249 (2001)
- [17] M. Nayfeh, S. Rao, N. Barry, J. Therrien, G. Belomin, A. Smith, Appl. Phys. Lett. 80, 121 (2002)
- [18] L. Pavesi, *Towards the First Silicon Laser*, NATO series 11, ed. By S.Gapenko, L. Pavesi and L. D. Negro, Kluwer Academic, 2003
- [19] M. Cazanelli, J. Heitmann, D. N. Urrios, F. Riboli, N. Daldasso, L. Pavesi, J. Heitman et al., J. Appl. Phys. 96, 6 (2004)
- [20] L.W. Hobbs, X. Yuan (Writ.), G. Pacchioni (Eds.), *Defects in SiO₂ and Related Dielectrics: Science and Technology*, Kluwer Academic Publishers, 2000
- [21] L. W. Hobbs, J. Non-Cryst. Solids, 192/193, 79-91
- [22] T. Bakos, Defets in Amorphous SiO₂, Phd. Thesis Work, 2003
- [23] S.T. Pantelides, Phys. Rev. Lett., 57, 2979 (1986)
- [24] A. N. Trukhin, J. Heithman, R. Scholz, E. Sonders, J. Non-Cryst. Solids, 331 (2003), 91-99

- [25] L. Skuja, *J. Non-Cryst. Sol.*, 239 (1998), 16
- [26] C. Barthou, P. H. Duong, A. Oliver, T. Itoh, P. Lavallard et al., *J. Appl. Phys.* 83, 12 (2003)
- [27] P. M. Lenehan, P.V. Dressendorfer, *Appl. Phys. Lett.* 44, 96 (1984)
- [28] A. Anedda, M. Cannas, R. Carpino, *Nucl. Instr. Meth. Phys. Res. B*, 116, 360 (1996)
- [29] S. Munekini, R. Tohmon, *J. Appl. Phys.* 68, 1212 (1990)
- [30] I. M. Lifshitz, V. Slyozov, *J. Phys. Chem. Solids*, 19, 35 (1961)
- [31] C. Wagner, *Z. Electrochem* 65 (1961), 35
- [32] V. R. Yazdanpanah, Physics Department, University of Arkansas
- [33] G. Rosenfeld, K. Morgenstern, M. Esser, G. Gomsa, *J. Appl. Phys. A* 69, 489 (1999)
- [34] P. W. Voorhees, M. E. Glicksman, *Acta Metall.* 32 (11), (1984) 2001
- [35] T. Kupper, N.Masbaum, *Acta Metall.*42 (6), 1847 (1994).
- [36] T. Pohl, C. Hammerl, B. Rauschenbach and U. Rude, *Nucl. Inst. and Meth. in Phys.Resarch B*, 158 (2001) 135-137.
- [37] G. Madras, B. J. Mcjoy, *Chem. Eng. Sci.*, 57, 3809-3818 (2002)
- [38] L. Ratke, C. Beckermann, *Acta Mater.* 49, 4041-4054 (2001)

- [39] G. Martin, *Solid State Phase Transformations in Metals and Alloys*, Les editions de physique, 1978
- [40] E. F. Brener, H. M. Krumbhaar, R. Spatschek, *Phys. Rev. Lett.*, 86, 7 (2000).
- [41] R. D. Vengrenovitch, *Acta Metall.*, 30, 1453-1440 (1982).
- [42] F.S. Lamarias, *Scripta Metall.*, 30, 1079-1086 (1993)
- [43] O. Hunderi, N. Ryum, *Acta Metall*, 29, 1737-1745 (1982)
- [44] G. Rosenfeld, K. Morgentern, *Surface Science*, 402-404, 401-408 (1998).
- [45] A. F. Leier, L. N. Safranov, G. A. Kachurin, *Semiconductors*, 33, 4 (1999)
- [46] T. Muller, K. H. Heinig, W. Moller, *Condens. Matter*, 1 (2002)
- [47] L. A. Nesbit, *Appl. Phys. Lett.* 46, 38 (1985)
- [48] M. Agarwal, S.T. Dunham, *J. Appl. Phys.* 78 (1995)
- [49] P. Mutti, G. Ghislotti, S. Bertoni, L. Bonoldi, K. Nagasava, *Appl. Phys. Lett.* 66, 851 (1995)
- [50] G. A. Kachurin, K. S. Zhuravlev, H. Tang, *Nucl. Instr. Meth. Phys. Res. B* 127/128, 583 (1997)
- [51] G. A. Kachurin, I. E Tyschenko, K. S. Zhuraulev, N. A. Pozdnikov, V. A. Volodin et al., *Nucl. Instr. Meth. Phys. Res. B* 112, 571 (1997)

- [52] U. Serincan, S. Yerci, M. Kulakçı and R. Turan, Nucl. Instrum. Methods Phys. Res. B, inpress
- [53] Y. Sakurai, K. Nagasawa, J. Appl. Phys. 88, 168 (2000)
- [54] H. Heckler, D. Kovalev, G. Polliski, F. Koch, Phys. Stat. Sol. (b) 215, 871 (1999)
- [55] V. A. Kharcenenko, M. Rosen, J. Lumin., 70, 158 (1996)
- [56] Y. Kanemitsu, S. Okamoto, Phys. Rev. B 58, 5692 (1998)
- [57] Y. Kanemitsu, T. Ogava, Phys. Rev. B, 48, 4883 (1993)
- [58] M. S. Hybertsen, Phys. Rev. Lett. 72, 1514 (1995)
- [59] C. Garcia, B. Garrido, P. Pellegrino, R. Ferre, J. A. Moreno, J.R. morante, Physica E 16, 429-433 (2003)
- [60] R. J. Needs, K. J. Nash, A. Qteish, A. J. Read, L. T. Canham, Phys. Rev. B 50, 14223 (1994)
- [61] D. Kovalev, H. Heckler, M. B. Chorin, G. Polisski, M. Schwatzkopff, F. koch, Phys. Rev. Lett. 81, 13 (1998)
- [62] T.Y. Kim, C. J. Choi, N. M. Park, K. H. Kim, G. Y. Sung, Y. W. Ok and T. Y. Seong, Appl. Phys. Lett. 85, 22 (2004)
- [63] P. Photopoulos, A. G. Nassipoulou, J. Phys: Condens. Mat. 15, 3461-3650 (2003)
- [64] T. Gao, S. Tong, X. Wu, X. Bao, G. G. Sui, Phys. Lett. A 253, 234 (1999)

- [65] J. Ternon, F. gourbilleau, C. Dufour, J. L. Doualan and B. Garrido, *J. Lumin.* 99, 361-364 (2002)
- [66] X. L. Wu, T. Gao, G. G. Siu, S. Tong and X. M. Bao, *Appl. Phys. Lett.* 74, 2420 (1999)
- [67] M.L. Brongersma, A. Polman, P. G. Kik, K. S. Min and H. A. Atwater, *Appl. Phys. Lett.* 76, 351 (2000)
- [68] G. Ledoux, J. Gong, F. Huisken, *Appl. Phys. Lett.*, 79, 4028 (2001)
- [69] D. S. English, L. E. Pell, Y. Zunghuva, F. B. Paul, B. A. Gorkel, *Nanoletters* 2, 681 (2002)
- [70] J. Martin F. Cichos, C. von Borczyskowski, *J. Lumin.* 108, 347-350 (2004)
- [71] S. Ossicini, R. Magri, N. Daldosso, M. Luppi, *Phys. Rev. B* 68, 085327 (2003)
- [72] L. Pavesi, *J. Appl. Phys.* 80, 1 (1996)
- [73] J. Heitmann, F. Muller, L. Yi, M. Zacharias, D. Kovalev and F. Eichhorn, *Phys. Rev. B* 69, 195309 (2004)
- [74] H. E. Roman and L. Pavesi, *Condens. Matter* 8, 5161 (1996)
- [75] I. Mihalcescu, J. C. Vial and R. Romenstain, *Phys. Rev. Lett.* 80, 15 (1998)
- [76] A. L. Efros, M. Rosen, M. Kuno, M. Nirmal, D. J. Norris and M. Bawendi, *Phys. Rev. B* 54, 4843 (1996)
- [77] E. Martin, C. Delerue, G. Allan and M. Lannoo, *Phys. Rev. B* 50, 24 (1994)

- [78] F. A. Reboredo, A. Francescetti and A. Zunger. *Appl. Phys. Lett.* 75, 19 (1999)
- [79] J. Heitmann, M. Schmidt, M. Zacharias, V. Y. Timosshenko, M. G. Lisachenko and P. K. Kashkarov, *Mater. Scien. and Eng. B* 105, 214-220 (2003)
- [80] A. Polman, *J. Appl. Phys.* 82, 1 (1997)
- [81] D. Pacifici, A. Irrera, G. Franzo, M. Miritello, F. Iacona and F. Priolo, *Physica E* 16, 331-340 (2003)
- [82] G. Franzo, V. Vinciguerra, E. Priolo, *Appl. Phys. A* 84, 3 (1999)
- [83] D. Kovalev et al. *Phys. Rev. B* 61, 4485 (2000)
- [84] A. J. Kenyon, S. S. Bhamber and C. W. Pitt, *Mat. Scien. and Eng. B* 105, 230-235 (2003)
- [85] M. Fujii, K. Toshikiyo, Y. Yamaguchi and S. Hayashi, *J. Appl. Phys.* 95, 1 (2003)
- [86] M. L. Brongersma, A. Polman, K. S. Min, E. Boer, T. Tambo and H. A. Atwater, *Appl. Phys. Lett.* 72, 20 (1998)
- [87] S. Takeoka, K. Toshikiyo, M. Fujii, S. Hayashi and K. Yamamoto, *J. Lumin.* 87-89, 350-352 (2000)
- [88] J. D. Blauwe, *IEEE Transc. on Nanotech.*,1, 1 (2002)
- [89] O. Gonzales-Varona, B. Garrido, S. Cheylan, A. P. Rodriquea and A. Cuadras, *Appl. Phys. Lett.* 82, 13 (2003)

- [90] P. Normand, E. Kapetanakis, P. Dimitrakis, d. Skarletos, D. Tsoukalas, K. Beltsios, et al., *Microelectronic Engineering* 67-68, 629-634 (2003)
- [91] Y. Shi, K. Saito, H. Ishikuro and T. Hiramoto, *J. Appl. Phys.* 84, 4 (1998)
- [92] S. Twari, O. Bissi, D. F. Falls, *Appl. Phys. Lett.* 68, 100 (1996)
- [93] J. W. Mayer, J. A. Davies and L. Erikson, *Ion Implantation in Semiconductors*, Academic Press, 1970
- [94] M. S. Sze, *Semiconductor Devices; Physics and Technology*, John Wiley and Sons, 1985
- [95] E. Borsella, M. A. Garcia, C. J. Fernandez, G. Mattei, C. Maurizio et al., *Nucl. Instr. Meth. Phys. Res. B* 191, 447-451 (2002)
- [96] J. D. Budai, C. W. White, *Nature* 390, 384 (1997)
- [97] Y. Kanematsu, H. Tanaka, Y. Fukunishi, T. Kushida, K. Sungmin, H. Atwater, *Phys. Rev. B* 62, 5100 (2000)
- [98] W. Wu, Y. Shi, H. Yamoto, *J. Vac. Sci. Technol. A* 17, 159 (1999)
- [99] T. V. Torchynska, J. A. Hernandez, A. I. Diaz Cano, Y. Goldstein, A. Many B. M. Bulakh et al., *Phys. Stat. Sol. A* 197, 2, 382-387 (2003)
- [100] N. Daldosso, M. Luppi, S. Ossicini, E. Degoli, R. Magri, G. Dalba R. Grisenti et al., *Phys. Rev. B* 68, 085327 (2003)
- [101] B. G. Fernandez, M. Lopez, C. Garcia, A. Perez Rodriguez, C. Banafos et al., *J. Appl. Phys.* 91, 2 (2002)

[102] S. Munekuni, T. Yamanaka, Y. Shimogiachi, R. Tohmon Y. Ohki et al., J. Appl. Phys. 68, 1212 (1990)

[103] U. Serincan, G. Aygun, R. Turan, J. Lumin. 113, 229 (2005)

[104] T. Matsuda, K. Nishihara, M.Kawabe, H. Iwata, S. Iwatsudo, T. Ohzone, Sol. Stat. Elect. 48, 1933-1941 (2004)

[105] A.N. Trukhin, J. Jansons, H. J. Fitting, T. Barfels, B. Schmidt, J. Non-Cryst. Sol. 331, 91-99 (2003)

[106] T. Gebel, L. Rebohle, J. Sum, W. Skorupa, A. N. Nazarov, I. Osiyuk, Physica E 16, 499-504 (2003)

ABBREVIATIONS AND ACRONYMS

TEM	Transmission Electron Microscope
XRD	X – Ray Diffraction
FTIR	Fourier Transform Infrared
PA	Phonon – Assisted
NC	Nanocrystals
PL	Photo Luminescence
EL	Electro Luminescence
ULSI	Ultra Large Scale Integration
LED	Light Emitting Diode
FN	Fowler - Nordheim Tunneling
DT	Direct Tunneling
NVM	Nonvolatile Memory Devices
ITO	Indium Tin Oxide
SRIM	The Stopping and Range of Ions in Matter
DOS	Density of States
NP	No – Phonon
PDOS	Phonon Density of States
QD	Quantum Dots
QDIP	Quantum Dot Infrared Photo Detector
EMA	Effective Mass Approximation
QW	Quantum Well
SIMOX	Separation by Implantation of Oxide
CVD	Chemical Vapor Deposition
SET	Single Electron Transistor
MOS	Metal Oxide Semiconductor
MOSFET	Metal Oxide Semiconductor Field Effect Transistor
EPR	Electron Paramagnetic Resonance
NBOHC	Non-bridging Oxygen Hole Center